On-Surface Chemical Reactions on an Insulating Substrate

Dissertation
zur Erlangung des Grades
“Doktor der Naturwissenschaften”
im Promotionsfach Physikalische Chemie

am Fachbereich Chemie, Pharmazie und Geowissenschaften
der Johannes Gutenberg-Universität Mainz

Markus Jan Kittelmann

geboren in Münster

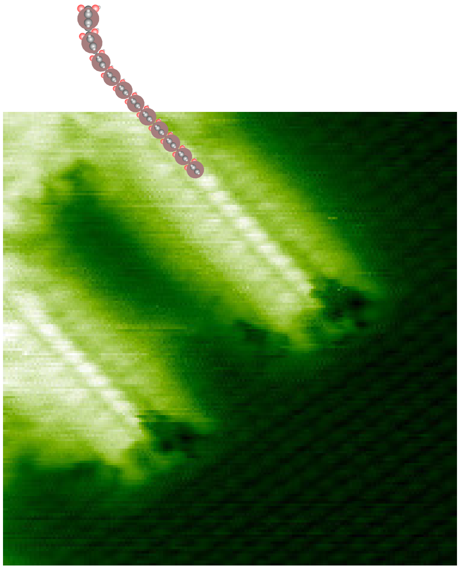

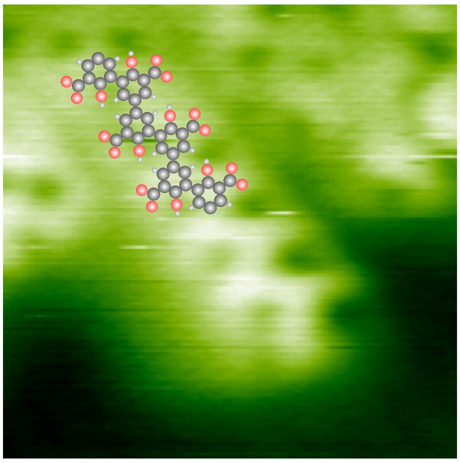

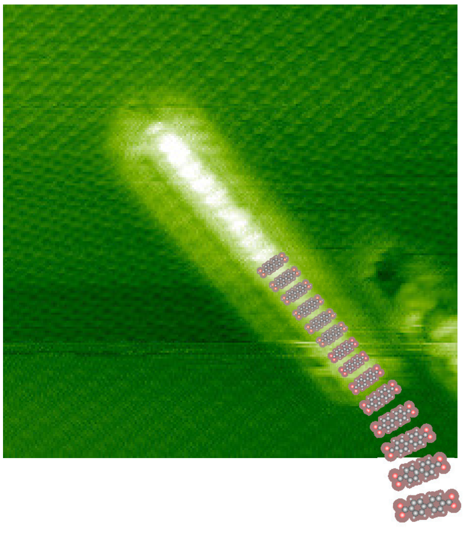

Mainz, den 30. Januar 2013

This dissertation was supervised by [Personal data removed] and was carried out at the Johannes Gutenberg-Universität Mainz from April 2010 to January 2013.

D77 (Dissertation Johannes Gutenberg-Universität Mainz)

dean of the faculty	[Personal data removed]
1st report	[Personal data removed] Johannes Gutenberg-Universität Mainz
2nd report	[Personal data removed] Johannes Gutenberg-Universität Mainz
3rd report	[Personal data removed] Universität Osnabrück

Submitted:	January 2013
Oral examination:	14. March 2013

Für meine Eltern

Contents

1 Introduction

In the middle of the last century, inorganic semiconductor research evolved from an emerging field into a powerful technology, having a tremendous impact on many areas of our daily life. The production of bipolar and field effect transistors enabled the development of today omnipresent microelectronics.

From this time onwards, the number of the transistors per area in electronic components doubles about every two years. These numbers follow Moore's law [1], who postulated this relationship already in 1965. Meanwhile, the manufacturers encounter severe problems in their striving for ever faster and more efficient microprocessors. The previously continuous downsizing of transistors based on silicon is intrinsically limited, and physical limits are expected to be reached no later than in 2020 [2].

The semiconductor industry is, therefore, forced to increase the size of computer chips for more transistors and to operate with a higher clock frequency. Both leads, however, to a rising energy consumption and higher waste heat. For this reason, scientists worldwide are intensively searching for new materials and processing strategies that can soon serve as a replacement for conventional silicon-based structures. These materials will represent the foundation for future electronics.

The currently most promising alternative to silicon is carbon. Carbon materials can provide substantial charge transport properties in systems with conjugated double bonds. Moreover, carbon is readily available in sufficient quantities. Therefore, molecular electronics is regarded as an extremely aspiring strategy to overcome the limits of silicon technology. The beginning of molecular electronics research dates back to the description of a single-molecule rectifier in 1974 [3]. The strategy of molecular electronics aims at using molecules instead of conventional semiconductor materials. The use of organic molecules leads to a minimum feature size in the nanometer range. Thus, molecular electronics bear the potential to produce smaller, cheaper and more efficient computer components in the future.

Nowadays, single functional units can be successfully built from organic molecules, for example switches [4], transistors [5] or diodes [6]. However, the molecules need to be connected to other units for arriving at an integrated functional device. This interconnection, however, still posing significant challenge in molecular electronics.

Extended wire structures are necessary for the networking of the molecular components. These large structures are, however, in general extremely insoluble and, therefore, not accessible by usual synthesis methods. A strategy to overcome this obstacle is the bottom-up construction of the required structures on the supporting surface. In contrast to the classical top-down principle, the bottom-up approach enables to build tailor-made molecular structures starting from predefined monomers. These monomer molecules can be easily deposited onto a surface and form the desired structure *in situ*.

Molecular self-assembly represents a powerful strategy to produce the desired nanostructures in a parallel fashion. A significant feature of molecular self-assembly is to benefit from weak and, therefore, mostly reversible interactions, such as van-der-Waals forces, π-π interactions and hydrogen bonding [7]. The reversibility of these bonds is inherent to self-assembled structures and offers the possibility to reach an ordered structure in thermodynamic equilibrium.

Electronic components, however, need to provide thermal and chemical stability, which is difficult to achieve with reversible interactions solely. Moreover, to arrive at structures with sufficient charge transport properties, conjugated structures are mandatory. Thus, the self-assembled structures have to be processed in a second step by covalent linking of the monomer molecules, in order to be able to guarantee sufficient stability and high conductivity for future applications. So far, this on-surfaces synthesis of organic molecules has been investigated only recently on metal surfaces [8]. However, the restriction to metallic surfaces constitutess a significant limitation for the future application in molecular electronics, since electronic devices, e.g. wires, require electrical decoupling from the supporting substrate.

To address this issue, this thesis explores on-surface synthesis on an electrically insulating substrate, namely calcite. After the introductory chapters, the self-assembly of structurally related organic molecules is investigated in terms of their interaction with the calcite substrate and their possibility to produce covalently bonded, extended structures.

In Chap. 6 the subtle balance between molecule-surface and intermolecular interactions is reflected in the coexistence between two different molecular structures, allowing for gaining insights into the driving forces behind the molecular self-assembly. In Chap. 7, results are presented that demonstrate the first direct visualization of the deprotonation step of a carboxyl group on an insulating substrate. The resulting phase is anchored by electrostatic interaction of the deprotonated carboxylate moieties with the surface calcium cations. The controlled activation of this substrate templating effect is demonstrated in Chap. 8 by inducing molecule deprotonation upon annealing the substrate.

Finally, the successful linking of halide substituted organic molecules will be demonstrated on the nonconductive calcite surface. In Chap. 9, the use of different halide substituted benzoic acid molecules is shown for the coupling reaction upon thermal activation. The comparatively high binding strength of the deprotonated carboxylic group towards calcite is exploited to avoid desorption upon annealing the surface. The rational approach of this concept is confirmed by systematically varying both the position and the number of halide substitution, resulting in conjugated molecular wires, zig-zag structures as well as dimers.

By varying the halides within a molecule, as discussed in Chap. 10, opportunity promising possibility for the covalent linking of molecules in a hierarchical manner is shown by the selective activation of defined sites. The results of this thesis, thus, constitute a significant step towards exploiting on-surface synthesis for molecular electronics and related applications.

2 Measurement Methods

Contents

The invention of scanning probe microscopy represents a pivotal development in the field of surface science. Many of the current advances in the area of nanotechnology would not have been possible without the information gained from scanning probe microscopy.

This chapter will describe the basic principles of the atomic force microscopy (AFM) technique and a related method, namely the Kelvin probe force microscopy (KPFM). Within this thesis, I have used both techniques in the frequency modulated (FM) mode, refered to as the FM-AFM and FM-KPFM.

2.1 Atomic Force Microscopy

Historical Background

A great milestone in surface science was the invention of the scanning tunneling microscope (STM) in 1981 [9]. For the development of the STM Binnig and Rohrer were awarded the Nobel Prize in physics in 1986 [10]. Nowadays, the technique is established as a most powerful tool in the field of surface science, which can achieve topographic images with highest spatial resolution [11]. This analysis technique is based on a tunneling current measured between the scanning tip and the investigated sample. However, this limits the technique to conductive substrates.

Thus, Binnig et al. have invented the atomic force microscope (AFM) in 1986 [12]. The AFM measures forces between the tip and the surface atoms instead of the tunneling current in STM to obtain an image of the surface. In the AFM, the tip is attached to the end of a cantilever. If the tip is close to the surface, this cantilever is deflected due to the forces between tip and surface (see Fig. 2.1).

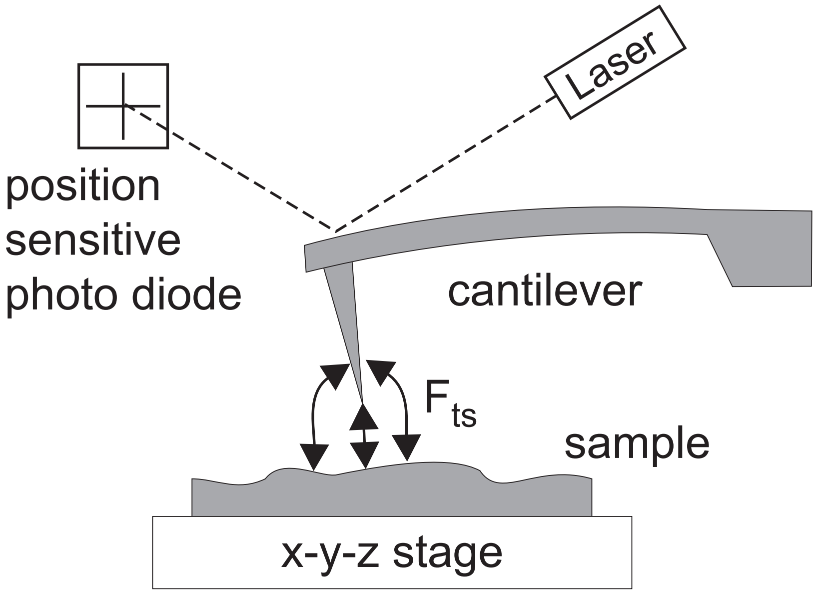

Figure 2.1: Basic principle of AFM: The interaction forces between the tip and the sample surface cause a deflection of the cantilever. In the most-common beam-deflection setup, this deflection is read out by reflecting a laser beam on a photo diode. (Adapted from [13])

For imaging the sample, the cantilever is scanned over the surface in a line by line mode. In parallel to this scanning movement, the deflection of the cantilever is detected by a laser beam, which is reflected from the backside of the cantilever onto a position-sensitive photo diode [14]. The changes in the force between tip and surface can, thus, be capture by the deflection signal and result in an image of the surface. Already very early AFM was used in a variety of studies, covering topics ranging from biological studies of cells [15] to DNA on surfaces [16]. However, the goal of atomic resolution was achieved first in 1996 by AFM operated in non-contact (NC) mode. After atomic resolution had once been shown on $\mathrm{Si}(111)-7\times 7$ [17; 18], a large number of studies followed, presenting atomically resolved images on a large variety of surfaces [19].

Forces in AFM

As already mentioned, the interaction between an AFM tip and a surface is determined by the interplay of various forces. The most important forces will be discussed here briefly.

Short-Range Forces

Short-range chemical forces are caused by the overlap of the electron wave functions of the atoms of the tip and the surface and by the repulsion of the atomic nuclei. Chemical forces can be both, repulsive and attractive. For example, they may result in the formation of bonding orbitals of tip and sample, but they also can form nonbonding orbitals [20].

Usually, repulsive chemical forces are described by an empirical potential,

$$U_{\mathrm{rep}} = \left(\frac{\sigma}{d}\right)^n \; ; n = 9, \ldots, 16 \tag{2.1}$$

where d is the distance between the atomic centers and σ an empirical parameter.

Figure 2.2: Model of a cantilever tip above the sample surface.

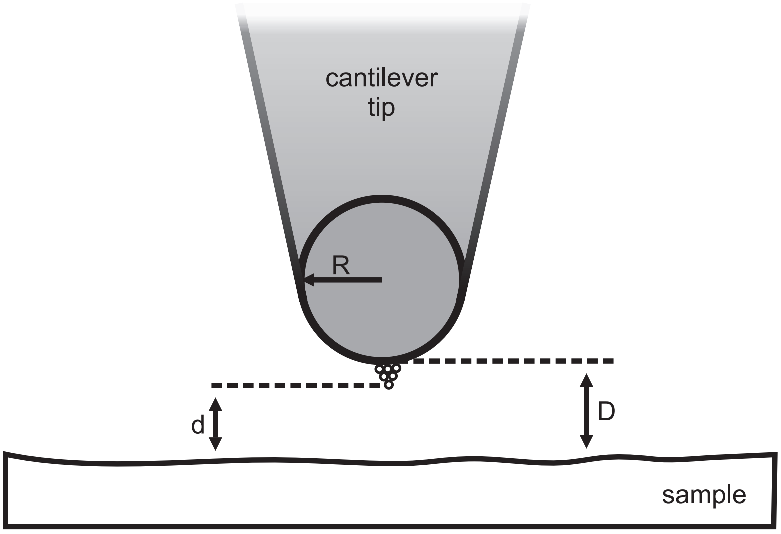

The chemical forces are characterized by their short-range nature with decay lengths below 1 nm (indicated in Fig. 2.2 by d). As shown by theoretical calculations short-range chemical forces are decisive for obtaining images with atomic resolution [21]. To model these short-range forces, typically model potentials such as the Morse potential or the Lennard-Jones potential are employed.

Van-der-Waals Forces

Van-der-Waals (vdW) forces are based on electrostatic dipole-dipole interactions. The forces describe the interaction of both, permanent and induced dipoles. The vdW forces are always present and thus, have to be considered in any AFM experiment. Van der Waals forces are, with few exceptions, always attractive. The range is large, 1 nm - 100 nm, thus not only the atomic tip apex, but the mesoscopic tip has to be considered. The interaction potential U between two neutral atoms is a function of their distance and their mutual polarizability [22].

The potential $U(r)$ for vdW interactions is given by:

$$U(r) = -\frac{C}{r^6} \tag{2.2}$$

where r is the radius and C a constant term to represent the two atoms depending on their properties.

As the vdW forces act over a wide range, there are uncountable dipole-dipole interactions between the atoms of the tip and the surface. Therefore, these forces are difficult to consider in an atomistic model. Hamaker offered a simplification by describing the tip and the surface as a continuous material characterized by macroscopic material properties [23].

The force F_{vdW} between two macroscopic objects is defined by the Hamaker summation method as:

$$F_{\mathrm{vdW}} = \rho_{\mathrm{t}}\rho_{\mathrm{s}} \int_{V_{\mathrm{s}}}\int_{V_{\mathrm{t}}} -\nabla\left(-\frac{C}{r^6}\right) dV_{\mathrm{t}} dV_{\mathrm{s}} \tag{2.3}$$

Here, $\rho_{\mathrm{t/s}}$ are the materials' densities and $V_{\mathrm{t/s}}$ are the volumes of the tip and surface. By using the material-dependent Hamaker constant [24] $H = \pi^2 C \rho_{\mathrm{t}}\rho_{\mathrm{s}}$, Eqn. 2.3 reads:

$$F_{\mathrm{vdW}} = H \int_{V_{\mathrm{s}}}\int_{V_{\mathrm{t}}} -\nabla\left(-\frac{1}{r^6}\right) \frac{1}{\pi^2} dV_{\mathrm{t}} dV_{\mathrm{s}} \tag{2.4}$$

For a spherical tip of radius R, which is located at a distance D from a flat surface (see Fig. 2.2) the following vdW force is calculated:

$$F_{\mathrm{vdW}} = -\frac{HR}{6D^2} \tag{2.5}$$

The values for H are in the order of $10^{-19}J$. The vdW forces extend over a large surface area and, therefore, they do not contribute to the atomic structure in the AFM image. Thus, for high-resolution imaging, vdW forces are undesirable. To minimize these forces, it is necessary to use very sharp tips, as is apparent from Eqn. 2.5.

Electrostatic forces

Electrostatic forces are present between conductive tips and conductive samples if these are at different electrostatic potentials. A contact potential difference occurs naturally if the tip and the sample have different work functions. Electrostatic forces are also present between localized charges situated in electrically insulated tips or samples. Most likely, these types of localized charges emerge easily due to the surface preparation such as cleaving a bulk insulating crystal. Usually, these charges are stationary and do not leak off from a non-conductive sample [25]. This situation can also described approximately by a contact potential difference.

The system of tip and sample forms a capacitor with capacitance C. The electrostatic force F_{el} with an externally applied voltage U_{dc} and a contact potential difference U_{cpd} is given by:

$$F_{\mathrm{el}} = -\frac{1}{2}\frac{\partial C}{\partial z}\left(U_{\mathrm{dc}} - U_{\mathrm{cpd}}\right)^2 \tag{2.6}$$

Thus, this force can be compensated by applying an appropriate voltage U_{dc}. In the experiments performed in this thesis, this is usually done by a constant value for U_{dc}, determined once at the beginning of the measurement.

By using an additional feedback loop, this voltage compensation can be performed for every sample position. By recording the required voltage to compensate the electrostatic force during scanning, one obtains information on local changes of charges on the sample surface. This special version of NC-AFM is referred to as Kelvin probe force microscopy (KPFM) [26]. This technique will be described in Sec. 2.2.

Lennard-Jones potential

A very common analytical description of the interaction between two atoms is the Lennard-Jones potential with empirical parameters (σ and ϵ):

$$U_{\mathrm{LJ}}(d) = 4\epsilon\left(\left(\frac{\sigma}{d}\right)^{12} - \left(\frac{\sigma}{d}\right)^{6}\right) \tag{2.7}$$

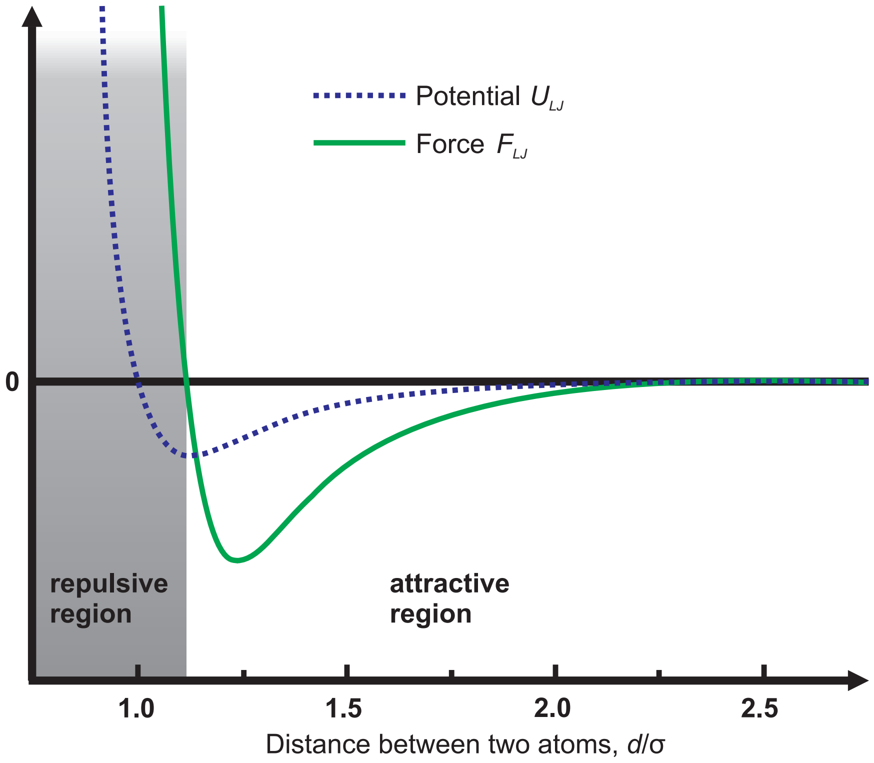

Figure 2.3: Lennard-Jones potential for describing a pairwise atom-atom interaction: This potential is composed of a repulsive term, which results from the Pauli exclusion principle, and an attractive term that models the atomic vdW forces.

The attractive vdW interaction is considered in the d^{-6} term wile the d^{-12} term is an empirical description of the repulsive chemical interaction. The Lennard-Jones potential represents a very useful model for the interaction between the atoms as a function of distance (Fig. 2.3).

Working principle

In AFM, different methods to measure forces are used, resulting in various modes of operation. A very fundamental differentiation is made between static and dynamic AFM.

In the static mode, also named contact AFM mode, the cantilever, having a stiffness k, is usually scanned at a constant distance to the sample surface. The distance is controlled by a feedback loop whose control signal is the deflection of the cantilever that is related to the tip-sample interaction force F_{ts}. Soft cantilever ($k \approx 0.01\,\mathrm{N/m}$ - $5\,\mathrm{N/m}$) should be used for this mode to achieve a large deflection signal on the photo diode [27].

Typically, the measurement is preformed in the repulsive interaction region (see Fig. 2.3). In this AFM mode, the tip is generally pressed onto the sample surface, resulting in a blint tip. Obviously, the lateral resolution is limited by the tip radius. The large interaction area between tip and sample makes true atomic resolution impossible (atomic defects cannot be resolved). When aiming at atomically resolved images, non-contact AFM (NC-AFM), a dynamic AFM mode, is the method of choice.

In NC-AFM, the cantilever is excited externally, e.g., via a piezo, to oscillate. In this case, the distance feedback loop can be regulated on different parameters. A differentiation is made between amplitude modulation AFM (AM-AFM) [28] and frequency modulation AFM (FM-AFM) [29].

Amplitude modulation AFM

In the AM-AFM method, developed 1987 by Martin, Williams and Wickramasinghe, the cantilever, having a quality factor Q, is excited to oscillate at a fixed frequency [28].

When the tip approaches the sample surface, the resonance frequency of the cantilever shifts due to the interaction with the surface. Hence, the free oscillation amplitude A changes by a value ΔA to a smaller amplitude A_{set} (Fig. 2.4). This change

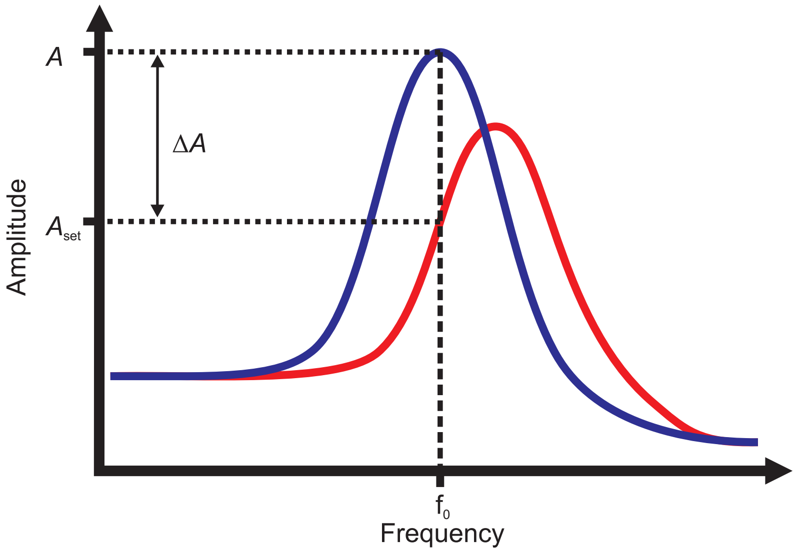

Figure 2.4: Oscillation amplitudes for the free oscillating measurement tip (blue) and in interaction range (red): Repulsive forces lead to a frequency shift towards higher frequencies. The cantilever is still excited at f_0 in AM-AFM, thus, the oscillation amplitude is reduced by ΔA.

in the amplitude of oscillation is used as the control variable for the distance feedback loop.

A severe disadvantage of this method is the long response time. The oscillation amplitude changes only after a settling time of $\tau_{\mathrm{AM}} \approx Q/(\pi f_0)$ [29]. Very high Q-values arise especially under vacuum conditions [30] and result in very long measurement times. Therefore, AM-AFM is usually not used under UHV conditions.

Frequency modulation AFM

The FM-AFM mode was developed in 1991 by Albrecht, Grütter, Horne and Rugar [29]. In FM-AFM, the cantilever is again excited to oscillate. Due to the interaction between tip and sample, which can be expressed by the force gradient k_{ts}, the resonance frequency f_0 of the free oscillating cantilever will change to the current resonance frequency f by $\Delta f = f - f_0$.

For harmonic oscillator, f_0 is defind by the following equation:

$$f_0 = \frac{1}{2\pi}\sqrt{\frac{k}{m^*}} \tag{2.8}$$

with k being the stiffness and m^* being the effective mass of the cantilever.

If the tip is brought close to the surface, the forces discussed in Sec. 2.1, caused by the interaction between the tip and sample, affect the oscillating tip. For small oscillation amplitudes and a large distance between tip and surface, the k_{ts} can be assumed to be constant during the period of oscillation. Therefore, Eqn. 2.8 can simply be complemented by $k_{\text{ts}} = \partial F_{\text{ts}}/\partial z$ [27]:

$$f = \frac{1}{2\pi}\sqrt{\frac{k + \frac{\partial F_{\text{ts}}}{\partial z}}{m^*}} \tag{2.9}$$

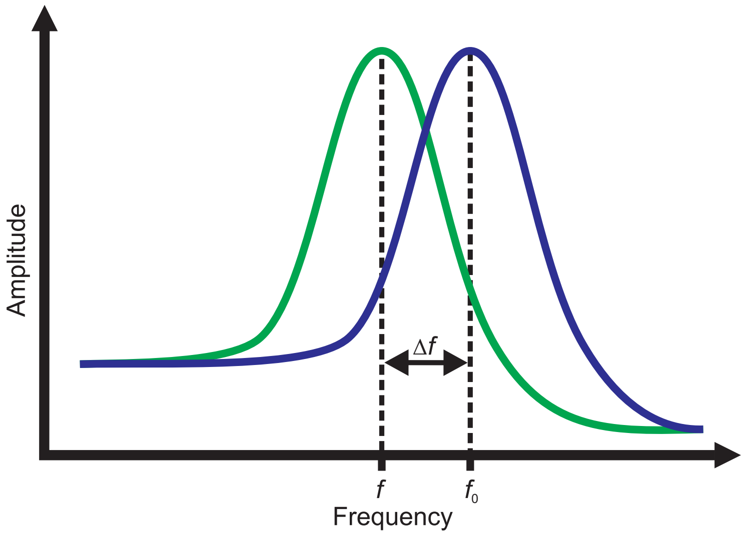

Figure 2.5: Operation in FM-AFM: The resonance curve of the free oscillation at f_0 (blue) is shifted by attractive forces between tip and sample toward lower resonance frequencies f (green).

In general, k_{ts} of repulsive forces has a positive sign, which leads to an increase of resonance frequency. Attractive forces, in contrast, usually manifest themselves by a reduced resonance frequency (Fig. 2.5).

A mathematical relationship between the frequency shift and k_{ts} is obtained by inserting Eqn. 2.8 and 2.9 into $\Delta f = f - f_0$. If $k_{\mathrm{ts}} << k$, the resulting expression can be simplified using a Taylor series and the frequency shift Δf can be expressed as [27]:

$$\Delta f = \frac{f_0}{2k}\frac{\partial F_{\mathrm{ts}}}{\partial z} = \frac{f_0}{2k}k_{\mathrm{ts}} \tag{2.10}$$

This equation is incorrect for the case of large oscillation amplitudes and short distances of tip and surface, because the force gradient can no longer be considered as constant during one period of oscillation.

Consequently, for calculating Δf, the tip-sample force F_{ts} have to integrate over a whole cycle ($q' = A\cos(2\pi f_0 t)$) [27]:

$$\Delta f(z) = -\frac{f_0}{\pi k A^2}\int_{-A}^{A} F_{\mathrm{ts}}\frac{(z-q')q'}{\sqrt{A^2-q'^2}}\,dq' \tag{2.11}$$

Via partial integration follows that the force gradient is convolved with a weighting function over a period of oscillation [27]:

$$\begin{aligned}\Delta f(z) &= \frac{f_0}{2k}\frac{2}{\pi A^2}\int_{-A}^{A} k_{\mathrm{ts}}\sqrt{A^2-q'^2}\,dq' && (2.12)\\ &= \frac{f_0}{2k}\langle k_{\mathrm{ts}}\rangle && (2.13)\end{aligned}$$

In contrast to AM-AFM, the settling time $\tau_{\mathrm{FM}} \approx 1/f_0$ is independent of the quality factor Q in the FM-AFM [21]. Thus, it is possible to measure with high Q-cantilevers which improves the signal-to-noise ratio of the measurement [32].

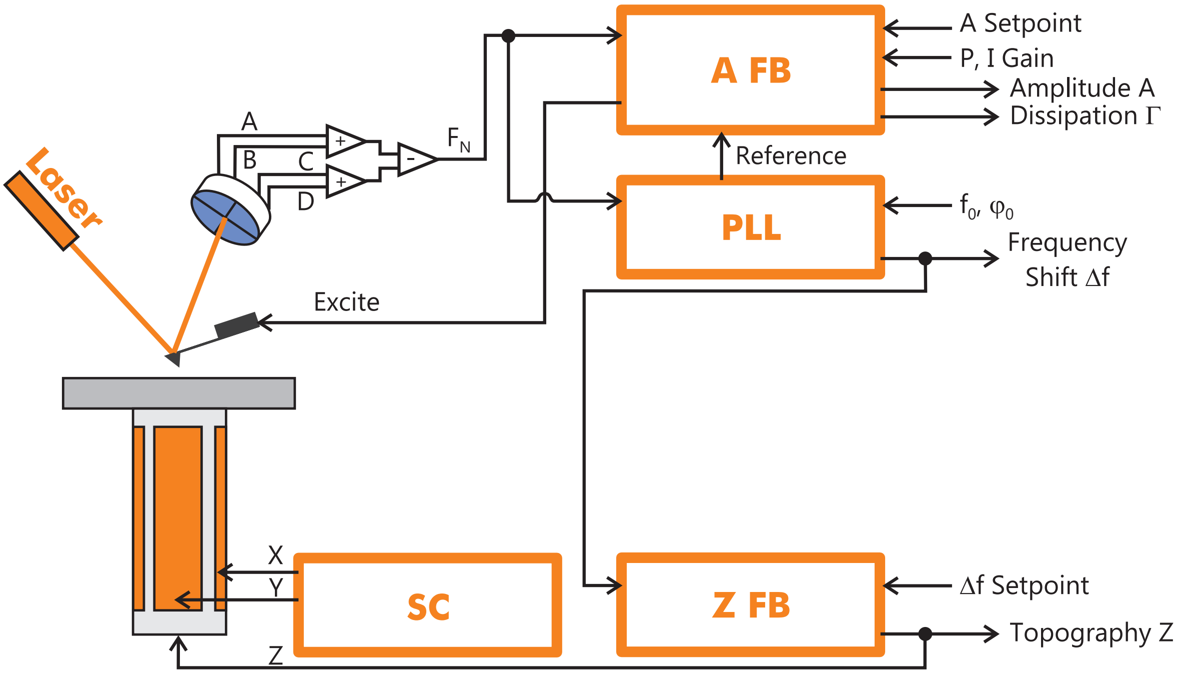

Figure 2.6: Block diagram of the electronic: The cantilever is excited by a sinusoidal signal via a piezo. The frequency of the oscillating signal from the cantilever is detected in the PLL and the difference Δf is passed to the control electronics. (Adapted from [31])

The frequency shift is used as the control variable for the distance feedback loop. The signal path of the frequency shift including the necessary electronic components is schematically shown in Fig. 2.6. The oscillation of the cantilever is detected by using a four-quadrant photodiode. In analogy to contact mode AFM, this sinusoidal signal is referred to as F_N.

Thi F_N signal is passed in both, the Phase-Locked Loop (PLL) and the amplitude feedback (A FB). The PLL determines the current resonant frequency f of the cantilever oscillation. As an output, the frequency shift Δf, which is the deviation of the frequency f from the resonance frequency f_0 of the undisturbed cantilever oscillation, is given. The Δf-signal is forwarded to the distance control circuit and the electronics for recording the Δf image.

In the amplitude feedback, the F_N signal is converted into a DC signal by calculating the root mean square. Thereafter, this signal is compared with the preset setpoint of the amplitude (A_{setpoint}) to kept the amplitude constant by a further feedback loop. The outputs amplitude (A) and dissipation (Γ) are monitored and recorded as separate "images". Moreover, the controlled amplitude signal is multiplied with the reference signal from the PLL. By this way, an excite signal is generated that is directly applied to the excitation piezo.

2.2 Kelvin Probe Force Microscopy

Basics

The AFM technique enables mapping of the sample surface, but does not provide chemical sensitivity. Kelvin probe force microscopy (KPFM) was introduced to imaging the surface potential of a surface with high vertical resolution. FM-KPFM is an extension to the NC-AFM mode and measures the contact potential difference (CPD) between tip and the sample.

Historically, “Kelvin probe” is derived from Lord Kelvin’s method of measuring the difference in work function between two materials in 1898 [33]. Two metals with different work functions $\Phi_{1,2}$, align their Fermi energy levels by charge displacement upon electrical contact. However, when a suitable compensation potential is applied between the metals, no equalizing of the Fermi levels is observable.

Lord Kelvin’s concept was further developed by Zisman [34] and was first introduced for AFM by Nonnenmacher in 1991 [35], establishing the method now referred to as KPFM. The KPFM technique has been used extensively for directly mapping electronic properties of organic devices [36; 37], biological materials [38], the charge state of adsorbates [39] as well as the charge distribution within a single molecule [40]. Recently, KPFM has also been applied for investigating organic molecules on bulk insulator surfaces [41].

In the KPFM mode, sample and tip can be described as the two capacitor electrodes. When establishing an electrical contact between the tip and the surface, the usually different work functions (Fig. 2.7(a)) lead to a charge transfer (Fig. 2.7(b)) and a corresponding potential difference

$$U_{\mathrm{cpd}} = \frac{\Phi_{\mathrm{sample}} - \Phi_{\mathrm{tip}}}{e} . \tag{2.14}$$

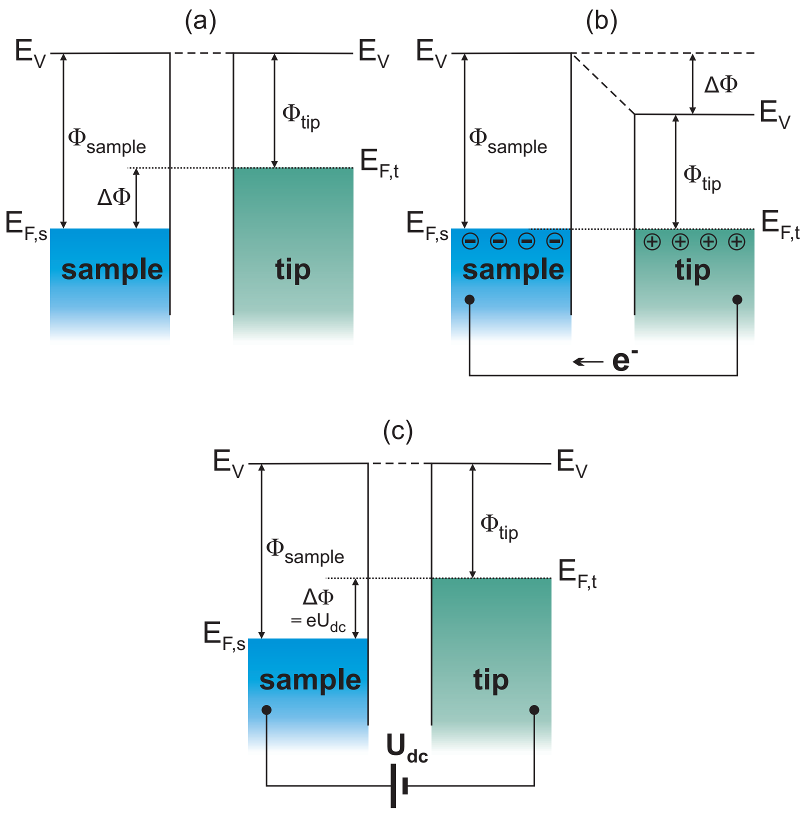

Figure 2.7: Energy level shift of two metals, here a sample and a tip, with different work functions Φ_{sample} and Φ_{tip}: (a) without contact, (b) with electrical back-contact, (c) with an externally applied voltage (U_{dc}).

The electrostatic force (see Eqn. 2.6) can be calculated from the capacity gradient $\partial C/\partial z$. Thus, the force gradient $\partial F/\partial z$ leads to a charge in the cantilever's resonance frequency. By applying a suitable compensating voltage, indicated by U_{dc} in Fig. 2.7(c), the Fermi-levels are raised into their initial position, the electric field disappears and, thus, the electrostatic force.

There are alternative approaches to determine the work function of a surface. A common method is photoelectron spectroscopy (PES) [42]. This quantitative experimental method determines the kinetic energy of emitted photo electrons, which have been excited either by ultraviolet light (ultraviolet photoelectron spectroscopy (UPS)) or X-ray (X-ray photoelectron spectroscopy (XPS)) photons. However, the disadvantage of these techniques is that they provide no spatial resolution. Instead, the sample work function is averaged over several square millimeters.

Of course, STM could be used for spatial resolution [43]. However, the wave functions of tip and sample have to overlap in STM to allow for a tunnelling current flowing. Therefore, the investigated system cannot be designated as undisturbed as it is influenced by the presence of the tip [44]. Furthermore, insulators cannot be investigated because of the absence of electric conductivity.

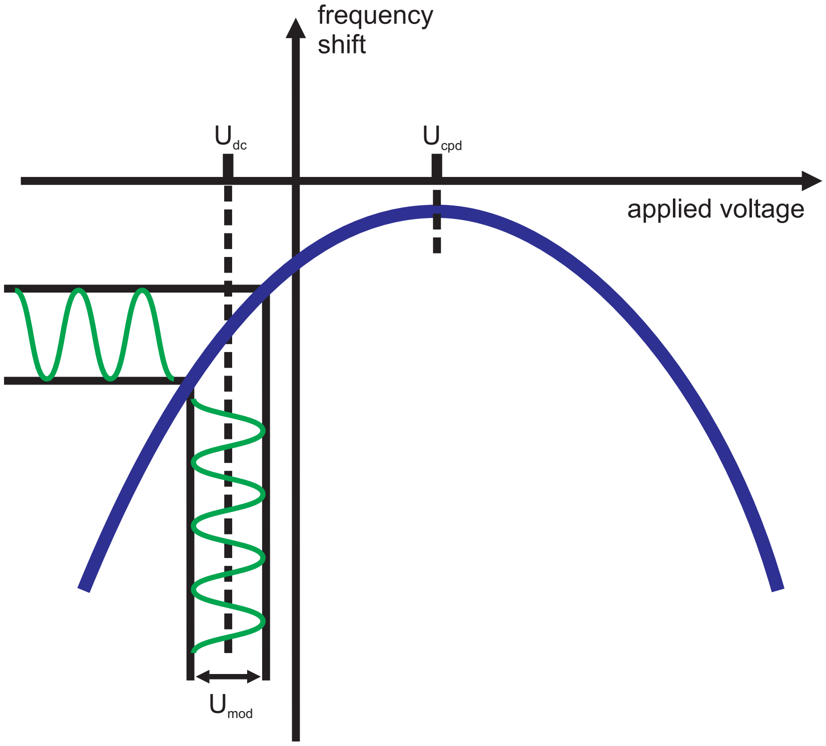

Figure 2.8: When the applied voltage between the tip and the sample is sweeped and the frequency shift of the cantilever is captured simultaneously, the result is a parabola. The position of the vertex marks U_{cpd}. For KPFM, the modulation voltage U_{mod} is transferred, in dependence of the value of U_{dc}, with a various amplitude and phase to the Y-axis. By using a lock-in amplifier and a feedback loop, the amplitude is minimized on the Y-axis, so that U_{dc} is continuously adjusted to U_{cpd}.

As alternative to the aforementioned methods, KPFM [35; 45] is applicable to insulating surfaces and offers both, a high lateral resolution and quantitative results. No additional measurement have to be made since the KPFM image can be recorded simultaneously with the topographic image [46]. The operation of the AFM in non-contact mode assures a very weak interaction between the tip and the surface. It is, therefore, possible to assume that the electronic properties of the surface are measured unadulterated.

Components of the Electrostatic Force

For $U_{\mathrm{cpd}} = \Delta\Phi/e$, the electrostatic force (Eqn. 2.6) between tip and sample, having a difference in work functions of $\Delta\Phi = \Phi_{\mathrm{sample}} - \Phi_{\mathrm{tip}}$, can be written as [47]

$$F_{\mathrm{el}} = -\frac{1}{2}\frac{\partial C}{\partial z}\left(U_{\mathrm{dc}} - \frac{\Delta\Phi}{e}\right)^2 \tag{2.15}$$

.

By calculating the gradient and using Eqn. 2.10, the quadratic relationship between the applied voltage U_{dc} and the frequency shift Δf is given as:

$$\Delta f_{\mathrm{el}} \propto \frac{\partial F_{\mathrm{el}}}{\partial z} = -\frac{1}{2}\frac{\partial^2 C}{\partial^2 z}\left(U_{\mathrm{dc}} - \frac{\Delta\Phi}{e}\right)^2 \tag{2.16}$$

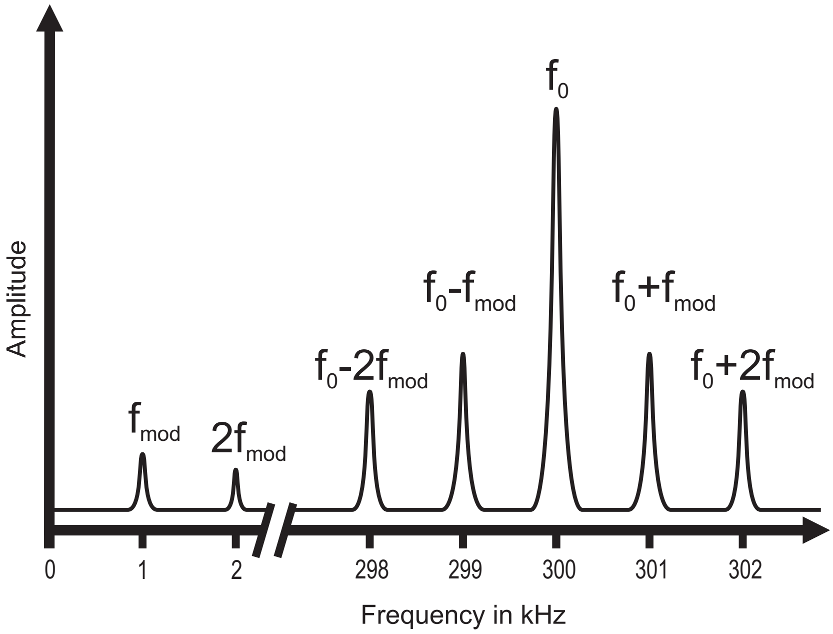

Figure 2.9: Expected frequency spectrum in FM-KPFM: The oscillation signal at f_0 is frequency modulated by f_{mod} and $2f_{\mathrm{mod}}$.

The position of the apex of the red parabola in Fig. 2.8 marks the point where the applied voltage compensates the contact potential difference. For this applied voltage U$_{\mathrm{dc}}$, the CPD is nullified and the electrostatic interaction is minimized. Consequently, U_{cpd} can be determined very accurately by fitting the resonance frequency voltage parabola with a quadratic function.

A continuous adjustment of $U_{\mathrm{dc}} = U_{\mathrm{cpd}}$ is achieved by modulating U_{dc} with a small voltage U_{mod} of frequency f_{mod}. For the total potential difference this results in [48]:

$$U = U_{\mathrm{dc}} - \frac{\Delta\Phi}{e} + U_{\mathrm{mod}} \cos(2\pi f_{\mathrm{mod}} t) \tag{2.17}$$

Combining Eqn. 2.15 and Eqn. 2.17 and expanding the squared sine results in three terms, one static term and two periodic terms at f_{mod} and $2f_{\mathrm{mod}}$:

$$\begin{aligned} F_{\mathrm{el}} = &-\frac{1}{2}\frac{\partial C}{\partial z}\left[\left(U_{\mathrm{dc}} - \frac{\Delta\Phi}{e}\right)^2 + \frac{1}{2}U_{\mathrm{mod}}^2\right] && (2.18)\\ &+ \frac{\partial C}{\partial z}\left(U_{\mathrm{dc}} - \frac{\Delta\Phi}{e}\right) U_{\mathrm{mod}} \cos(2\pi f_{\mathrm{mod}} t) && (2.19)\\ &+ \frac{1}{4}\frac{\partial C}{\partial z} U_{\mathrm{mod}}^2 \cos(2\pi 2 f_{\mathrm{mod}} t) && (2.20) \end{aligned}$$

The second term can be used for an efficient determination of $\Delta\Phi$. The modulation, caused by U_{mod}, can be detected with a lock-in amplifier from the signal of the frequency shift. The amplitude of this signal is zero when the applied voltage U_{dc} corresponds to the contact potential difference $\Delta\Phi/e$ as is directly apparent from Eqn. 2.19. The amplitude-signal from the lock-in amplifier is then used as the control variable for U_{dc} and, thus, the measurement of the U_{cpd} can be performed in parallel to the regular AFM measurements.

In the experimental implementation, there are two different detection possibilities similar to the NC-AFM mode; the amplitude modulation (AM-KPFM) and the frequency modulation (FM-KPFM) KPFM. In this work, FM-KPFM is used.

Frequency modulation KPFM

In the FM-KPFM mode, an applied AC voltage induces a modulation of the electrostatic force. As a result, the oscillation signal is frequency modulated. As shown in Eqn. 2.19 and Eqn. 2.20, this frequency modulation is at f_mod and $2f_\mathrm{mod}$ around f_0. Fig. 2.9 shows the expected frequency spectrum for the cantilever oscillation signal. The signals at f_mod and $2f_\mathrm{mod}$ are directly caused by the electrostatic force, which produces an oscillating deflection of the cantilever.

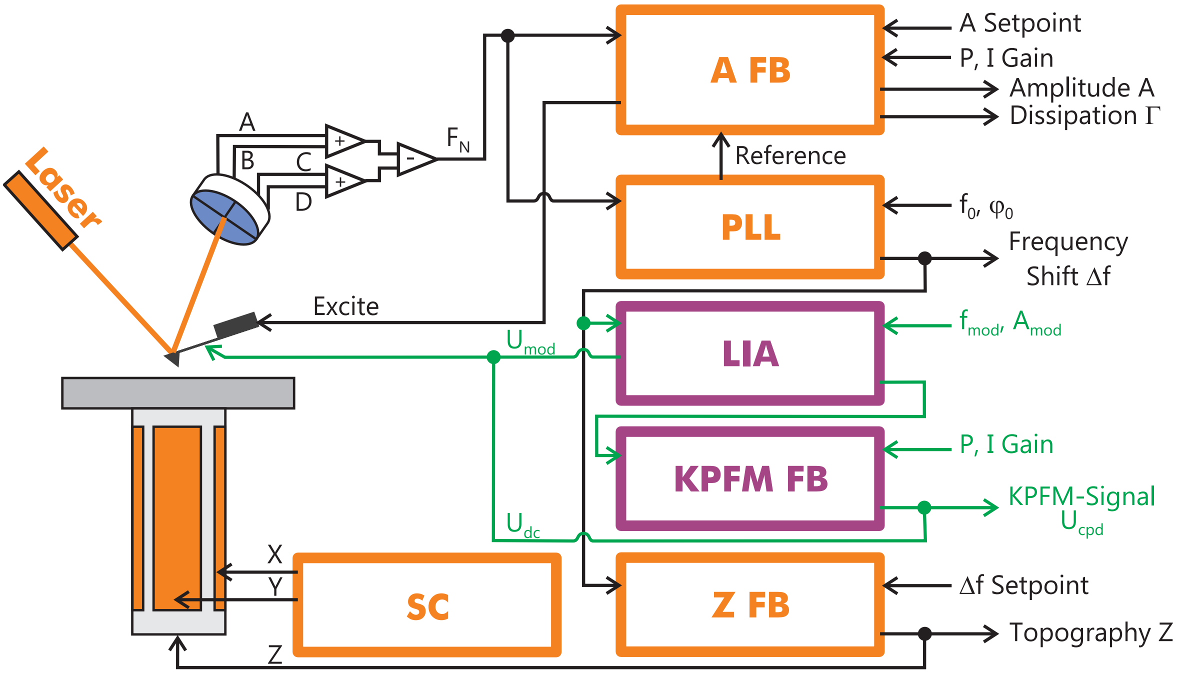

Figure 2.10: Block diagram of the electronics: The KPFM components and lines are colored in purple and green, respectively. For FM-KPFM, the demodulated Δf-signal at f_mod is used to supply the KPFM-feedback controller (KPFM FB). (Adapted from [31])

The amplitude of the sideband at f_mod is proportional to $(U_\mathrm{dc} - \Delta\Phi/e)$. Thus, to determe $U_\mathrm{dc} = \Delta\Phi/e$, the goal is to vary U_dc until these side bands disappear. This requires the demodulation of the oscillation signal, performed in the PLL.

Then a lock-in amplifier determines phase and amplitude of the modulation f_mod. Finally, a KPFM-feedback controller readjust U_dc, so that the modulation signal at f_mod disappears to fulfill $U_\mathrm{dc} = \Delta\Phi/e$. If this condition is met, f_0 is no longer frequency modulated by f_mod. In FM-KPFM cantilevers with a spring constant above 5 N/m can also be used. There are no limits for the bandwidth of the detector.

Fig. 2.10 shows the block diagram extended by the electronics used in FM-KPFM. The newly installed lock-in amplifier (LIA) generates the reference signal f_{mod}, which is added as a modulating voltage U_{mod} to the output voltage U_{dc} of the Kelvin controller.

The bandwidth of the PLL is larger than f_{mod}, so the electrostatic modulation of the cantilever is preserved in the Δf-signal. In the PLL, thus, a demodulation of the sidebands $f_0 \pm f_{\mathrm{mod}}$ is performed. For FM-KPFM, the Δf signal is passed to the input of the LIA. The Δf signal is demodulated by the LIA and the amplitude and the phase position to the internal reference f_{mod} are determined. The result is a DC voltage proportional to $(U_{\mathrm{dc}} - \Delta\Phi/e)$. This voltage is utilized by the Kelvin controller as the control signal to readjust U_{dc} to the value of $\Delta\Phi/e$.

3 Experimental Setup and Equipment

Contents

All experiments presented in this thesis are acquired in a ultra-high vacuum system. This chapter gives an insight into the experimental setup. In addition, preparation parameters and data processing are explained.

Ultra-High Vacuum System

In this thesis, a commercially available UHV system is used, including a scanning probe microscope, the VT AFM 25 from Omicron (Omicron NanoTechnology GmbH, Taunusstein, Germany).

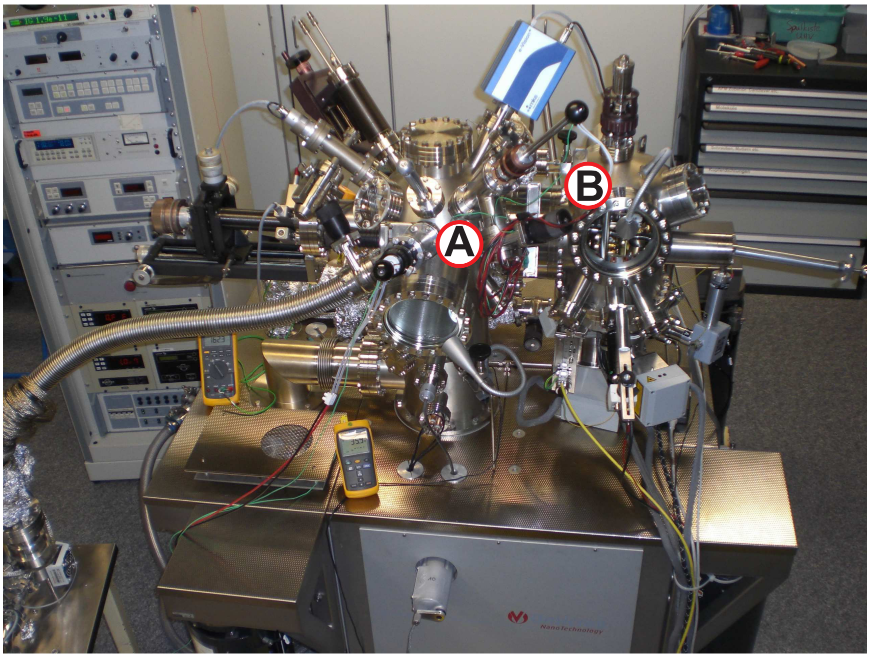

Figure 3.1: Ultra-high vacuum system and attached equipment at the preparation chamber (A) and microscope chamber (B).

The central UHV system is composed of two main chambers. The first chamber, labeled with A in Fig. 3.1, is the preparation chamber, which is used for the preparation of samples and tips. The heatable and coolable manipulator (Vacuum Generators Ltd., Hastings, United Kingdom) acts as the main part.

Moreover, several additional components are installed at the preparation chamber:

- an sputter ion gun from Omicron for cleaning the tips,
- two home-built molecule sublimators for deposition the organic molecules onto the surfaces,
- a home-built crystal cleaver for sample preparation,

- a quadrupole mass spectrometer e-Vision+ (MKS Instruments, Crewe, United Kingdom) for residual gas analysis and

- a quartz crystal microbalance from Inficon (Bad Ragaz, Switzerland) for adjusting the molecular deposition rates.

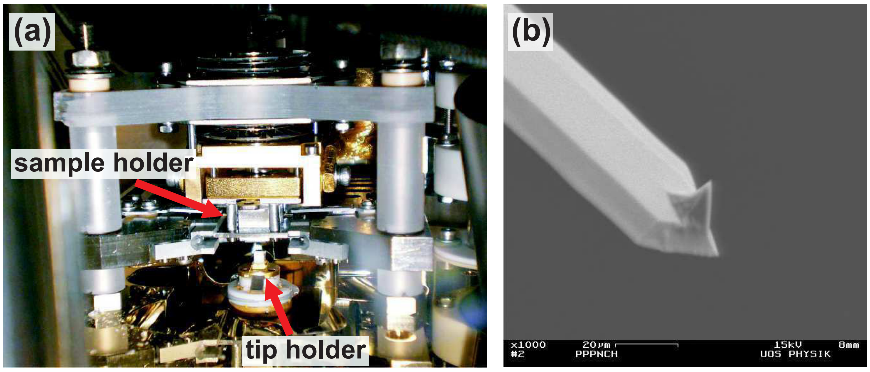

Figure 3.2: (a) View onto the scanning probe microscope: The sample holder is held in position by clamping springs and the probe tip is approached from the bottom to the sample surface. (b) Electron microscopy image of an NCH-PPP 300 kHz AFM tip prior to use. Courtesy of [Personal data removed], University of Osnabrück. (Adapted from [49; 50])

The scanning probe microscope (Fig. 3.2(a)) and a storage carousel for samples and tips are in the second main chamber (marked with B in Fig. 3.1), which can be completely separated from the preparation chamber via a valve.

The system performance has been optimized by several steps [51], e.g., indroduction of a PLL and a new preamplifier. For the optimized system, the background noise level was determined to $125\,\mathrm{fmHz}^{-0.5}$ [32].

Using this optimized setup, it is possible to image conducting and insulating surfaces at the atomic scale [52–54] at temperatures between 25K and 350K. All images shown in this thesis are collected at room temperature.

The tips and samples can be replaced via a load-lock chamber. The load-lock chamber is connected to the preparation chamber. The pressure in the preparation and the microscope chamber is usually lower than $1 \cdot 10^{-10}$ mbar to minimize contaminations at the sample surface.

Equipment and Accessories

The used molecule sublimator is based on a design from [Personal data removed] [55] and was adapted to the present chamber by [Personal data removed] [49]. The sublimator consists of a Knudsen cell [56], which is mounted on a linear translator.

The Knudsen cell is a glass tube, which is closed at one end, having an inner diameter of 2 mm and a length of about 15 – 20 mm. Fig. 3.3 shows a detail image of the Knudsen cell. The glass tube is heated by a tantalum wire of 0.5 mm in diameter. The device is equipped with a thermocouple as sensor for temperature measurements. The contacting for the heating wire and the thermocouple into UHV is done by a special feedthrough from Allectra GmbH (Berlin, Germany). The molecules are placed in the closed end of the glass tube and are secured by glass wool, as the molecule sublimator is mounted in the "upside down" position (see Fig. 3.1).

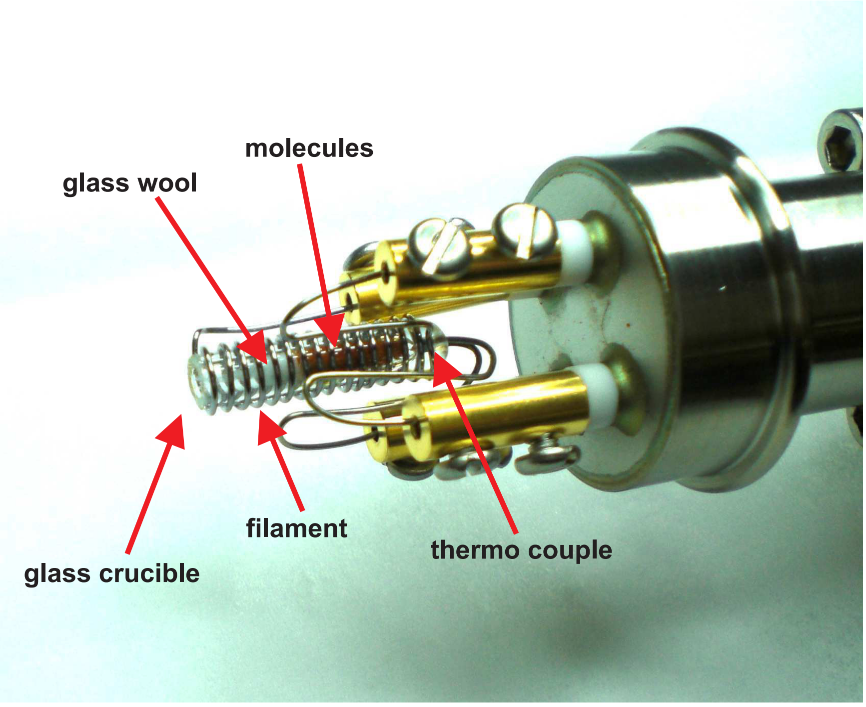

Figure 3.3: The Knudsen cell is heated by a filament made of tantalum, which is contacted via the upper feedthroughs. The temperature can be read out by the nickel-chromium-nickel thermocouple (Type K), melted in the glass cell and connected via the lower feedthroughs.

The molecule sublimators are installed in T pieces, which allow for exchanging the molecules without breaking the UHV in the

Molecule	**Purity**	$\mathbf{T_{sublimation}}$	$\mathbf{r_{deposition}}$
BPCPPCA	97%	335 K	0.01 ML/min
BPDCA	97%	350 K	0.05 ML/min
DCBA	99%	315 K	< 0.01 ML/min
DHBA	> 99%	340 K	0.08 ML/min
DIBA	97%	308 K	< 0.01 ML/min
DISA	99%	360 K	0.05 ML/min
IBA	98%	345 K	0.04 ML/min

Table 3.1: Specified purities for the molecules employed in this thesis as well as the corresponding sublimation temperatures and deposition rates in monolayer (ML) per minute.

remaining system. The Knudsen cell can be moved completely into the chamber via a linear translator and, thus, the distance is only about 90 mm to the sample surface in the manipulator stage.

As shown in numerous experiments, the molecule sublimator allows for reproducible molecule deposition in the submonolayer range [57–73]. The molecules investigated in this thesis are purchased from Sigma-Aldrich (Munich, Germany). For each molecule a new, clean Knudsen cell is used. The molecules are thoroughly outgassed at room temperature for 60 hours prior to deposition under UHV conditions.

Lowest possible deposition rates are used in this thesis to ensure reproducible and well-defined submonolayer coverages. Sublimation temperatures and corresponding rates are plotted in Tab. 3.1. All molecules are sublimated *in situ* onto the freshly prepared calcite surface.

The home-built sample holder for ionic crystals is based on the sandwich design of Omicron. An exploded view of the modified sample holder is shown in Fig. 3.4(a). The crystals are fixed by a clamping mechanism. This clamping mechanism has been developed by [Personal data removed] [74] and adapted to rectangular 4 × 2 mm^2 crystals by [Personal data removed] [49].

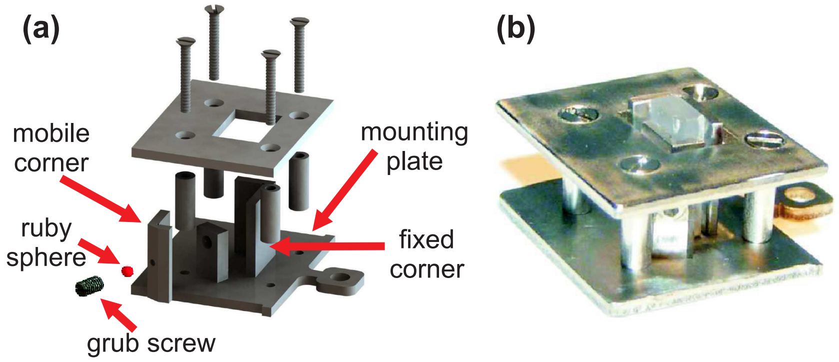

Figure 3.4: (a) An exploded view of the modified sample holder: The mechanism comprises a fixed welded corner on the mounting plate and a mobile corner. The mobile corner is pulled tight by a grub screw and a ruby sphere. (b) Image of the manufactured stainless steel sample holder in the sandwich design. (Adapted from [49])

The crystals used in this thesis are optical quality calcite samples from Korth GmbH (Kiel, Germany). Right after bringing into the UHV chamber, the calcite crystal is annealed to 720 K for two hours for outgasing. The crystal is cleaved at room temperature with a scalpel blade, which is attached to a wobblestick [74]. Then, the sample is heated in the preparation chamber to 600 K for about one hour to remove surface charges.

To anneal the calcite substrate, a pyrolytic boron nitride heater is used, positioned underneath the sample. The temperature is controlled by a thermocouple mounted at the sample stage about 25 mm apart from the sample. The temperature specifications given in this thesis are the corresponding temperatures expected at the calcite sample based on an individual calibration curve supplied by the manufacturer (Omicron, Taunusstein, Germany).

For NC-AFM measurements, n-doped silicon cantilevers (NanoWorld, Neuchâtel, Switzerland) are used (Fig. 3.2(b)), with resonance frequencies of around 300 kHz (type PPP-NCH) excited to oscillation amplitudes of about 10 nm. Prior to their use, the cantilevers were Ar^+ sputtered at 2 keV for 5 min to remove contaminants.

Measurement Electronics and Data Analysis

All experiments are carried out using an electronic from Omicron, namely the Matrix (Omicron NanoTechnology GmbH, Taunusstein, Germany) with the software Matrix V3.0 operated in the frequency modulation NC-AFM mode. The system is equipped with an easyPLL Plus controller and PLL detector from Nanosurf AG (Liestal, Switzerland) for oscillation excitation and signal demodulation.

For FM-KPFM measurements, a digital lock-in amplifier (HF2LI from Zurich Instruments AG, Zurich, Switzerland) with built-in feedback loop is used. The AC voltage with a frequency of around 1 kHz and an amplitude of about 2.3 V is applied to the tip and compensates the resulting electrostatic force with an offset DC voltage also applied to the tip (Kelvin signal).

The Open Source software Gwyddion is employed for data presentation. Using this software, the topographie images were leveled out by the “Three Point Leveling” tool. Numerous detail images were carefully drift-corrected, following a routine published by [Personal data removed] [75], to compensate the distortion by linear thermal drift.

Depending on the feedback loop settings, either frequency shift (Δf) or topography (Z) images are presented here. For the Δf images, the distance feedback loop was set very slow in order to provide quasi constant-height images while still following the overall tilt of the sample surface. Image type as well as slow and fast scan directions are given in the upper right corner in each image by arrows. The images are displayed such that bright correspond to high attractive interaction while dark corresponds to less attractive or even repulsive interactions.

4 Bulk Insulator Substrate: Calcite

Contents

Limestone is one of the sedimentary rocks and was formed by the sedimentation of the shells and skeletons of marine organisms, which consist of calcium carbonate [76]. Pure calcium carbonate is found in nature in the crystalline polymorphs calcite, aragonite and vaterite. Under normal conditions, however, calcite is the thermodynamically most stable form.

Calcite has a density of 2.710 g/cm^3, a Mohs hardness of 3 and is transparent in the visual regime [77]. Calcite is also strongly birefringent [78] and, therefore, is used in optical components [79]. It is the most abundant simple mineral in the geological environment [80]. Calcite is of highest importance within many fields such as biomineralisation [81], environmental geochemistry as well as many industrial applications [82]. In this study, the most stable cleavage plane of calcite is used as the bulk substrate surface.

Calcite (10.4) Surface

Calcite ($CaCO_3$) is a mineral that crystallizes in a rhombohedral crystal structure. The (10.4) surface is the most stable cleavage plane and has a rectangular surface unit cell with dimensions of 5.0×8.1 Å^2 (Fig. 4.1). The surface consists of both the calcium ions and the carbonate groups.

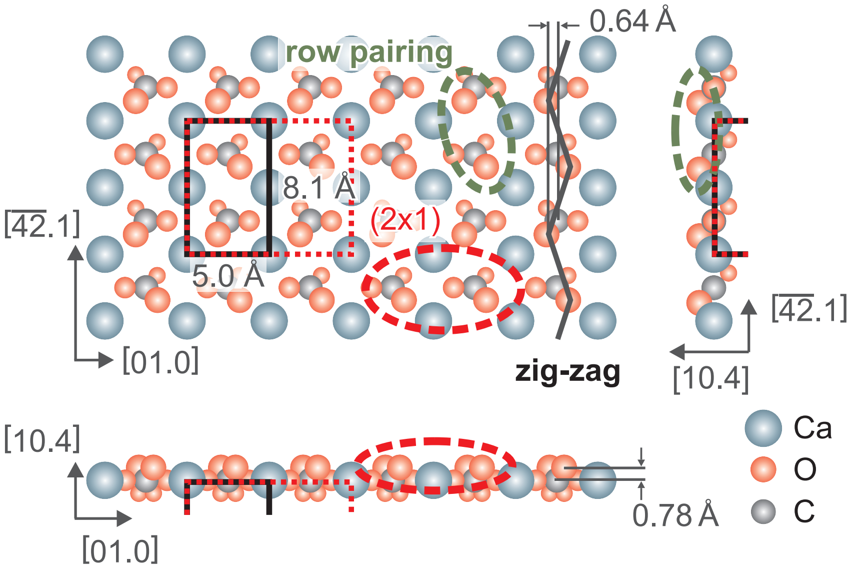

Figure 4.1: The Bulk truncated structure of the calcite (10.4) surface: Surface unit cell, two reconstructions: row pairing and (2 × 1), and the zig-zag of the carbonate groups are marked. (Adapted from [83])

The surface unit cell contains two carbonate groups that are oriented differently, resulting in a zig-zag structure of the topmost oxygen atoms along the $[\overline{42}.1]$ direction. The carbonate groups form an angle of 44.6° to the surface. Thus, the upper oxygen atoms are approximately 78 pm above and the lower oxygen atoms are approximately 78 pm below the plane that is defined by the calcium ions.

Surface Reconstructions

For the (10.4) surface of calcite two surface reconstructions are discussed in the literature (illustrated in Fig. 4.1 and 4.2). The first reconstruction is known as row-pairing. This reconstruction is expressed by the different appearance of the carbonate groups along the $[\overline{42}.1]$ direction, resulting in the impression of two carbonate groups forming a “pair”. The row-pairing reconstruction has been observed for the first time in 1992 with the contact AFM in aqueous solution [84].

A second reconstruction is observed in the [01.0] direction. This (2 × 1) reconstruction was observed for the first time in 1991 by low energy electron diffraction (LEED) [85]. The reconstruction is identified by a brighter appearance of every second maximum in [01.0] direction, resulting in a doubling of the unit cell along this direction.

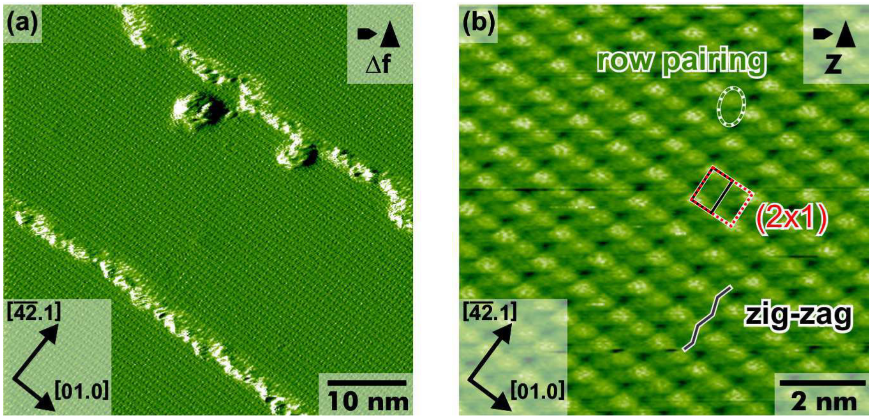

Figure 4.2: NC-AFM images of the bare $CaCO_3(10.4)$ surface at room temperature: (a) Overview image with two step edges running along the [01.0] direction. (b) Detail image with atomic resolution shows row pairing, (2 × 1) and zig-zag of the carbonate groups.

The birefringence of calcite can be used for the exact determination of the crystal directions on the calcite cleavage plane [31]. Light, which passes the calcite crystal perpendicular to the (10.4) surface, splits up along the $[42.\overline{1}]$ direction.

A more detailed and comprehensive description of the bulk structure of calcite and the (10.4) cleavage surface, its reconstructions and the different imaging contrasts in NC-AFM can be found in the thesis of [Personal data removed] [31].

5 Towards On-Surface Reactions on Bulk Insulators

Contents

The bottom-up construction of functional devices from molecular building blocks offers a great potentail in tailoring materials properties and functionality with utmost control. An important step towards exploiting bottom-up construction for real-life applications is creating covalently bonded structures that provide sufficient stability as well as superior charge transport properties over reversibbly linked self-assembled structures. On-surface synthesis has emerged as a promising strategy for creating stable, convalently bound molecular structures on surfaces.

In this chapter, the concept of on-surface synthesis and the current status of molecular self-assembly on insulating surfaces will be presented and illustrated by a literature overview discussing the most recent achievements in the field.

5.1 Reactions on Metals

Fundamental understanding of reactions of molecules on surfaces is of utmost importance for a large number of daily life applications including fields such as catalysis [86] and fabrication of functional surface coatings, e.g., for organic solar cells as well as for smart responsive films. Moreover, covalently linked conjugated molecules allow for efficient electron transport and are, thus, particularly interesting for future molecular electronics applications [87; 88].

On-surface synthesis in ultrahigh vacuum provides a promising strategy for creating thermally and chemically stable molecular structures at surfaces [8; 89; 90]. The two-dimensional confinement of the educts, the possibility of working at higher (or lower) temperatures in the absence of solvent, and the templating effect of the surface bear the potential of preparing compounds that cannot be obtained in solution.

Manipulation of Individual Molecules

A first publication demonstrating the covalent linking of precursor molecules on a surface dates back to the year 2000 [91]. Via a Ullmann-similar [92] homocoupling of iodobenzene to biphenyl on a Cu (111) surface, the covalent connection of individual molecules has been presented. In this case, the carbon-iodine bond has been broken by a voltage pulse with the tip of an STM. As a next step, two closely lying molecular radicals have been pushed together again using the STM tip. Finally, a second voltage pulse has been applied to link the radicals to a biphenyl molecule. An important task has been ascribed to the copper surface, as the phenyl radicals are stabilized by interactions with the metallic surface.

For extended nanostructures, this serial process is very time-consuming and, therefore, unsuitable.

The Parallel Approach

A more promising method has been published in 2007 by Grill *et al.* [93]. Based on bromine-substituted porphyrins covalent linkages have been induced by thermal activation on the Au(111) surface. By homolysis of the carbon-bromine bond, a phenyl radial group has been created. The highly reactive molecule is mobile on the surface and readily reacts with other radicals. It has been demonstrated that dimers, one-dimensional chains or two-dimensional networks can be created by controlling number and position of the bromine atoms (Fig. 5.1).

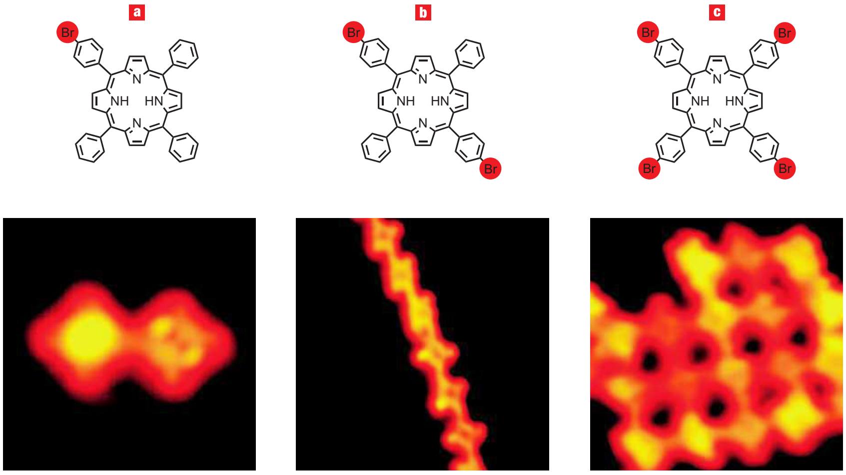

Figure 5.1: Controlling the macromolecular architecture. Results of different monomer building blocks with (a) one, (b) two and (c) four Br substituents. Detailed STM images of the nanostructures formed after activation and connection. (Adapted from [93])

Following this strategy, other examples exist in the literature, inducing covalent coupling by the dehalogenation on metallic surfaces. The coupling of diiodobenzene on Cu(110) has been shown by Lipton-Duffin *et al.* [94]. While iodine in para-position leads to poly(p-phenylene) lines, the polymerization of 1,3-diiodobenzene results in poly(m-phenylene) rows with zig-zag structures or sexiphenylene-macrocycles (Fig. 5.2). The reaction of diiodothiophene to poly(thiophene) was shown by the same authors on the same surface [95].

Other publications reporting thermal activation of halogen-substituted precursor molecules have been demonstrated to allow for fabrication of one-dimensional structures [96; 97] as well as two-dimensional network arrangements [98–100].

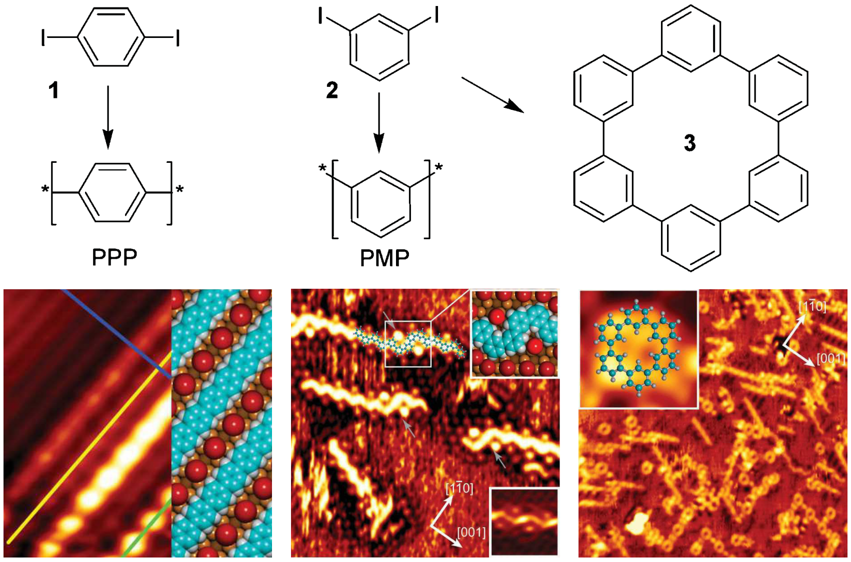

Figure 5.2: Ullmann coupling of diiodobenzene molecules. (1) STM image of 1,4-diiodobenzene rows after annealing. (2) 1,3-diiodobenzene, dosed with the substrate held at 500 K, resulting in lines with zig-zag structure. (3) STM image of PMP oligomers, scanned at 102 K. (Adapted from [94])

An interesting example has been given by the combination of the Ullmann reaction with the Scholl reaction [101]. Following this approach allows for linking bianthryl derivates in two thermally activated steps, a dehalogenation and a cyclodehydrogenation step. This has been used for the polymerization of 10,10'-dibromo-9,9'-bianthryl to graphene stripes on the metal Au(111) surface (Fig. 5.3) [102].

Carbon-carbon bonds can also be realized without the radical formation originating from halide-carbon bond. This has been shown in the polymerization of tetraazaperopyrene by tautomerization [103] on a metallic surface. Furthermore, molecules can be covalently linked by polycondensation reactions on surfaces [104–106]. The creation of extended two-dimensional networks has been shown by using co-sublimated benzenediboronic acid and hexahydroxytriphenylene molecules [107].

Sequential and Site-Specific Reactions

A further step in scientific research is the use of different halogen atoms attached at one molecule. The activation energy for carbon-halogen bond dissociation has different values for differ-

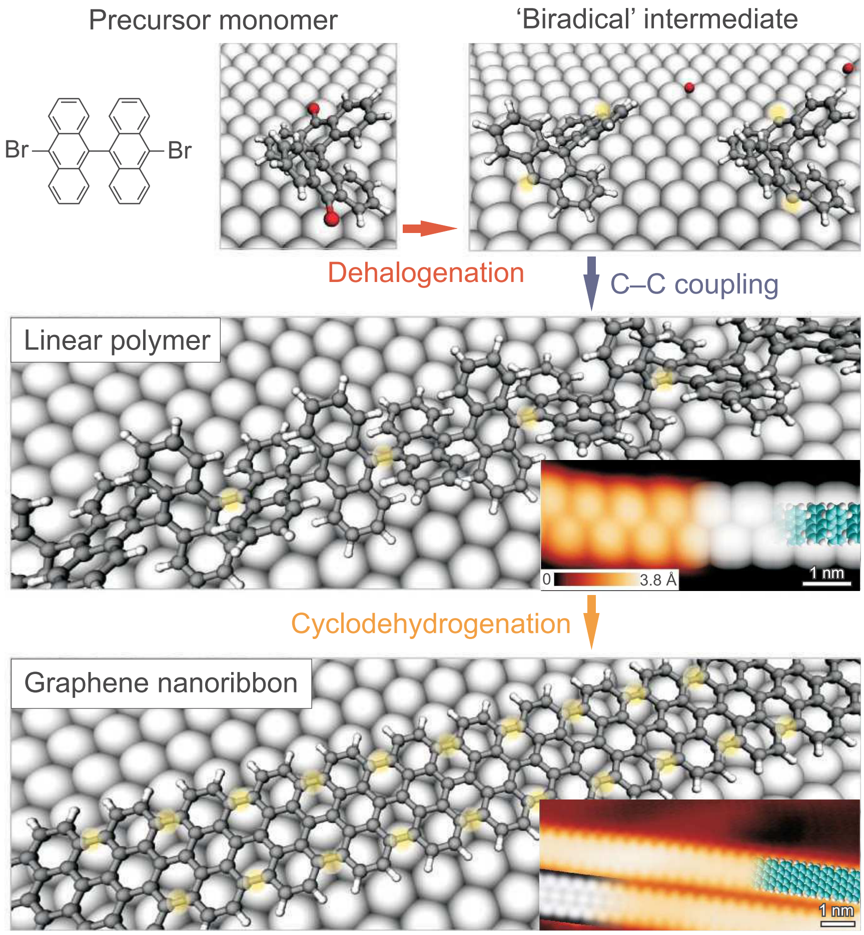

Figure 5.3: Bottom-up fabrication of graphene nanoribbons. Basic steps for surface-synthesis. Top: Dehalogenation during adsorption. Middle: Formation of linear polymers by covalent interlinking. Bottom: Formation of fully aromatic graphene nanoribbons. (Adapted from [102])

ent halogen atoms. This can be exploited for sequential and site-specific reaction: The carbon-iodine bond can be selectively activated first, while the carbon-bromine bond remains intact.

This hierarchical approach has been explored in a recent elegant example using trans-dibromo-diiodo-substituted porphyrins on Au (111) [108]. In a first heating step, one-dimensional rows have been created by cleaving the carbon-iodine bond. A second heating step at a higher temperature has been exploited to break the carbon-bromine bond. This has been shown to result in large network structures by cross-linking the pre-created rows (see Fig. 5.4).

In all these reactions, the surface has been discussed as an important key factor. On the one hand, metals are often seen as a catalyst for coupling reactions [100], particularly the step edges are catalytically highly active [109]. Secondly, metal surfaces offer a comparatively substrate-molecule interaction and, therefore, ideal conditions prevail to prevent the molecule desorption also at higher temperatures. This is of great significance especially for thermally activated on-surface synthesis, since the supplied heat for activation can readily result in desorption instead of reaction of the molecules.

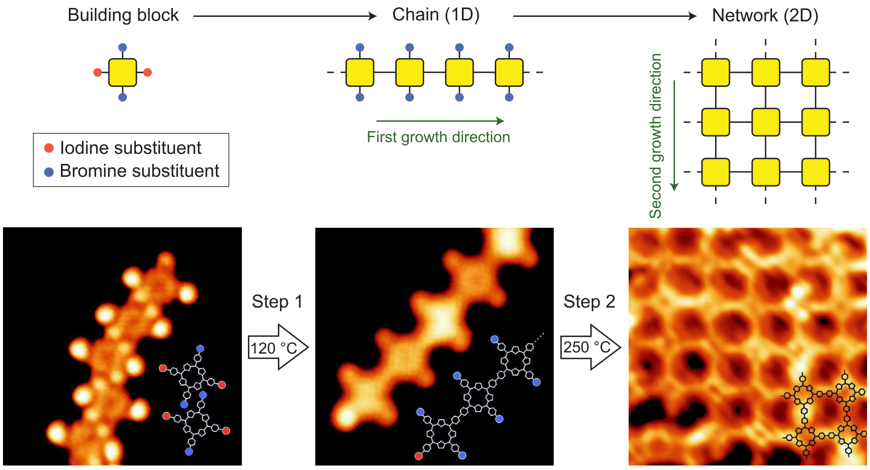

Figure 5.4: Hierarchical growth following sequential thermal activation. Top: Scheme of the sequential activation mechanism. Bottom: STM images of substituted porphyrins, after deposition, after heating to 120°C and after further heating to 250°C. (Adapted from [108])

However, when having molecular electronics applications in mind it would be exceedingly attractive to transfer the on-surface synthesis technique to bulk insulating substrates to prevent electronic coupling to the support surface.

To address this issue, attempts have been made studying the coupling reaction on thin insulating NaCl films on a metallic Ag(100) support [110]. This approach has mainly been followed for the ease of the experiment and to maintain the possibility of performing STM imaging. However, electrical conductivity measurements for this system [111] have demonstrated that a few monolayers of a non-conducting substrate cannot provide sufficient electronic decoupling from an underlying metal.

Therefore, reactions of molecules that are intended for the future use in molecular electronics have to be performed on a bulk insulator substrate.

5.2 Moving to Bulk Insulating Surfaces

However, significant challenges have to be overcome to transfer on-surface synthesis by thermal activation to bulk insulating substrates. While metal surfaces usually exhibit interaction strengths in an energy range that favors molecular self-assembly [112], prototypical insulating surfaces having low surface energies often lack sufficient interaction with adsorbed molecules. As a consequence, application-oriented, bulk insulating materials pose significant challenges when considering them as supporting substrate for molecular electronics.

In terms of molecule-surface interactions, organic molecules usually bind stronger to metallic than to prototypical insulating surfaces [71]. This strong interaction usually originates from a hybridization of organic molecular orbitals with the electronic states of the metal surface [113; 114], and generally supports surface-wetting molecular overlayers. Macroscopic parameters such as the surface energy [115] have been suggested [71] as a first approach for the abstract classification in terms of molecular wetting layers.

The Interaction Challenge

Molecular self-assembly at surfaces benefits from the fact that structure formation is not only governed by intermolecular interactions, but also by molecule-surface interactions [116]. For many prototypical insulating substrate surfaces, the low surface energy has been shown to result in dewetting and molecular crystal formation rather than substrate templating. Thus, exploiting the full potential of molecular self-assembly on insulating surfaces requires exploring ways to increase the molecule-surface interaction.

Due to the absence of sufficiently strong and specific molecule-surface interactions, the molecules diffuse at room temperature and only nucleate at step edges [117–121]. One of the first observation of this behavior has been made for PTCDA molecules on the KBr(001) surface (Fig. 5.5) [119]. In this work, the weak influence of the substrates has been confirmed by fact that the molecules aggregate into a structure that closely resembles the molecular bulk crystal. Later, further examples of a weak molecule-substrate interaction have been presented leading to dewetting and often molecular bulks structure formation [122–126].

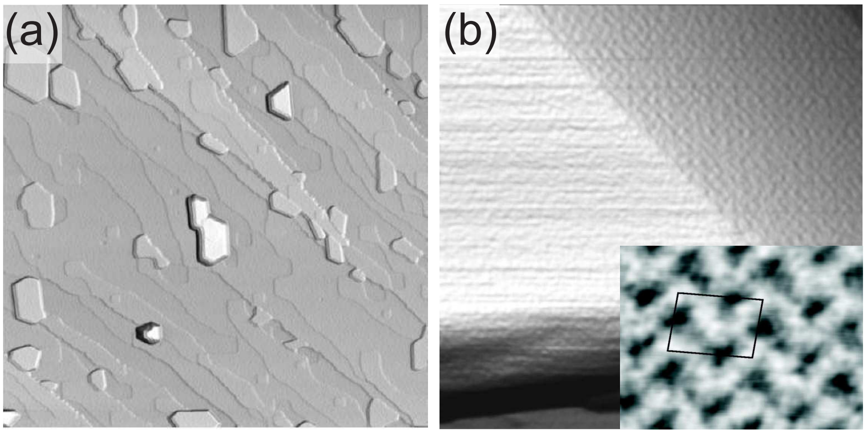

Figure 5.5: Arrangement of PTCDA molecules on a KBr(001) surface. (a) Overview of a large area (2 μm)^2 of the KBr surface covered with PTCDA islands. (b) Part of an individual PTCDA crystallite island; Molecular resolution on the top (inset). (Adapted from [119])

The molecules of the before presented systems are mainly physisorbed on the dielectric surfaces, mainly bonded by weak van-der-Waals interactions. Thus, weak molecule-surface interactions have been identified as major obstacle for transferring molecular self-assembly principles from metallic to insulating substrates.

Anchoring the Molecules

Soon after the first experiments, strategies have been explored to enhance the templating effect of the surface on the molecular structure formation. As a first attempt, the substrate surface has been patterned to guide the molecule nucleation at step edges and surface pits [127–133]. Upon irradiation with an electron beam, monolayer deep pits can be produced on KBr(001) [134], which can either trap full molecular islands [133] or which step edges can act as nucleation sites for subsequently deposited molecules [127].

Electrostatic interactions can be exploited for anchoring the adsorbed molecules on ionic crystal surfaces. Matching the intermolecular charge distribution to the ionic crystal lattice provides a possibility for enhancing the molecule-surface interaction. Along this line, molecules bearing a large dipole moment have been explored for increasing the electrostatic interaction with the surface [41; 62; 127; 131; 135–138]. This strategy has been followed for the formation of up to 600 nm long molecular wires made of a perylene derivative on KBr(001) (Fig. 5.6) [139; 140].

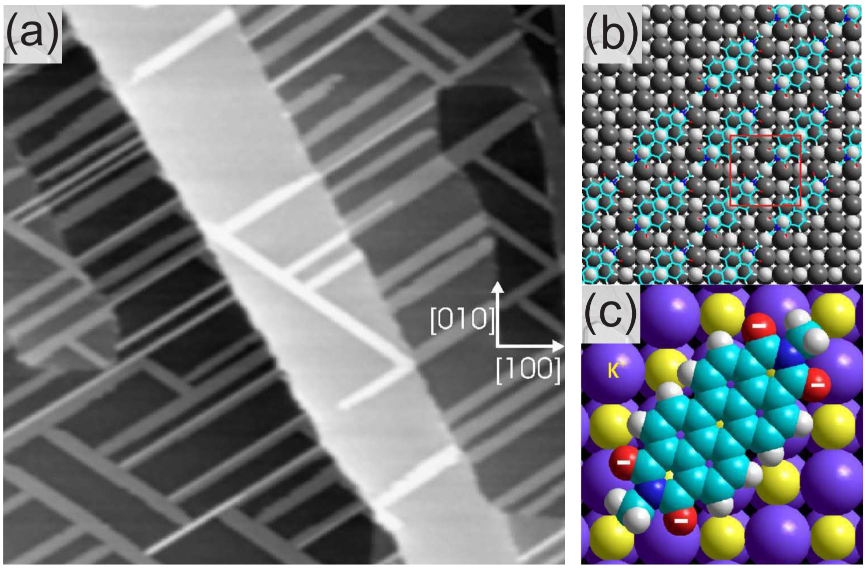

Figure 5.6: DiMe-PTCDI wires on KBr(001). (a) Image shows molecular wires of DiMe-PTCDI; the size of the image is $(400\,\mathrm{nm})^2$. (b) Proposed (2 × 2) superstructure based on calculation and experimental data. (c) Minimum energy position of a single DiMe-PTCDI molecule on KBr. (Adapted from [139])

A cooperative mechanism of molecule anchoring has been found for cytosine on $CaF_2(111)$ [62]. In this example, the increased molecule-surface interaction of individual molecules together with the arrangement in three-membered hydrogen-bonded rings eventually results in immobilization of trimer clusters on the surface (Fig. 5.7).

Besides the strength and the range of the binding, the specific nature of the interactions constitutes the key controlling parameter for molecular self-assembly. While van-der-Waals interaction forces are typically weak and unspecific, for example hydrogen bonds are very specific and directed. Several dielectric surfaces allow for hydrogen bond formation. As an example, calcite(10.4) can act as a proton acceptor, thus providing very

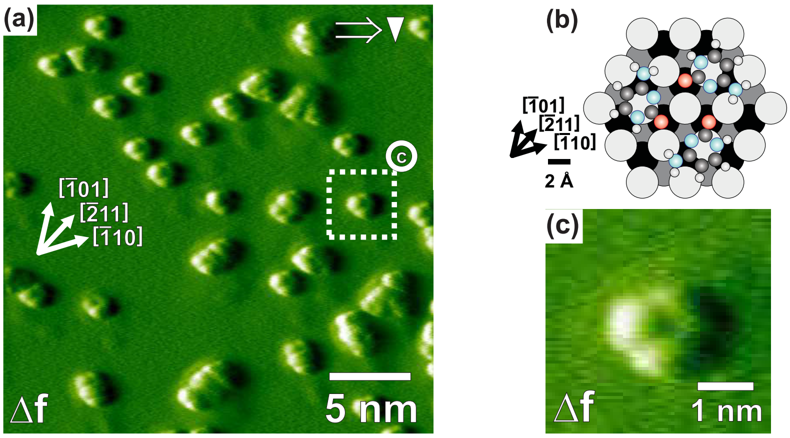

Figure 5.7: Arrangement of PTCDA molecules on a KBr(001) surface. (a) High-resolution image: Homogeneously distributed clusters are observed. (b) Optimum adsorption position of the trimer structure as obtained by DFT calculations. (c) Zoom into the trimer structure in (a). (Adapted from [62])

specific anchoring sites for proton donor molecules, such as carboxylic acid groups [72].

Another important aspect in molecule-surface anchoring is matching the molecular structure to the substrate periodicity, as has been indicated by the comparison of the adsorption structure of a stilbazolium derivative on different insulating surfaces [137]. Considering a given insulating material as supporting substrate, the complementary strategy is to adjust the molecular building blocks to the substrate of interest. The molecular core can be adjusted to match the substrate periodicity [141; 142].

An example is given by the adsorption structure of terephthalic acid (TPA) [72] on calcite(10.4). In this case, the interaction with the substrate is governed by the interaction of the carboxylic acid groups with the substrate carbonate groups. The molecule is equipped with two carboxylic acid groups in para position. TPA forms a well-ordered (2×2) superstructure, however, islands are mobile at sub-monolayer coverages (Fig. 5.8(a,b)).

Furthermore, a concept for increasing the influence of the surface is increasing the number of functional groups that provide an interaction with the surface. This has been the driving force in many attempts in literature [41; 138].

For the calcite(10.4) surface, an example is changing the number of carboxylic acid groups at a benzene core from two as in TPA to three as in trimesic acid (TMA) [72]. In the close-packed island

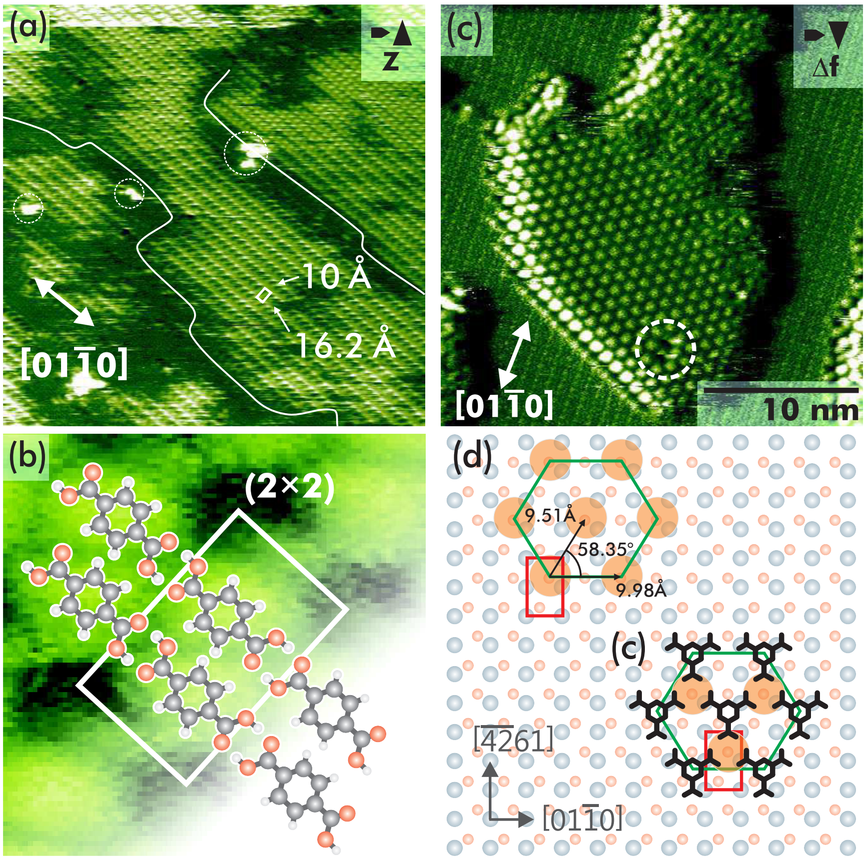

Figure 5.8: Two aromatic carboxylic acids, namely TPA and TMA, on the calcite surface. (a,b) TPA: NC-AFM images taken at a sample temperature of 300 K with immobile features and a detailed image including a structural model. (c,d) High-resolution Δf image of TMA with molecular resolution and Model of the molecular adsorption structure are shown. (Adapted from [72])

(the so-called flower motif), the TMA molecules adopt equivalent adsorption positions in a c(2 × 2) superstructure (Fig. 5.8(c,d)). In this configuration, all three carboxylic acid groups can interact with the substrate, resulting in a more stable configuration as compared to the TPA islands. It is important to note that the TMA structure is slightly compressed as compared to the perfectly hexagonal flower motif configuration, clearly demonstrating the templating influence of the substrate.

Consequently, successful examples of molecular self-assembly on insulating surfaces are based on tailoring the interaction type and the detailed molecule-surface matching. Although, the incorporation of strong covalent bonds in the structure stabilization becomes inevitable for the formation of application-oriented robust molecular structures.

6 Substrate Templating vs Molecular Interactions

Contents

In this Chapter, I report on molecular self-assembly of biphenyl-4,4'-dicarboxylic acid (BPDCA) on $CaCO_3$(10.4) under ultra-high vacuum conditions. Two-dimensional, ordered islands are obtained upon deposition at room temperature. High-resolution images of the molecular islands reveal an ordered inner structure. A detailed analysis of this structure exhibits inter-row distances that are multiples of the calcite unit cell dimension along the [01.0] direction, clearly demonstrating the templating effect of the substrate. In between the rows, a different molecular structure is coexisting with the molecules aligning *head-to-tail*. This structure is explained by intermolecular hydrogen bond formation very similar to the BPDCA bulk structure.

Introduction

The molecular self-assembly on surfaces is governed by a subtle interplay between intermolecular and molecule-surface interactions [143]. Thus, it is important to balance these two interactions, which is frequently achieved for molecular self-assembly on metallic surfaces [116]. On insulating substrates and thin insulating films, however, molecule-surface interactions have been found to be considerable reduced as compared to metallic substrates (Chap. 5).

This is the reason only very few examples exist so far demonstrating the formation of a stable molecular wetting layer on an insulating surface. Promising strategies for insulating surfaces include the use of the high surface energy substrates such as calcite [71], the optimizing of the geometrical match for the molecular dimensions to the crystal lattice [141; 142] and the anchoring of molecules by functional end groups on an ionic crystal [62].

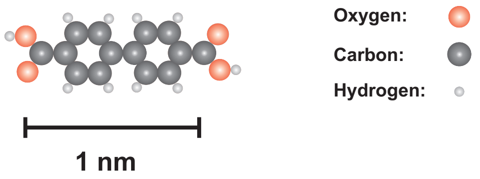

Figure 6.1: Model of the biphenyl-4,4'-dicarboxylic acid (BPDCA) molecule.

Here, I present a system that directly expresses the balance between intermolecular and molecule-surface interactions by the coexistence of two different molecular structures on the surface. Using NC-AFM imaging under UHV, I study the molecular self-assembly of BPDCA on the most stable cleavage plane of calcite, $CaCO_3(10.4)$ (Chap. 4), at room temperature. Ordered rows of molecules aligned *side-by-side* running along the $[\overline{42}.1]$ crystallographic direction demonstrate a significant molecule-surface interaction that can be explained by an excellent geometrical match of the molecular structure to the substrate dimensions. In between theses rows, a second structure is formed with the molecules aligning *head-to-tail*, closely resembling the molecular bulk structure. My results, thus, indicate that molecule-substrate and intermolecular interactions are of similar strength in the presented system.

Self-assembly of BPDCA

A representative NC-AFM topography image obtained after deposition of approximately a half monolayer (ML) BPDCA molecules onto $CaCO_3(10.4)$ held at room temperature is given in Fig. 6.2(a). In this image, molecular islands are observed that are separated by streaky regions. The islands exhibit an elongated shape with typical dimensions of few tens of nanometer in the [01.0] direction and of 10 to 30 nm in $[\overline{42}.1]$ direction. The apparent height of the islands is approximately 0.25 nm, suggesting that the islands are formed by flat-lying molecules.

The edges of the islands appear fuzzy, which is a typical sign for attachment and detachment of molecules at the islands' periphery. The streaky regions and the existence of the islands indicate that individual molecules (i) can detach from the islands and (ii) have substantial mobility on the surface at room temperature to form a two-dimensional gas-like phase.

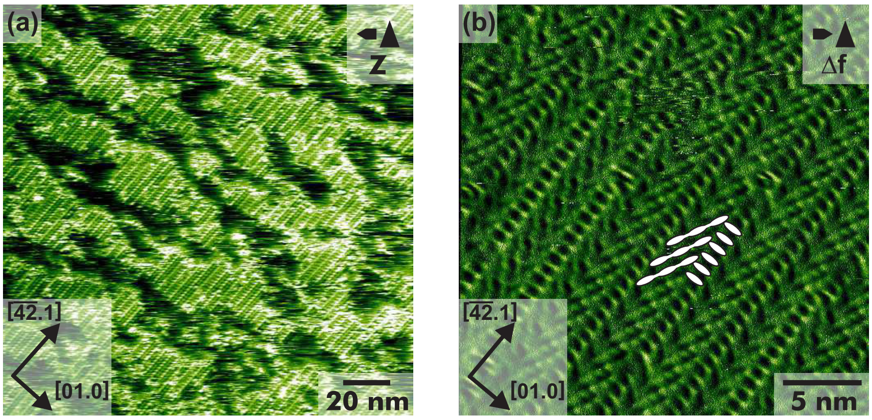

Figure 6.2: NC-AFM images showing BPDCA islands on $CaCO_3(10.4)$ held at room temperature. (a) Topography image exhibiting BPDCA islands separated by streaky regions.
(b) Frequency shift image taken on a molecular island, revealing the internal structure. Molecules aligning in *side-by-side* rows and *head-to-tail* rows are indicated by ellipses.

An internal structure is revealed on the islands, which is predominantly composed of rows running along the $[\overline{42}.1]$ direction. The inner structure is resolved in the frequency shift image shown in Fig. 6.2(b). Most prominently, the ordered rows running along the $[\overline{42}.1]$ direction are observed to be composed by features that fit in size to flat-lying, individual molecules aligned *side-by-side*. Interestingly, the separation of these *side-by-side* rows along the [01.0] direction is not equidistant, but shows different distances. The area in between the *side-by-side* rows is occupied by another structure with the molecules aligning *head-to-tail*, forming a characteristic angle of 27° with respect to the *side-by-side* row structure.

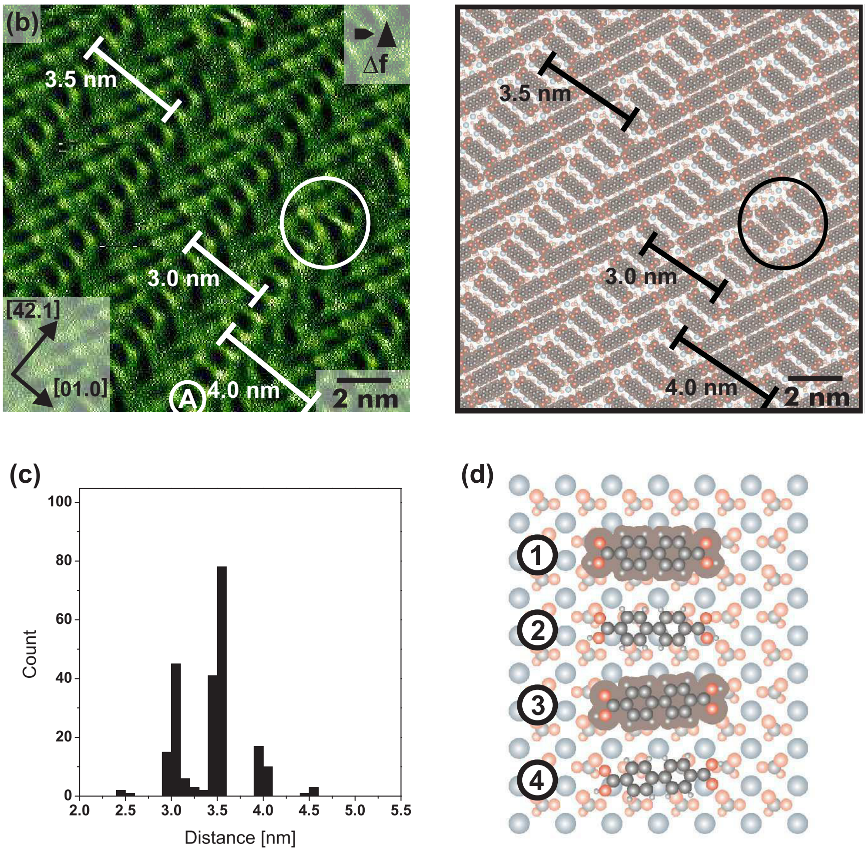

Figure 6.3: Detail analysis of a BPDCA island. (a) Drift-corrected frequency shift image: A defect (circle) and three different inter-row distances are marked. (b) Model visualizing the molecular arrangement as present in (a). (c) Histogram showing the distribution of 224 inter-row distances. (d) Possible adsorption positions of the molecules within the *side-by-side* rows with respect to the underlying substrate.

To analyze the molecular islands in more detail, a high-resolution frequency shift image is given in Fig. 6.3(a) along with a model for the molecular arrangement shown in Fig. 6.3(b). Three different inter-row distances are marked within this image, exhibiting distances of 3.0, 3.5 and 4.0 nm, respectively. Interestingly, these distances appear as multiples of the unit cell dimension of 0.5 nm along the [01.0] direction, indicating that the surface structure has a decisive influence on the formation of these *side-by-side* rows.

In order to quantify this observation, I have analyzed a total number of 224 inter-row distances from four independent large-scale images. The resulting distance histogram is shown in Fig. 6.3(c). As can be seen, a discrete distribution is, indeed, obtained exhibiting inter-row spacings that are multiples of the unit cell dimension of 0.5 nm. Moreover, a clear maximum at an inter-row spacing of 3.5 nm is revealed, which will be explained later.

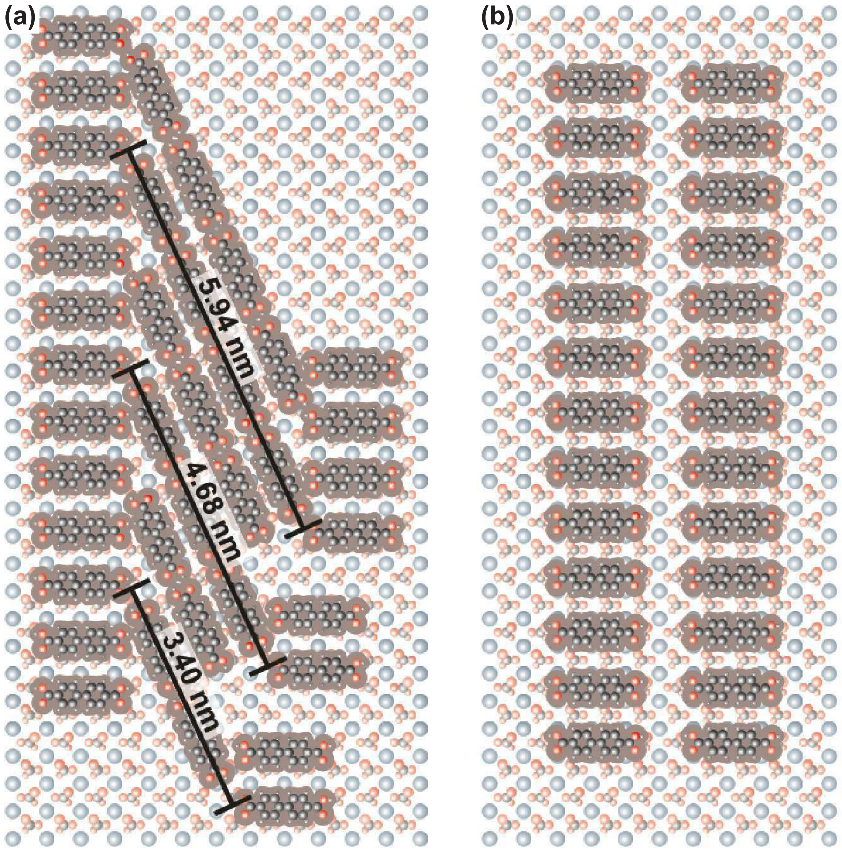

Figure 6.4: Models illustrating possible molecular arrangements. (a) Model showing both the *side-by-side* rows and the *head-to-tail* rows. Different lengths of *head-to-tail* rows are indicated, composed of two, three and four molecules, respectively. (b) Closest alignment of a pure *side-by-side* row phase, revealing a large spacing between the molecular rows.

Substrate Templating: Two Positions

From the images, I can deduce the orientation of the molecules within the *side-by-side* rows with respect to the underlying calcite lattice. The absolute adsorption position is, however, not obtained experimentally as simultaneous imaging of the molecular islands and the calcite lattice was hampered by the molecular mobility at room temperature. Based on simple electrostatic considerations, I can identify two very likely adsorption positions that might be present in the experimental data shown in Fig. 6.3(a). I want to stress, however, that more elaborate calculations are required for confirming the qualitative discussion made here. Nevertheless, my conclusions regarding the molecular arrangement and the most likely inter-row spacing remain valid regardless of the precise adsorption.

Two obvious adsorption positions of the molecules within the *side-by-side* rows are shown in Fig. 6.3(d). The models are based on the fact that the molecule-surface interaction is steered by the interaction of the carboxylic groups with the surface [144]: The hydrogen atom of the carboxylic groups anchors to a surface oxygen atom via a hydrogen bond, while the partially negatively charged carbonyl oxygen atom is positioned close to a surface calcium cation. When aligning the molecular axis along the [01.0] direction as observed experimentally, the size of the molecule allows for accommodating both carboxylic groups on top of equivalent adsorption positions. This explains the strong surface templating effect, as both carboxylic groups can attain an energetically favorable adsorption position.

Depending on the position of the hydrogen atom, two slightly differing adsorption positions can be obtained. In the upper part of Fig. 6.3(d), two molecules are shown (labeled 1 and 2) with both hydrogen atoms arranged in *cis* configuration. In this case, the molecule can accommodate such that main axis of the molecule is exactly perpendicular to the *side-by-side* row direction.

However, a second option would be to rotate one carboxylic acid around the C-C axis with the hydrogen atoms adopting *trans* configuration (shown in the molecules labeled 3 and 4). In this case, the molecular axis would form an angle of approximately 5° with respect to the *side-by-side* row. This slightly rotated configuration might be evident for the rows shown in Fig. 6.3(a) except for the one marked with an A.

The ordering within the rows is very well-pronounced, and defects can be found only rarely. One defect is shown in Fig. 6.3(a) (marked by a circle), which originates from a shift of one *side-by-*

side row by 0.5 nm. The linking molecule appears to bridge the two rows in a tilted fashion.

Intermolecular Interactions

The area in between the rows is occupied by molecules forming a distinctly different pattern. In this structure, the molecules are found to align *head-to-tail*, such that the carboxylic groups face each other. This arrangement allows for hydrogen bond formation between the carboxylic groups and is very close to what is expected in the BPDCA bulk structure [145]. The observed ordering is a clear sign for the fact that the molecules are not deprotonated yet, which is in agreement with the pK_a values of 3.5 and 4.3, respectively [66].

The length of these *head-to-tail* rows differ depending on the available space between the above mentioned *side-by-side* rows running along the $[\overline{42}.1]$ direction. For inter-row distances of 3.0, 3.5 and 4.0 nm, an alignment of two, three and four molecules is revealed, respectively, as shown in Fig. 6.4(a) and listed in Tab. 6.1.

The “head” and “tail” molecules from a *head-to-tail* row arrange in a way that they can form hydrogen bonds towards the oxygen atom of the neighboring molecule within the adjacent *side-by-side* row, while the partially negatively charged oxygen atom is close to a surface calcium cation. This configuration explains the experimentally observed characteristic angle of 27°.

To analyze the obtained inter-row spacing histogram from Fig. 6.3(c) in more detail, I calculated the length of a *head-to-tail* row and compared this length with the available space between the *side-by-side* rows.

To estimate the length of a *head-to-tail* row, I added the estimated molecule length (O-O distance: 1.15 nm [145]) and hydrogen bonds length (O-O distance: 0.27 nm [146]) as listed in the third column in Tab. 6.1. I want to stress that (i) these numbers do not include the interaction with the surface and (ii) all hydro-

***side-by-side* inter-row distance**	**number of molecules in *head-to-tail* row**	***head-to-tail* row length calculated**	**space available (distance)**
2.5 nm	1	1.69 nm	1.94 nm
3.0 nm	2	3.11 nm	3.40 nm
3.5 nm	3	4.53 nm	4.68 nm
4.0 nm	4	5.95 nm	5.94 nm
4.5 nm	5	7.37 nm	7.21 nm

Table 6.1: Comparison of *head-to-tail* row lengths with available space for the respective *side-by-side* inter-row distances.

gen bonds were considered to be of the same length, regardless of their nature (within the *head-to-tail* row or between *head-to-tail* row and *side-by-side* row). Thus, the given length values represent a rough estimate only.

I compare these lengths with the space available between the *side-by-side* rows (considering the distance between two oxygen atoms as indicated in Fig. 6.4(a)) listed in the fourth column. As can be seen, for *head-to-tail* rows consisting of only one or two molecules, the available space is considerably larger than the estimated molecule length, indicating that the interaction of the *head-to-tail* rows with the *side-by-side* rows is weak or even absent.

For *head-to-tail* rows consisting of five molecules, the distance between the *side-by-side* rows is smaller than what would be needed to easily accommodate the *head-to-tail* rows. For *head-to-tail* rows consisting of three and four molecules, the available space is very close to the estimated space required, suggesting that these *head-to-tail* rows should be favored. Indeed, my experimental results reveal a maximum at an inter-row distance of 3.5 nm in Fig. 6.3(c). I, therefore, explain the maximum in the histogram in Fig. 6.3(c) by a favorable size match in the inter-row distance and the space required for the *head-to-tail* rows.

Finally, I comment on the situation that would arise in the absence of the *head-to-tail* rows. Because of the well-defined adsorption position of the molecules within the *side-by-side* rows, the most close-packed arrangement is associated with a rather large spacing between the molecular rows, as shown in Fig. 6.4(b). Thus, no inter-row interaction is expected in this configuration, which is unfavorable compared to the situation where the *head-to-tail* rows interlink the *side-by-side* rows.

Summary and Conclusions

The coexistence of two different molecular adsorption configurations is shown upon deposition of BPDCA on $CaCO_3(10.4)$. A very pronounced row structure is revealed that is formed by flat-lying molecules aligned *side-by-side*, resulting in rows running along the $[\overline{42}.1]$ direction. In this configuration, the molecules show a favorable adsorption position with both carboxylic groups anchoring toward the calcite surface. This strong surface templating effect is possible because of the excellent size match of the molecule to the substrate lattice.

Besides this structure, another structure is coexisting, formed by rows that are composed of molecules aligned *head-to-tail*. In this configuration, the molecules can form hydrogen bonds as present in the bulk structure. The coexistence of these two different adsorption structures indicates a subtle balance between substrate templating on the one hand and molecular bulk crystal formation on the other.

7 Visualization of Molecule Deprotonation

Contents

In this Chapter, the deprotonation of 2,5-dihydroxybenzoic acid (DHBA) deposited onto $CaCO_3(10.4)$ held at room temperature is reported. After deposition, the molecules form two coexisting phases, a transient striped phase and a stable dense phase. Detailed analysis indicates the transient striped phase being a bulk-like phase, which requires hydrogen bonds between the carboxylic acid moieties to be formed. With time, the striped phase transforms into the dense phase, which is explained by the deprotonation of the molecules. The deprotonation step is directly confirmed by Kelvin probe force microscopy that unravel the change in the molecular charge.

Introduction

Following the discussion on the interplay between substrate templating and intermolecular interactions in the previous Chap. 6, a fundamental understanding of adsorption and molecule-surface interactions are of utmost importance for anchor molecules. Only very recently, on-surface chemical transformations including deprotonation [147–149] have been addressed, revealing important insights into fundamental reaction steps. For many applications, however, it becomes increasingly interesting to extend the knowledge gained on metallic surfaces to bulk insulator substrates, as many applications, e.g., catalysis and organic opto-electronics, require non-metallic and electronically insulating support materials.

Interestingly, comparatively little is known so far about molecule-surface interactions in relation to chemical transformations of organic molecules on electrically insulating surfaces (Chap. 5). By making use of the KPFM technique, NC-AFM allows for directly mapping the charge state of adsorbates [39] as well as the charge distribution within a single molecule [40]. Only very recently, this technique has been applied for investigating organic molecules on bulk insulator surfaces, e.g., for differentiating two adsorption geometries of triphenylene derivatives on KBr(001) [41].

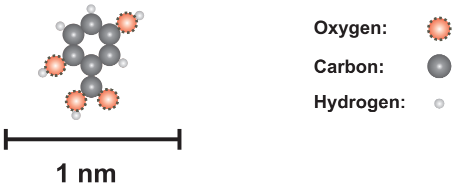

Figure 7.1: Model of the 2,5-dihydroxybenzoic acid (DHBA) molecule.

Here I benefit from both, the high-resolution imaging capability of NC-AFM and the possibility to detect changes in the local charge distribution by KPFM for the direct visualization of the deprotonation step of DHBA on the insulating calcite substrate (Chap. 4).

Upon deposition onto the calcite (10.4) surface held at room temperature, two molecular structures are observed to coexist. One of these structures closely resembles the molecular bulk structure, which is stabilized by intermolecular hydrogen bonds, thus giving clear evidence for the fact that the molecules are still in the protonated state. Interestingly, this structure is observed to transform with time into the second structure, which is characterized by a dense packing of upright standing molecules.

This configuration can be explained by deprotonated molecules anchoring towards the surface calcium cations. Thus, I am able to directly follow the deprotonation step of a carboxylic acid moiety on the calcite surface *in situ*, which is of great importance for elucidating molecular-scale details of molecular reactivity on surfaces within fields such as on-surface synthesis [150] and catalysis [151].

Structure Formation of DHBA Molecules

Upon submonolayer deposition of DHBA onto a $CaCO_3(10.4)$ substrate held at room temperature, initially two distinctly different molecular phases coexist on the surface, as shown in Fig. 7.2(a). In this image, the majority of the surface is covered by a striped phase, which is characterized by islands formed from molecular double rows running along the $[\overline{42}.1]$ substrate direction. The outer shape of these islands exhibits a large number of kink sites. Moreover, several defects formed by missing molecules are evident within the striped phase.

This striped layer constitutes a transient phase which transforms with time into a coexisting second phase. In the upper part of Fig. 7.2(a), an island of this second phase is seen, formed by densely packed molecules. The outline of this dense phase is less fragmented than those of the striped phase, however, kinks and vacancy islands are revealed for the dense phase as well.

A closer view of both the striped and the dense phase is given in Fig. 7.2(b). In the lower part of this image, an island of the striped phase is shown, clearly revealing the molecular double-row structure and a single-molecule defect (circle). The upper part of Fig. 7.2(b) is covered by an island of the dense phase, unraveling a rectangular internal structure that is characterized by a dense packing of molecules.

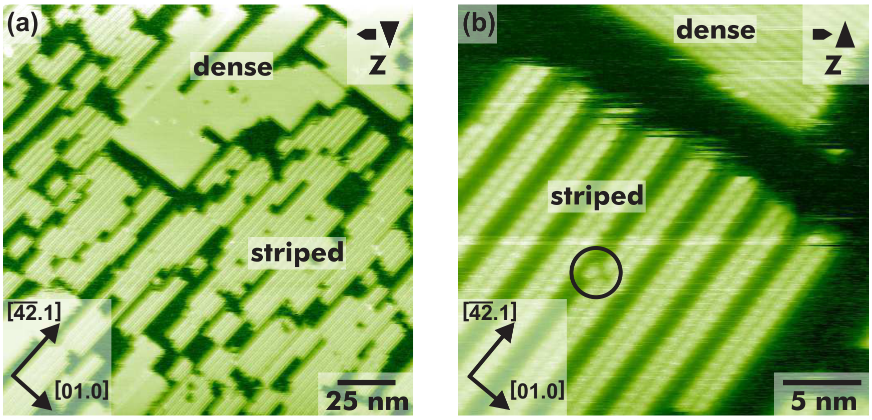

Figure 7.2: Coexisting molecular structures after deposition of DHBA onto $CaCO_3(10.4)$:
(a) Overview image revealing two coexisting phases, a defect-rich striped phase and a dense phase. (b) Closer view of both, the striped phase (lower part) and the dense phase (upper part).

To elucidate the molecular arrangement within both phases, I analyze high-resolution NC-AFM images of the striped and dense phase shown in Fig. 7.3(a) and (b). In Fig. 7.3(a), the striped phase is presented, revealing an internal structure within the bright molecular rows as well as in between these rows. The different brightness indicates this structure being formed by molecules adopting different adsorption geometries.

Striped and Dense Phase in Detail

The data suggest that the area in between the bright rows is covered by flat-lying molecules, while the molecular rows are formed by molecules with the molecular plane not parallel to the surface, resulting in an apparent height of approximately 0.4 nm. This motif closely resembles the molecular arrangement of the bulk structure in the ordered form [152] as superimposed in Fig. 7.3(c).

In the ordered bulk structure, the molecules pair to dimers by hydrogen bond formation between the carboxylic groups. These dimers arrange in rows having alternating dimer orientations. The inter-dimer interaction is governed by hydrogen bond formation and by $\pi-\pi$ interaction of adjacent molecules. The different dimer orientation is reflected in my images by the alternate appearance of flat-laying molecules and molecules being oriented with their main axis parallel to the surface but having the molecular plane oriented upright, as illustrated in Fig. 7.3(c).

The striped phase constitutes a (6 × 1) superstructure, having unit cell dimensions of 2.99 nm and 0.81 nm along the [01.0] and [$\overline{42}$.1] direction, respectively. Compared to the bulk structure, this superstructure corresponds to an extension of 13 and 8 % along these two directions, indicating the subtle influence of the substrate on the resulting bulk-like structure. The fact that the striped phase constitutes a bulk-like structure provides experimental evidence for the conclusion that the molecules are still protonated within the striped phase, as the above-mentioned dimerization requires the carboxylic groups to be protonated.

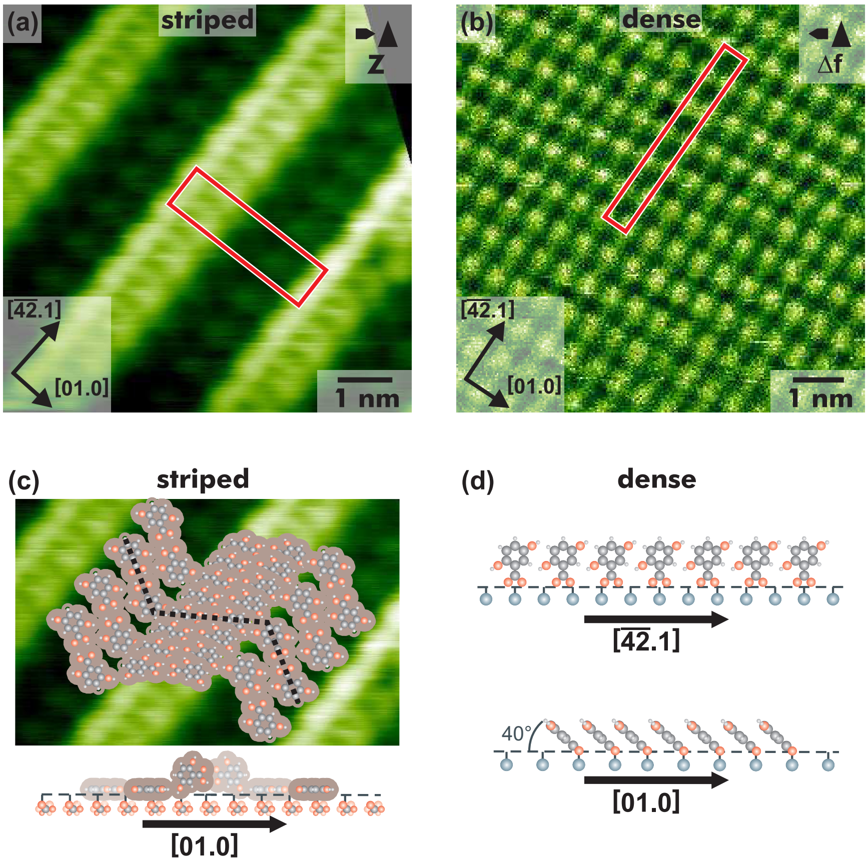

Figure 7.3: (a) Drift-corrected high-resolution image of the striped phase, unraveling molecular double rows running along the [$\overline{42}$.1] direction and a molecular sub-structure in-between the rows. The (6 × 1) unit cell is marked.
(b) Drift-corrected high-resolution image of the dense phase, exhibiting a (1 × 5) superstructure.
(c) Striped phase with superimposed model of the molecular bulk structure. The dashed line marks the molecules shown in the model at the bottom of the subfigure. (d) Model of the molecular arrangement within the dense phase.

Interestingly, with time the striped phase transforms into the dense phase, which remains as the only structure present after waiting for several hours to days. Alternatively, the sample was annealed to 440 K, resulting in the same situation of the dense phase remaining exclusively on the surface. A high-resolution image of this phase is given in Fig. 7.3(b), exhibiting a densely packed structure having a rectangular unit cell with dimensions of 0.5 nm x 4.1 nm, corresponding to a (1×5) superstructure. The comparatively small lateral size of the individual features suggests this structure to be formed by molecules having their main axis oriented upright with respect to the surface normal as given in the model in Fig. 7.3(d). In this configuration, hydrogen bonding is no longer possible, providing a first indication for the deprotonation of the molecules.

Moreover, the upright position can be readily explained by electrostatic interaction of deprotonated molecules with the surface calcium cations as detailed in the following. Along the [01.0] direction, the molecules follow the substrate periodicity, allowing for linking of the carboxylate with the substrate calcium cations. A further stabilization of this structure would be $\pi-\pi$ stacking of adjacent molecules along the [01.0] direction. In order to optimize the $\pi-\pi$ stacking distance, the molecules might tilt to bring the rings close to each other. To reach a favorable $\pi-\pi$ stacking distance of 0.34 nm in the parallel-displaced configuration [153], a tilt angle of approximately 40° would be favorable as obtained from simple trigonometry. This tilt would result in a reduction in molecular height from an upright height of approximately 0.77 nm to around 0.52 nm, which is reflected by the experimentally observed height of 0.4 nm.

Using Kelvin Probe Force Microscopy

However, as height measurements with AFM rely on interaction forces, the height of chemically different species cannot be compared directly [154]. Thus, the measured height can only provide an indication but no clear-cut experimental evidence for the proposed tilted geometry. Along the $[\overline{42}.1]$ direction, a compromise between molecule-surface interaction and intermolecular hydrogen bonding results in a molecular spacing that is responsible for a (1×5) superstructure.

In the proposed geometry, six molecules are placed with their carboxylate groups atop of ten Ca cations as shown in Fig. 7.3(d). This results in non-equivalent adsorption positions along the $[\overline{42}.1]$ direction. The NC-AFM results do not show different molecular appearance, which might be explained by two aspects. First, the NC-AFM might be sensitive only to the top part of the molecules, which is probably rather homogeneous. Second, the different adsorption positions might be compensated for by both molecule and surface relaxations.

Regarding the intermolecular interaction along the $[\overline{42}.1]$ direction, a closest distance between the hydrogen atoms of approximately 0.15 nm is revealed. This geometry might be optimized by a slight rotation of the benzene ring around the C-C bond between the carboxylate group and the benzene ring. These details are, however, beyond the scope of this simple model based on the NC-AFM images alone.

To confirm the above made tentative assignment of the dense phase being the deprotonated species, I made use of KPFM, allowing for a direct measurement of dipole moments and local charges. Deprotonated DHBA is negatively charged and, thus, should provide a clear signal in KPFM measurements [155]. Protonated DHBA, on the other hand, carries a dipole (about 5 Debye [156]) but is overall neutral.

Consequently, for the protonated species I expect a less pronounced Kelvin signal as compared to the deprotonated molecules. In the absence of net charges, possible KPFM contrast can originate from surface charge transfer or intramolecular charge distribution [40]. Resolving this charge distribution is rather difficult with KPFM because of the reduced lateral resolution of KPFM compared to NC-AFM [48].

However, in some cases I succeeded in resolving an internal structure within the striped phase as discussed below. An NC-AFM topography image and the corresponding KPFM image are shown in Fig. 7.4(a) and (b). The KPFM voltage of the bare calcite substrate is set to zero. The voltage required to compensate the

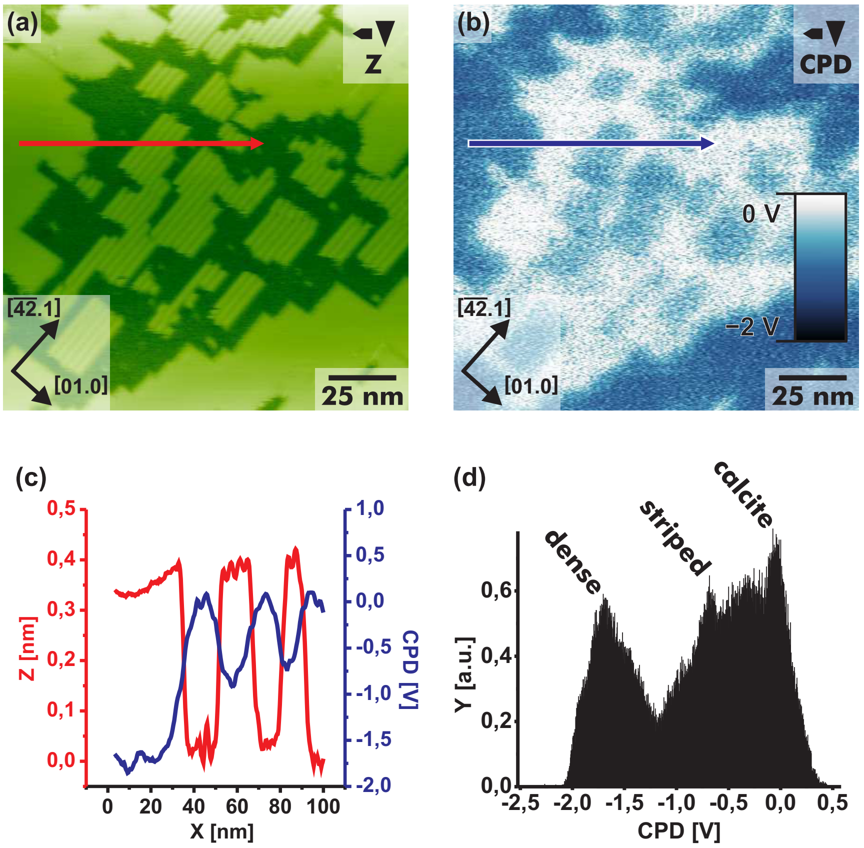

Figure 7.4: Kelvin probe force microscopy information: (a) Topography image revealing the coexistence of the striped and the dense phase. (b) Corresponding KPFM image with the bare calcite surface set to 0 V. (c) Height profile (red) and voltage profile (blue) from the indicated positions in Figs. (a) and (b). (d) Tip voltage histogram from Fig. (b), unraveling a peak at 0 V (substrate), −0.75 V (striped phase) and −1.75 V (dense phase).

local contact potential difference relative to the bare substrate is given in Fig. 7.4(b) with darker regions corresponding to negative voltages.

Note that all data presented herein show the voltage applied to the tip. Compared to the bare surface, the Kelvin signal of the striped phase is shifted towards negative voltages. This is evident from the height and voltage profiles given in Fig. 7.4(c) and quantified in the voltage histogram shown in Fig. 7.4(d). According to this histogram, the voltage measured above the striped phase is approximately −0.75 V. This shift might be explained by a slight electron transfer from the surface to the DHBA molecules, which would result in a slight negative charge of the molecules. In order to compensate the resulting electrostatic forces, a more negative voltage has to be applied to the tip.

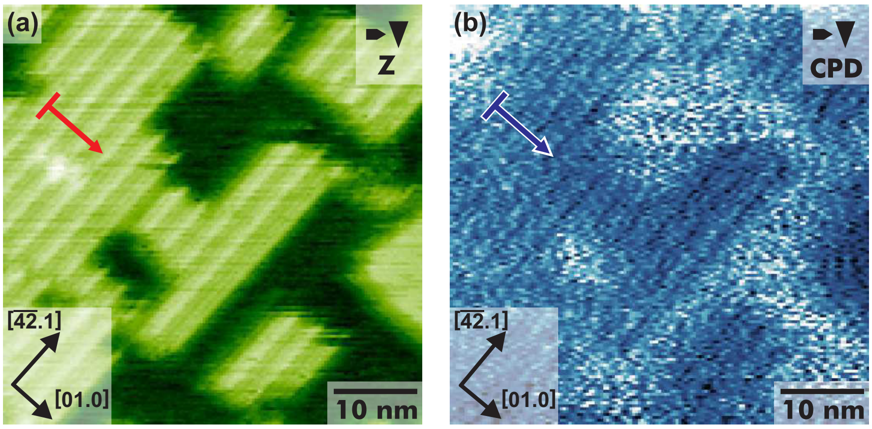

Figure 7.5: High-resolution KPFM image of the striped phase: (a) NC-AFM topography image showing a part of the striped phase. (b) The corresponding KPFM image.

Moreover, due to the intramolecular charge distribution, an internal structure within the striped phase might be resolved when imaging with a very sharp tip. Indeed, in rare cases, the KPFM signal revealed an internal structure within the striped phase as shown in Fig. 7.5. As can be seen from the comparison of the topography (Fig. 7.5(a)) and KPFM (Fig. 7.5(b)) images and the corresponding line scans (Fig. 7.6), a protruding feature in the height profile is associated with a negative shift of the KPFM signal.

Additionally, a further small dip in the KPFM signal is seen in the minimum of the height profile. These characteristics can be explained by considering the molecular packing within the bulk-like phase, as illustrated in Fig. 7.6. Both, in the lying-down and standing-upright phase, the negative parts of the molecules are facing each other, leading to an accumulation of negative charges in the center of the structures. This is indeed reflected in the KPFM line profile in Fig. 7.6.

The different magnitude of the negative shift can be understood by considering the different packing density within the standing-upright and lying-down parts. As the molecular packing is twice as large in the standing-upright part compared to the lying-down part, I expect a more pronounced signal in the protruding part in excellent agreement with the experimental observation.

Relative to the striped phase, the Kelvin signal of the dense phase is further shifted towards more negative values. As can

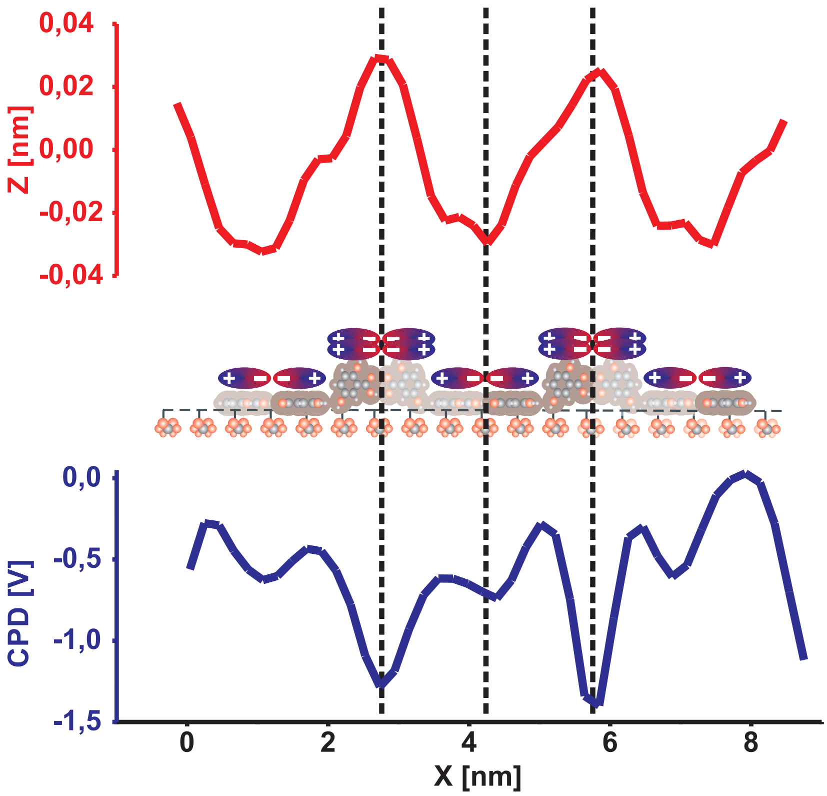

Figure 7.6: Height profile (red) and KPFM profile (blue) taken along the indicated lines in Fig. 7.5(a) and (b). The profiles are averaged over 10 pixel as illustrated by the perpendicular line at the beginning of the height profile lines in Fig. 7.5(a) and (b). The model illustrates the partial charge distribution due to molecular packing.

be seen from the voltage histogram in Fig. 7.4(d), the voltage applied to the tip amounts to approximately $-1.75\,\mathrm{V}$ above the dense phase. This further shift can be readily assigned to the change in charge upon molecule deprotonation. After deprotonation, the molecules are negatively charged.

In order to compensate for the electrostatic force acting between the molecules and the tip originating from this negative charge, a negative voltage has to be applied to the tip. This is directly expressed in the further shift towards more negative voltages above the dense phase compared to the striped phase. As the deprotonation of DHBA on calcite constitutes an acid-base reaction, I expect the proton to be linked to a surface carbonate group, forming hydrogencarbonate.

Thus, in the deprotonated case, a dipole moment pointing towards the surface is formed by the negatively charged molecule and the proton. Since entire instead of partial charges are present in the deprotonated case, a more pronounce signal is evident for the deprotonated compared to the protonated islands. Therefore, the KPFM results directly confirm the above made assignment of the striped and dense phase being formed from the protonated and deprotonated species, respectively.

Summary and Conclusions

In conclusion, I present direct evidence for molecule deprotonation on an insulating surface by KPFM measurements. My high-resolution NC-AFM images elucidate the transient striped phase of DHBA on $CaCO_3(10.4)$ being a bulk-like (6×1) phase, which transforms with time into a dense (1×5) superstructure that is formed by upright-standing molecules. This latter phase can be readily explained by a deprotonation step, as negatively charged molecules anchor with the carboxylate group towards a surface calcium cation. The deprotonation step is directly visualized using KPFM, providing clear-cut confirmation of the above-made assignment.

8 Controlled Activation of Substrate Templating

Contents

As the next step, I demonstrate the activation of substrate templating in molecular self-assembly on a bulk insulator at room temperature by controlled deprotonation. Upon deposition of 4-iodobenzoic acid (IBA) onto the natural cleavage plane of calcite held at room temperature, high molecular mobility is observed, indicating the weak molecule-surface interaction. Molecular islands only nucleate at step edges. These islands resemble the molecular bulk crystal and show no commensurability with the underlying substrate, clearly indicating the absence of surface templating. Upon annealing the substrate, the molecules undergo a transition from the protonated to the deprotonated state. In the deprotonated state, the molecules adopt a well-defined adsorption position, resulting in a distinctly different, substrate-templated molecular structure. My work, thus, demonstrates the controlled activation of substrate templating in molecular self-assembly on a bulk insulator at room temperature.

Introduction

Molecular self-assembly at surfaces benefits from the templating effect of the underlying substrate which greatly enriches the structural variety by controlling the balance between intermolecular and molecule-surface interactions [143]. Thus, to transfer the full potential of molecule self-assembly to insulating substrates, strategies to induce substrate templating have to be explored. An interesting situation is obtained in the case of biphenyl-4,4'-dicarboxylic acid on $CaCO_3$(10.4), which shows the coexistence of two distinctly different molecular structures (Chap. 6).

When anchoring carboxylic acid moieties onto the (10.4) surface of calcite, the charge state of the acid group plays a crucial role: In the protonated state, the molecules can form intermolecular hydrogen bonds as well as hydrogen bonds towards the calcite carbonate group. In the deprotonated state, on the other hand, the negatively charged carboxylate group anchors towards the surface calcium cations (Chap. 7). Carboxylic acids with a low pK_a value deprotonate already at room temperature while carboxylic acids with a pK_a value larger than ≈ 3 stay intact on calcite.

Figure 8.1: Model of the 4-iodobenzoic acid (IBA) molecule.

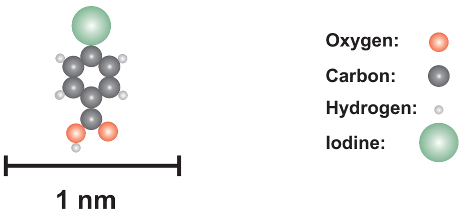

Here, I benefit from the distinct change in molecule-surface interaction by controlled deprotonation of IBA. When deposited onto calcite held at room temperature, intermolecular interactions clearly dominate over the molecule-surface interaction, resulting in the formation of an ordered structure that exhibits no epitaxial or rotational relationship to the underlying calcite lattice. Interestingly, substrate templating can be activated when annealing the substrate. Upon annealing, two different molecular phases coexist that are both governed by the molecule-surface interaction. This work illustrate that substrate templating can be activated deliberately by inducing deprotonation.

IBA Held at Room Temperature

Upon deposition of IBA onto calcite(10.4) (see Fig. 8.2) held at room temperature, large areas of the surface are found to remain unchanged except for a somewhat higher defect density. Molecules are exclusively found in troughs formed by step edges, nucleating into extended, highly ordered islands with an apparent height of approximately 0.5 nm. NC-AFM images of such islands are given in Fig. 8.2, showing straight step edges running from the upper to the lower part of the images. The troughs formed by the step edges are filled by molecular islands (bright area). The existence of extended islands readily indicates that individual molecules are mobile on calcite held at room temperature.

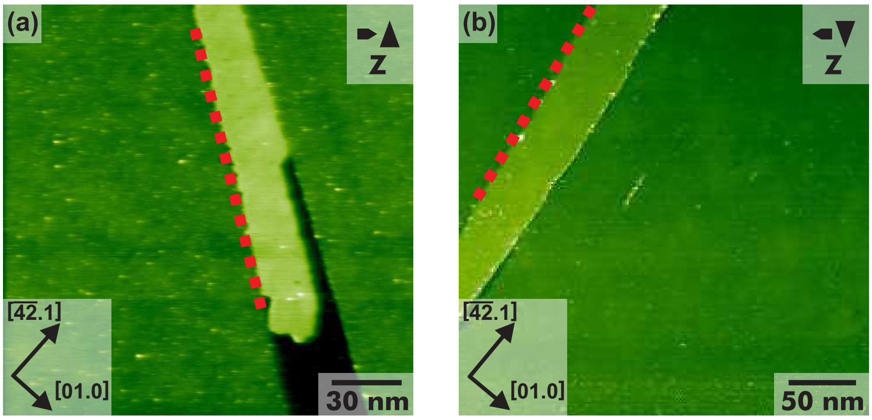

Figure 8.2: Molecular arrangement of IBA after deposition onto the natural cleavage plane of calcite held at room temperature. Overview NC-AFM images, revealing a surface that is largely free of molecules. Only within surface troughs formed by two step edges (in each case one marked by a red dotted line), the molecular islands exist.

A zoom into the molecular islands is given in the drift-corrected images shown in Fig. 8.3(a) and (b). In these images, the molecular structure imaged on two different islands is displayed. The molecules self-assemble into a nearly hexagonal structure with only few lattice defects. Interestingly, the molecular pattern lacks epitaxial and rotational relationship to the underlying calcite crystal, but the molecules seem to arrange along the step edge as demonstrated in Fig. 8.3(a) and (b) by the red dotted lines. Moreover, the overlayer lattice periodicity of 17.2 nm is incommensurate with the calcite lattice along the respective directions.

These findings clearly indicate that the molecular layer is largely unperturbed by the calcite lattice. Instead, the intermolecular interaction is expected to govern this structure. A possible arrangement of the molecules is superimposed in Fig. 8.3(a) and (b). This model is inspired by the common dimerization motif of carboxylic acids within the bulk crystal. The model is reproduced in Fig. 8.3(c). Due to the repulsive interaction between the iodine atoms, one of the two iodines might protrude out of the layer as illustrated in the side view in Fig. 8.3(d). The protruding iodine atoms might be responsible for the bright features seen in the NC-AFM images (see red circles marked in Fig. 8.3(c)).

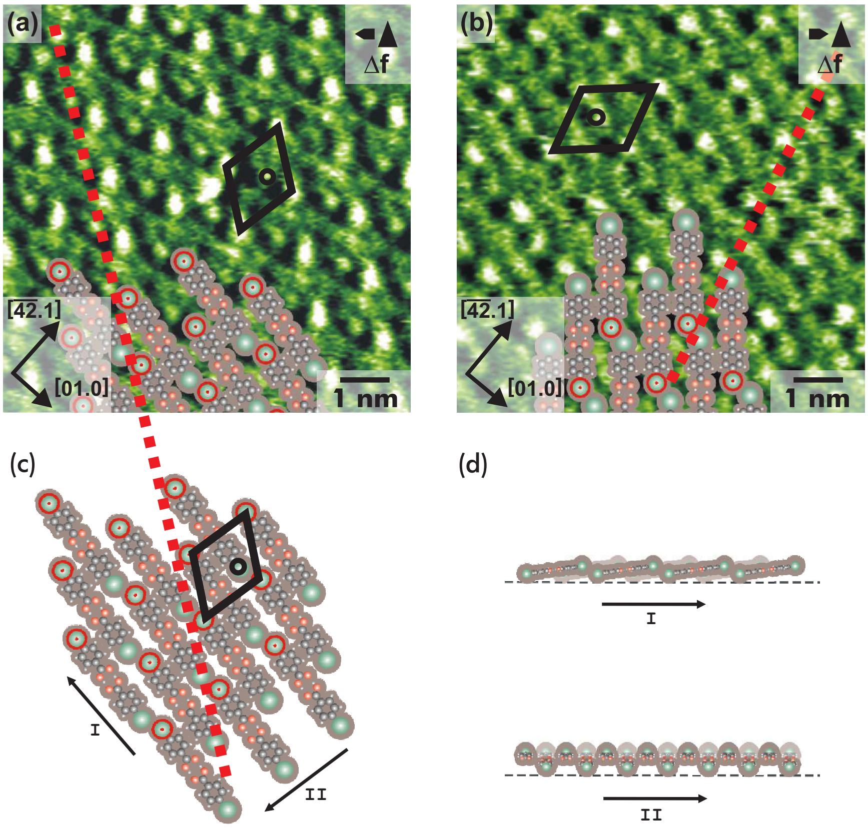

Figure 8.3: Molecular structures in detail. (a) and (b) High-resolution images taken on two different islands shown in Fig. 8.2, illustrating the same internal order which lacks fixed rotational relationship to the underlying substrate lattice. However, Islands arranges along the step edges (red dotted lines). (c) Structural model for the alignment within the island of (a). Protruding iodine atoms are indicated by a red circle. (d) Side views of the island structure along the I and II directions.

After Annealing the Sample

When annealing the calcite substrate to 495 K, the molecular structure changes significantly. Based on my previous findings, I ascribe this structural change to a deprotonation step, which requires annealing in case of IBA having a pK_a value of 4.02 [66]. After annealing, the entire surface is covered by two striped structures (referred to as A and B) with an apparent height of approximately 0.8 nm (Fig. 8.4a). The increased apparent height suggests that the molecules now arrange in a more upright fashion as compared to the room-temperature islands.

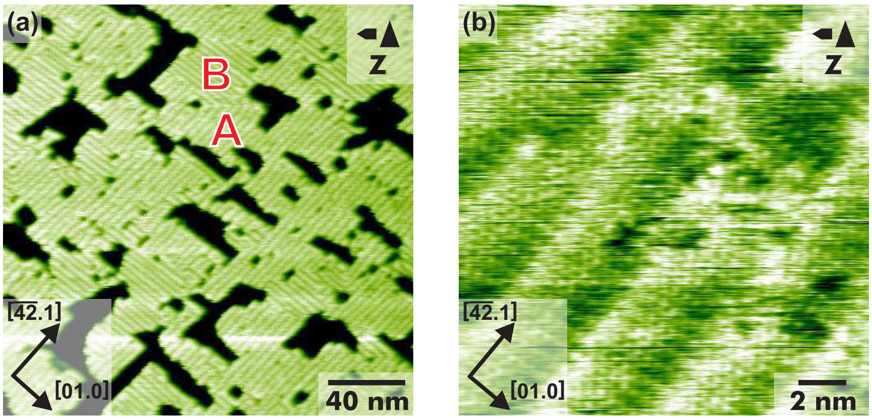

Figure 8.4: Islands structures after annealing the substrate to 495 K. (a) Overview NC-AFM image revealing two striped phases named A and B. (b) Zoom into the A phase, indicating that the stripes originate from a moiré pattern.

In the A phase, the stripes are oriented along the $[\overline{42}.1]$ direction, while in the B phase, the stripes are running along the [01.0] direction. A zoom into the A phase (Fig. 8.4(b)) discloses a dotted pattern, where each dot fits in size with an upright-standing molecule. The zoom in Fig. 8.4(b) indicates that the stripes originate from a moiré pattern. Drift-corrected high-resolution images of the A and B phases are shown in Fig. 8.5(a) and (b), respectively. Phase A is composed of dots with a repeat distance of approximately 0.58 nm in [01.0] direction and 0.79 nm in $[\overline{42}.1]$ direction. In $[\overline{42}.1]$ direction, the molecules adopt the substrate periodicity of 0.81 nm. Along the [01.0] direction, however, seven molecules are spaced atop eight calcite repeat distances, resulting in a (8 × 1) superstructure ($7 \cdot 0.58$ nm = 4.06 nm equals to $8 \cdot 0.50$ nm = 4.00 nm).

The difference in lattice spacing along the [01.0] direction readily explains a moiré pattern with stripes running perpendicular to the [01.0] direction as evident in Fig. 8.4(a). Phase B is formed by dots with a periodicity of approximately 1.01 nm along the [01.0] direction, which equals two times the calcite unit cell dimension in this direction. Along the $[\overline{42}.1]$ direction, however, the molecular pattern shows a distance of approximately 0.57 nm, which is different from the substrate periodicity. Along this direction, seven molecules are spaced along five calcite unit cell repeat distances ($7 \cdot 0.57\,\text{nm} = 3.99\,\text{nm}$ equals to $5 \cdot 0.81\,\text{nm} = 4.05\,\text{nm}$), resulting in a ($2 \times 5$) superstructure (Fig. 8.5(c)). Again, the different periodicity of the substrate and the molecular pattern gives rise to a moiré pattern, which is perpendicular to the $[\overline{42}.1]$ direction for phase B.

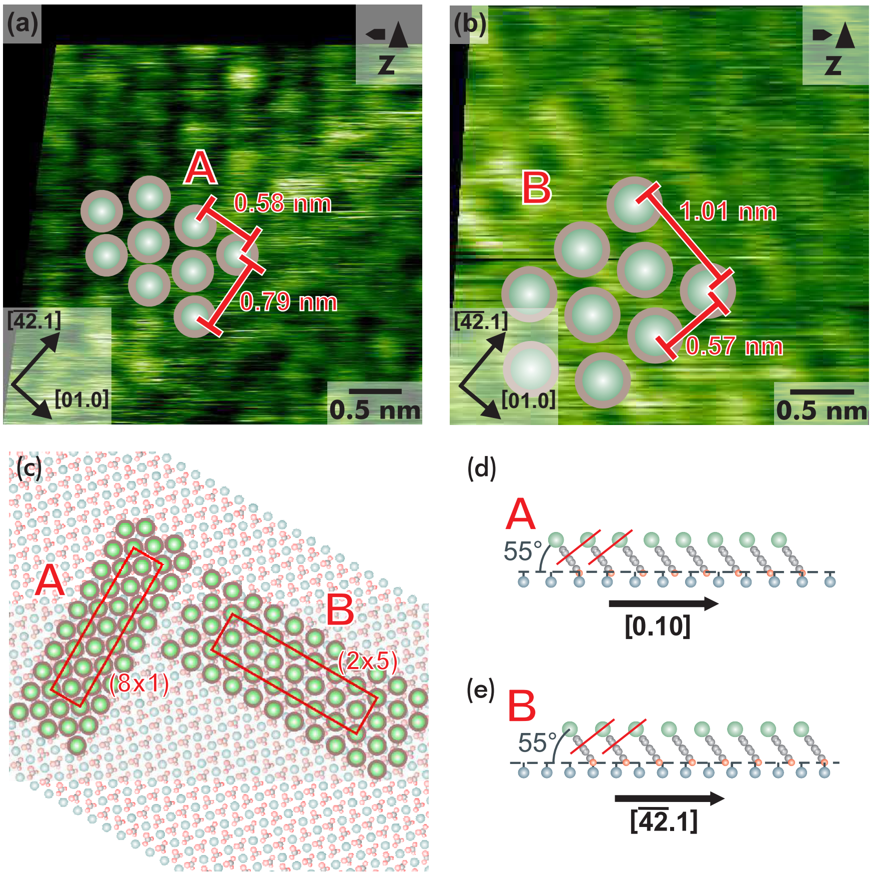

Figure 8.5: Drift-corrected high-resolution NC-AFM images. (a) The A phase, showing a (8×1) superstructure. (b) Image of the B phase, showing a centred (2×5) superstructure. (c) Model illustrating the arrangement of the molecules within the two structures. (d) Side view along the [01.0] direction of the A phase, illustrating the resulting alignment of the iodine atoms and the aromatic rings. The optimum molecular packing results in a moiré pattern with seven molecules arranged along a distance of eight lattice repeat units. (e) Corresponding view of the B phase along the $[\overline{42}.1]$ direction.

The existence of the moiré pattern clearly indicates that the molecular structures are steered by the underlying substrate in one direction ($[\overline{42}.1]$ direction for phase A, [01.0] direction for phase B), while the distance in the other direction is influenced by the intermolecular interaction. Interestingly, the spacing of phase A along the $[01.0]$ direction is similar to the spacing of phase B along the $[\overline{42}.1]$ direction, suggesting that this spacing is dominated by the intermolecular interaction.

This can be understood by considering a tilted arrangement of the molecules as given in Fig. 8.5(d) and (e), in which the iodine atoms are placed above the center of the aromatic ring of the neighboring molecule. This configuration is in accordance with upright standing deprotonated molecules anchoring towards the surface with the negatively charged carboxylate groups that bind to the surface calcium cations. Thus, by deprotonating the molecules, the molecule-surface interaction is greatly increased and substrate-templated structures emerge.

Summary and Conclusions

In conclusion, the controlled activation of substrate templating is demonstrated by inducing a deprotonation reaction of IBA on the natural cleavage plane of calcite. When depositing IBA onto calcite held at room temperature, the molecules are found to be highly mobile on the surface. The molecules exclusively nucleate at step edges and arrange themselves into an ordered array that follows an important motif of the bulk structure, namely hydrogen bond formation between the carboxylic acid groups. The latter finding gives strong evidence for the fact that the molecules remain protonated in this structure. Most interestingly, these islands lack an epitaxial or rotational relationship to the underlying calcite lattice, clearly demonstrating the absence of substrate templating. This situation is changed reproducibly upon annealing the substrate to 495 K, which results in molecule deprotonation. After deprotonation, two different phases are formed that are distinctly different from the former hydrogen-bonded structure. Now, the molecules stand upright on the surface, with the negatively charged carboxylate groups anchoring towards the surface calcium cations. This substrate templating effect is clearly reflected in the molecular ordering that now follows the substrate periodicity in one direction ($[\overline{42}.1]$ direction for phase A and $[01.0]$ direction for B, respectively). Perpendicular to this direction, a moiré pattern is observed, which is governed by the optimum packing of the aromatic rings. This study demonstrates that molecular deprotonation can be successfully exploited to deliberately activate substrate templating in molecular self-assembly.

9 On-Surface Covalent Linking

Contents

In this Chapter, I demonstrate the covalent linking of organic molecules on the bulk insulator calcite. I deliberately employ the strong electrostatic interaction between the carboxylate groups of halide substituted benzoic acids and the surface calcium cations to prevent molecular desorption and to reach homolytic cleavage temperatures. This allows for the formation of aryl radicals and intermolecular coupling. By varying number and position of the halide substitution, I rationally design the resulting structures, revealing straight lines, zig-zag structures as well as dimers, thus providing clear evidence for the covalent linking.

Introduction

Upon tuning the subtle balance between intermolecular and molecule-surface interactions (Chap. 6), using of surface active molecule end groups [72] and utilization of deprotonation to activate templating (Chap. 8), stable molecular structures have been constructed in clean and well-controlled UHV conditions. When having molecular electronics applications in mind, the weak and reversible interactions pose a further challenge as they hardly provide sufficient intermolecular electron transport capabilities. Only recently, the concept of on-surface synthesis [8] has been exploited as a promising strategy to overcome these limitations. But, so far, on-surface synthesis has been limited to metallic substrates (Chap. 5). Moreover, thermal activation of a coupling reaction is not feasible on many insulating surface, like alkali halides, as most organic molecules would desorb at temperatures below the reaction temperature. Therefore, it appears necessary to use a controllable anchoring mechanism for the molecules, such as the deprotonation, as shown in Chap. 8.

Herein, I present the covalent coupling of four different halide substituted benzoic acids (for an overview see Fig. 9.1), namely 2,5-diiodo benzoic acid (DIBA), 2,5-dichloro benzoic acid (DCBA), 3,5-diiodo salicylic acid (DISA) and 4-iodo benzoic acid (IBA) on calcite. The carboxylic acid moiety is known to bind strongly towards the calcite surface [144], thus, compared to other insulating surfaces, the carboxylic acid-calcite system has revealed very promising results in terms of substrate-templated molecular self-assembly [64; 73].

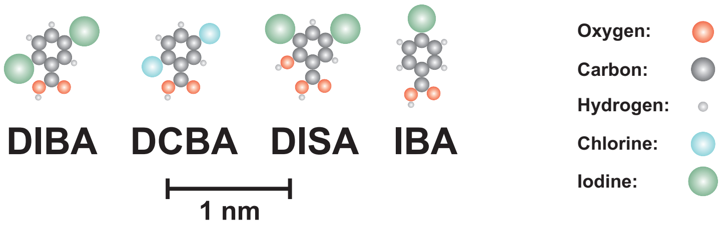

Figure 9.1: Models of the used organic molecules comprising 2,5-diiodo benzoic acid (DIBA), 2,5-dichloro benzoic acid (DCBA), 3,5-diiodo salicylic acid (DISA) and 4-iodo benzoic acid (IBA).

Here, the comparatively high molecule-substrate binding strength is employed to prevent clustering at step edges and to avoid desorption upon thermal activation of the coupling reaction. The previous results in Chap. 7 and 8 indicate that the carboxylic acid group deprotonates before covalent linking. The presence of the carboxylate group being a strong electron donor is expected to weaken the phenyl-halide bond and, therefore, favor homolytic cleavage of this bond to give reactive phenyl radicals at moderate temperatures without the need of a coupling catalyst.

Upon deposition at room temperature, DIBA and DCBA form extended and highly ordered monolayers, which undergo a clear transition into straight molecular wires upon thermal activation, as unraveled by NC-AFM. The observed structures fit excellently in size with a model of a covalently bound, completely conjugated molecular row. When changing the position of the halide substitution from 2,5 to 3,5 as in 3,5-diiodo salicylic acid (DISA), again a distinct structural transition can be observed upon thermal activation, however, in this case zig-zag instead of straight structures are revealed. Finally, when having only one halide atom per molecule, dimers instead of extended rows are expected to form upon covalent linking. Indeed, thermal activation of IBA results in the formation of dimer-like molecular structures that fit in size to the expected reaction product, 4,4'-biphenyl dicarboxylic acid (BPDCA).

Deposition of DIBA

First, a sub-monolayer coverage of DIBA is deposited onto a freshly cleaved calcite (10.4) surface held at room temperature. After deposition, the resulting structure is observed by NC-AFM. An overview image is shown in Fig. 9.2(a), revealing two calcite terraces that are covered by molecular islands with an apparent height of approximately 0.7 nm. From this image it can be concluded that individual DIBA molecules are mobile and diffuse on the surface to form extended stable monolayers.

A zoom into one island exhibits a highly ordered structure with bright rows running along the $[\overline{42}.1]$ direction as shown in the drift-corrected image presented in Fig. 9.2(b). The dimensions of the unit cell measure 2.53 nm × 0.81 nm, constituting a (5 × 1)

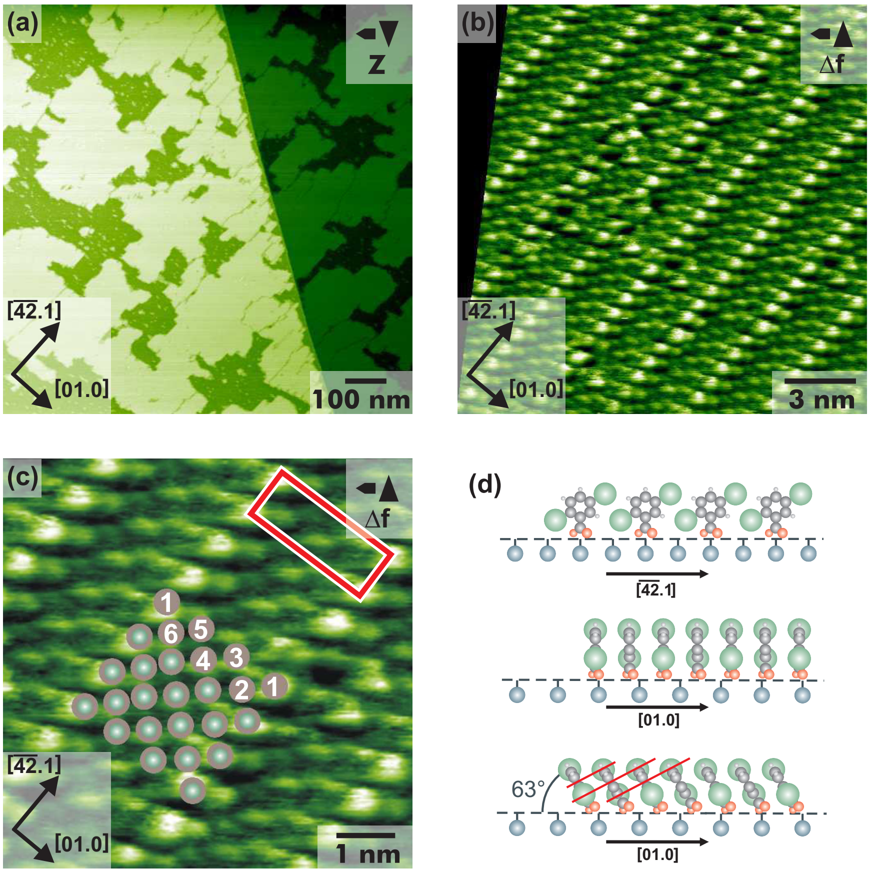

Figure 9.2: As-deposited structure of DIBA. (a) Overview NC-AFM image of DIBA, showing two calcite terraces covered by 0.7 nm high islands. (b) Drift-corrected detail NC-AFM image of a DIBA island. (c) Zoom into the ordered structure with a (5 × 1) unit cell. (d) Model explaining the molecular structure.

superstructure as superimposed in Fig. 9.2(c). Along the [$\overline{42}$.1] direction, the distance between two molecules is 0.81 nm, corresponding to a commensurate molecular structure. A model is shown in Fig. 9.2(d, upper panel). Molecular dynamics calculations [144] suggest that molecules containing a carboxylic acid moiety anchor to the calcite surface with the carboxylic group binding to a surface oxygen and calcium atom in an upright fashion.

However, the binding is of course greatly influenced by the protonation or deprotonation state of the acid. In Chap. 7 and 8 the deprotonation step is shown for different pK_a values. The tendency of the benzoic acids derivates to deprotonate on the calcite surface follows the trend, that molecules with a pK_a value larger than ≈3 stay intact on calcite while molecules with a lower pK_a value deprotonate already at room temperature. For DIBA, having a calculated pK_a of 2.51 (i.e., in vacuo), the results indicate that DIBA molecules are already deprotonated at room temperature. I note that the listed pK_a values must not been taken too literally, as adsorption onto the surface might have a significant influence. However, the general trend in acidity should be reflected correctly by considering the calculated (in vacuo) values.

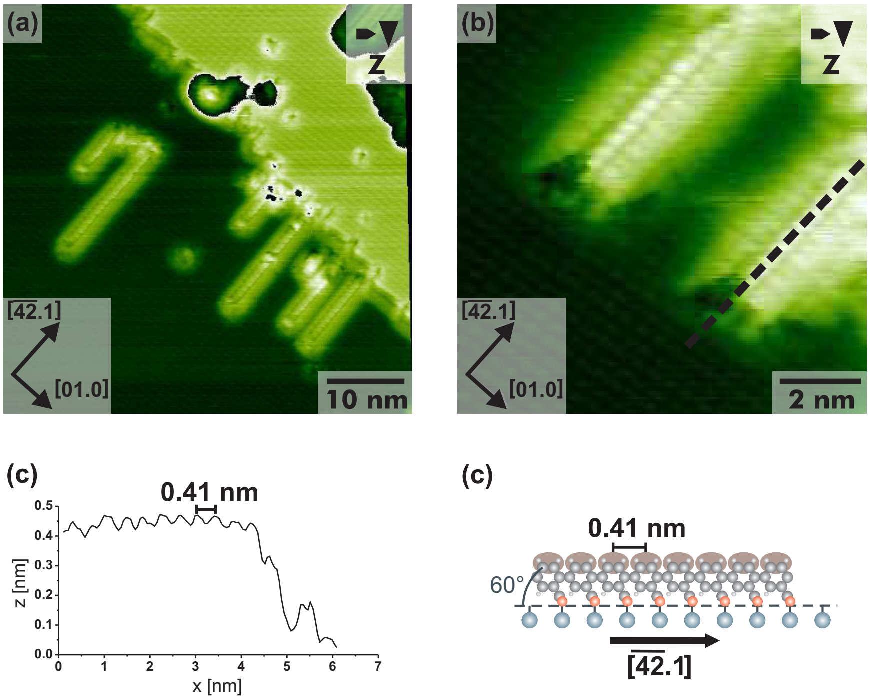

Figure 9.3: Covalent linking of DIBA.
(a) NC-AFM image of DIBA after annealing above 530 K (here: 555 K). The structures decorate step edges and rows are observed growing along the [$\overline{42}$.1] direction. (b) Detail NC-AFM image, showing two molecular rows and the substrate with atomic resolution. (c) Height profile as indicated in (b), revealing a repeat distance of 0.41 nm, in excellent agreement with a reacted molecular chain. (d) Model explaining the reacted structure.

Thus, in the case of DIBA I expect the negatively charged carboxylate group to anchor to the calcium ions. The iodine atoms are oriented away from the surface. Along the [01.0] direction, the structure is not commensurate, but coincident, as six molecules (marked by numbers) are situated in a zig-zag fashion along a distance of 2.53 nm (see superimposed model in Fig. 9.2(c)), corresponding to five lattice repeat units. This fact explains the overall modulation of the brightness, which is due to a moiré effect (model shown in Fig. 9.2(d, middle panel)).

In this configuration, the spacing of the molecules along the [01.0] direction is 0.42 nm, which is too large to account for a considerable intermolecular interaction, raising the question as to why the molecules would arrange in this way. This question can be readily answered by considering a tilt angle, which decreases the distance between the benzene rings and the iodine atoms. When considering a tilt angle of around 63°, the iodine atoms are positioned in the centre of a benzene ring with a distance of 0.37 nm to the ring centre (Fig. 9.2(d, lower panel). This would constitute a strong driving force for a tilt, which should result in a reduction of the apparent height. The total height of the molecule is in the order of 0.8 nm; however, when introducing a tilt angle of 63°, this height is reduced to 0.71 nm, which fits to the measured height of 0.7 nm.

Covalent Linking of DIBA and DCBA

When annealing the DIBA sample to a temperature above 530 K, a completely different situation is present as shown in Fig. 9.3(a). Now, in contrast to what was observed before at room temperature, no extended islands are formed, but rows running along the $[\overline{42}.1]$ direction. The rows shown in Fig. 9.3(a) decorate the step edges (one step edge is running from the lower left to the upper right part of the image). This drastic change in molecular structure is explained by thermolytic dissociation of the two iodine atoms from the molecule and subsequent covalent linking of the radical molecules. As the iodine atoms are substituted at the 2 and 5 positions, i.e. at opposite positions, a straight row is expected upon covalent linking.

A detailed view given in the drift-corrected image in Fig. 9.3(b) reveals a highly ordered structure that fits in size with molecules forming a row after iodine dissociation and reaction of radicals. From a height profile taken at a line indicated in Fig. 9.3(b), a repeat distance of 0.41 nm is revealed (Fig. 9.3(c)). This distance is in excellent agreement with a model of a reacted, completely conjugated chain as shown in Fig. 9.3(d).

In this model, the molecule is again anchored towards the surface with the carboxylate groups as discussed before. In order to allow for covalent bond formation at the previous iodine positions, the molecules have to tilt at an angle of approximately 60° between the main molecular axis and the surface. This tilt results in a calculated reduction of the apparent height from nominally 0.75 nm for the iodine-free molecules to 0.65 nm. Experimentally, I reveal an apparent height of 0.45 nm, which is somewhat smaller than the expected value. However, I need to stress that different interaction forces greatly influence height measurements in NC-AFM, readily explaining this height difference.

The same reaction pathway is expected for DCBA, where the iodine atoms are replaced by chlorine atoms. DCBA has basically the same pK$_a$ value of 2.50, but a higher carbon-halide bond strength (Cl-C_6H_5: 400 kJ/mol versus I-C_6H_5: 272 kJ/mol) [157]. Based on the binding energies alone, very high thermolytic cleavage temperatures would be expected. Interestingly, in a recent study, thermolytic cleavage of bromine has been achieved at 590 K within a the molecule sublimator (i.e., in the absence of a metallic surface) [93].

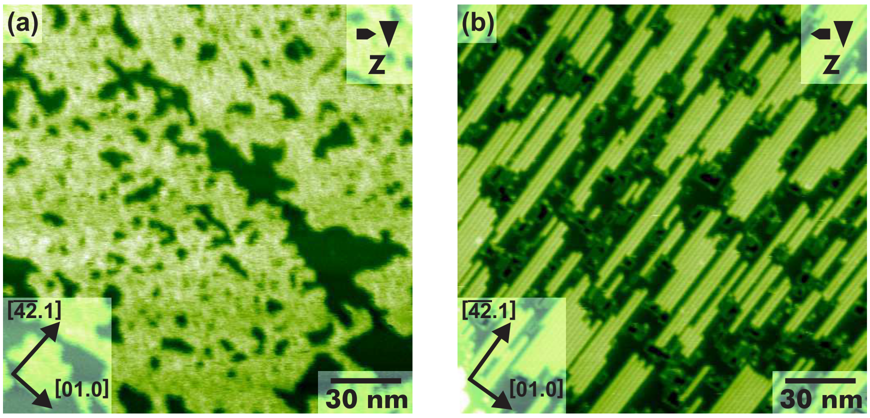

Figure 9.4: Covalent linking of DCBA. (a) Overview NC-AFM image of DCBA deposited onto the calcite surface held at room temperature, showing 0.7 nm high islands. (b) NC-AFM image of DIBA after annealing above 565 K showing molecular rows in a high coverage.

In this case, as mentioned above, the carboxylate formation and the interaction with the surface is expected to facilitate the homolytic cleavage. Thus, exclusively considering the bond strengths certainly oversimplifies the situation. I do, however, expect that somewhat higher temperatures are required when repeating the same experiments with DCBA instead of DIBA.

I have done this experiment (Fig. 9.4) and, indeed, find the same structures, but at an increased transition temperature which has to be raised above 565 K for inducing covalent linking, approving the above made conclusion. After annealing, I observe an increased defect density in the case of both, DIBA and DCBA. These defects might arise from the dissociated iodine and chlorine atoms, respectively. However, I speculate that most of the dissociated iodine and chlorine atoms desorb upon annealing.

Changing the Substitution Position

Next, I have changed the substitution position from 2,5 to 3,5 with the objective to create a zig-zag structure after covalent linking. As 3,5-diiodo benzoic acid was not available for this study, 3,5-diiodo salicylic acid (DISA) is used instead, having a pK_a of 2.07. This low pK_a value suggests the molecules to be already deprotonated at room temperature.

The as-deposited structure is shown in Fig. 9.5(a), revealing a commensurate (1×1) superstructure with an apparent height of 0.6 nm, which agrees with upright standing molecules. Annealing this sample to 580 K again results in a distinctly different molecular pattern, as shown in Fig. 9.5(b). In this image, molecular features of differing shape are observed. The apparent height of these structures is in the order of 0.35 nm, suggesting flat-lying molecules in this case. Among them, zig-zag structures are, indeed, obtained as marked by a rectangle in the centre of the image.

An enlarged view is given in Fig. 9.5(c) along with a model of covalently linked poly(metaphenyl) molecules forming a zig-zag row. The observed transition from standing molecules at room temperature to lying molecular structures upon annealing can be readily understood by considering the position of the carboxylate groups. In the case of individual DISA molecules, all molecules can arrange with the carboxylate groups pointing towards the calcite surface, resulting in a layer of upright-standing molecules. After reaction, however, the carboxylate groups point in opposite directions, which prevents concerted binding of these groups to the surface, explaining the transition from standing to flat-lying molecules.

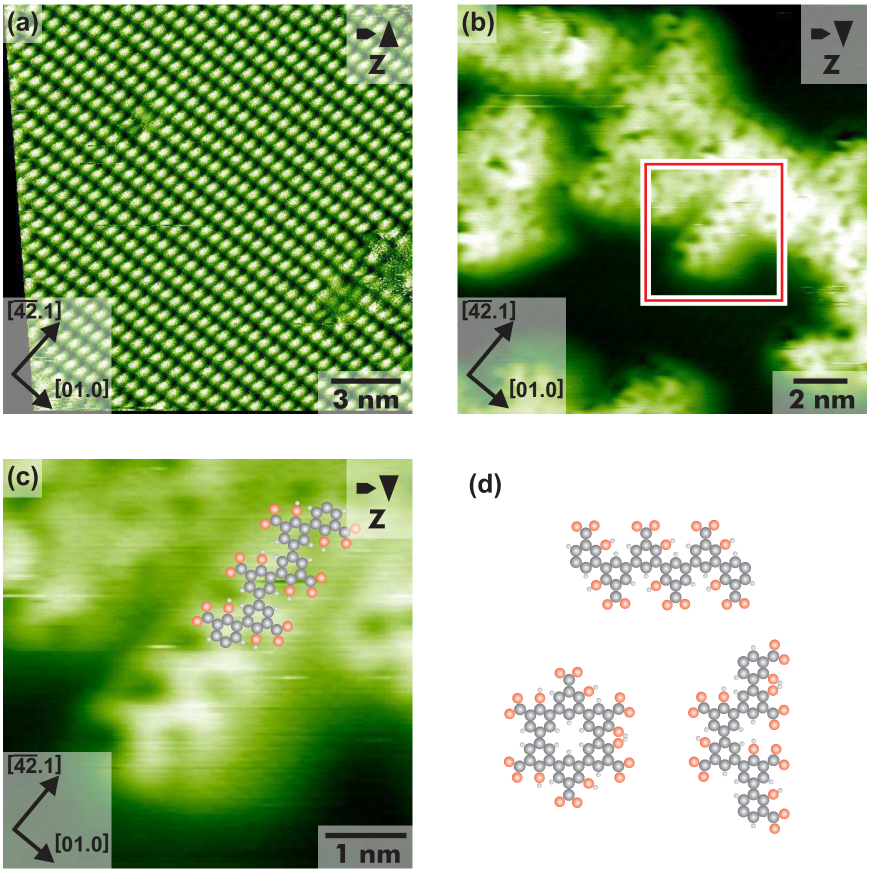

Figure 9.5: Covalent linking of DISA. (a) NC-AFM image of DISA deposited onto the calcite surface held at room temperature, revealing a commensurate (1×1) structure. (b) Detail NC-AFM image of the sample after annealing to 580 K, revealing a distinctly different molecular structure. A zig-zag pattern is obtained as marked by a rectangle. (c) Zoom into the marked area in (b) with a superimposed model of the covalently linked molecules. (d) Model of the different structures possible upon covalent linking. Besides a zig-zag row, also other, kinked and circular patterns are possible.

Besides zig-zag structures, DISA can form other patterns, which occur when the molecules link with a different angle as illustrated in Fig. 9.5(d). This fact readily explains the less ordered appearance of DISA upon annealing as compare to the structures observed after annealing of DIBA, as only straight lines are possible in the latter case. The structural change from straight lines as observed for 2,5 substituted DIBA and DCBA to aggregates with a kinked linking in the case of 3,5 substituted DISA constitutes a further strong confirmation of the above-drawn conclusion of covalent linking.

Reducing the Number of Substitutions

As a further evidence for the coupling reaction, I next discuss reducing the number of halide atoms at the phenyl ring from two to one. Molecules with only one halide atom are expected to form dimers instead of extended wires upon covalent linking.

To follow this approach, IBA with a pK_a of 4.02 is deposited onto freshly cleaved calcite. Due to the comparatively high pK_a value, the molecules remain protonated at room temperature, as is evident from a further structural transition observed upon moderate annealing to 520 K before inducing covalent coupling at higher temperatures as explained in Chap. 8. After the first annealing step, two domains of extended islands are observed with upright-standing molecules (Fig. 9.6(a)). Thus, the molecules are assumed to bind as negatively charged carboxylates.

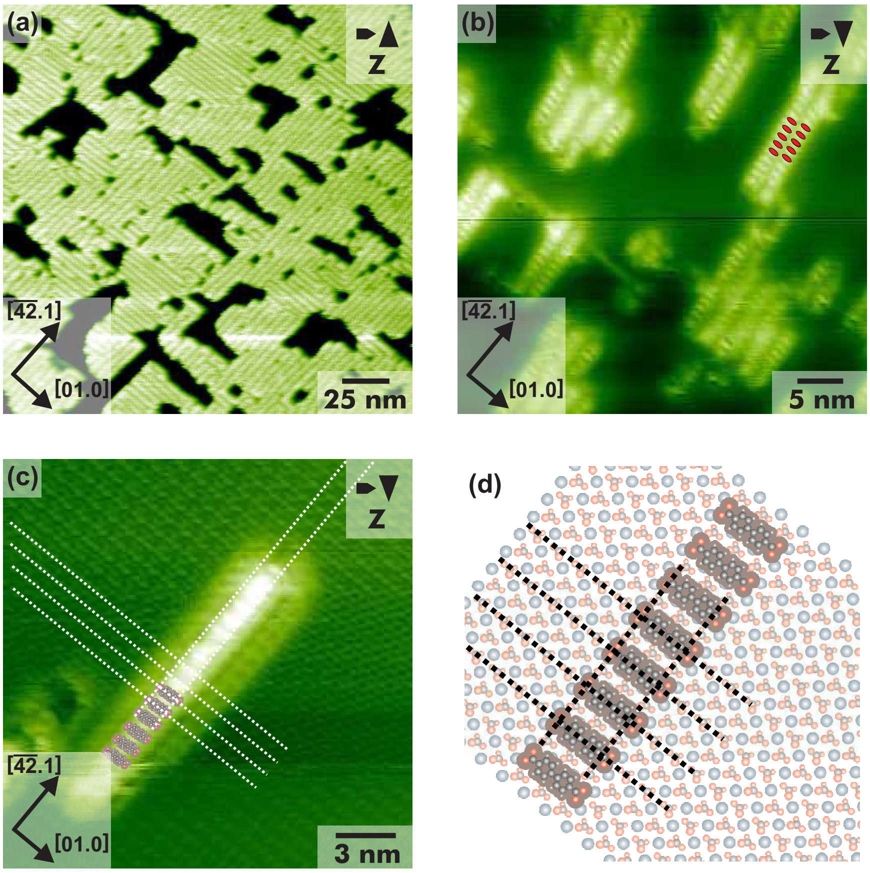

Figure 9.6: Covalent linking of IBA. (a) Annealing of the IBA-covered sample to a temperature of 520 K, two domains are revealed (see Chap. 8). (b) Molecular structure of the IBA-covered substrate after annealing to 580 K showing molecular rows running along the [$\overline{4}$2.1] direction. The rows are composed of individually resolved features that are aligned *side-by-side*. (c) Zoom onto a single molecular row with superimposed BPCDA model molecules. (d) Structural model to (c) showing the flat-lying molecules with the carboxylate groups adsorbed on top of two calcium ions of the substrate.

In an attempt to deiodize the IBA molecules and to induce a covalent linking of the remaining radical molecules to form BPDCA molecules, the molecules are further annealed to thermally activate the deiodization and subsequent linking. Annealing an

IBA-covered calcite surface to 580 K again results in a significant structural change.

As shown in Fig. 9.6(b), now rows are obtained that oriented along the $[\overline{42}.1]$ calcite direction. The apparent height of the rows is 0.4 nm, suggesting flat-lying molecules. The rows are composed of features that fit excellently in size with BPDCA molecules aligned *side-by-side*, as illustrated by the superimposed ellipses with size of BPDCA molecules (Fig. 9.6(b)). Often, two or more rows are observed to align, resulting in double-rows and larger arrangements.

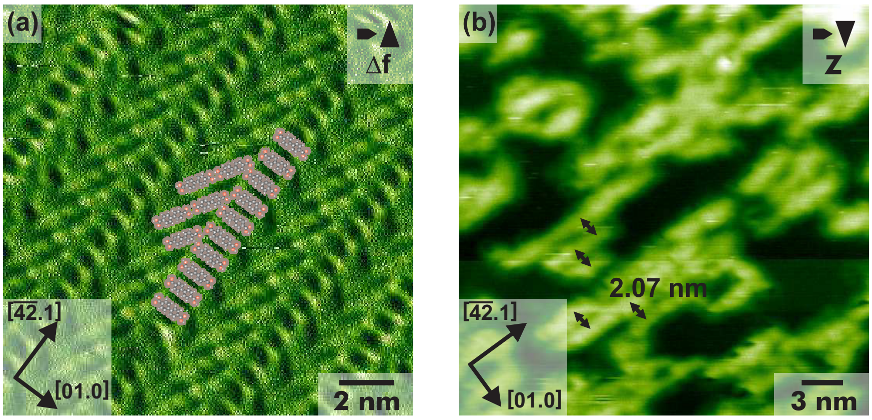

Figure 9.7: (a) NC-AFM image of BPDCA, revealing rows along the $[\overline{42}.1]$ direction (Chap. 6). (b) Situation after annealing to 580 K, resulting in a structural change that is ascribed to deprotonation. Now, individual rows of molecules are observed that fit in orientation and size with the rows observed for reacted IBA.

However, single rows exist as well, as shown in Fig. 9.6(c). Based on these data, which reveal both, the molecular rows and the calcite lattice simultaneously, the molecule adsorption position can be determined unambiguously. The calcite lattice reveals the two pronounced reconstructions, the (2 × 1) reconstruction and the row pairing, allowing for an identification of the lattice sites [53]. The lines drawn along the [01.0] direction in Fig. 9.6(c) are superimposed onto the bright features of the calcite surface, which are ascribed to the protruding oxygen atoms of carbonate groups having the same orientation. The lines in $[\overline{42}.1]$ direction are placed in a way that they superimpose the less bright features, which are known to be the oxygen atoms of the carbonate groups having the opposite orientation within the unit cell. As can be seen, the molecular row is centered in between the lines drawn in $[\overline{42}.1]$ direction. The molecules within the row are centered on the lines superimposed along the [01.0] direction. With this information, a precise structural model can be constructed, as given in Fig. 9.6(d).

In this model, I assume the reacted IBA molecules to be deprotonated, as suggested by the structural change observed upon moderate annealing. The size of a deprotonated BPDCA molecule allows for an excellent alignment of the negatively charged carboxylate groups on top of two calcium ions of the substrate, which is exactly what I obtain from the model. The measured molecular spacing along the $[\overline{42}.1]$ direction of 0.81 nm reflects the spacing of every two calcium ions along this direction. Along the [01.0] direction, the measured spacing of 2.07 nm between adjacent rows again reflects the calcite lattice dimensions (four times 0.51 nm) and, thus, further supports the assumption of a well-defined adsorption position in the case of covalently linked IBA molecules.

I take the excellent agreement in size and the very reasonable spacing with respect to the calcite substrate as strong indications for the reaction of IBA to deprotonated BPDCA. Moreover, the transition in the molecular orientation from standing-upright to lying-down provides further evidence for the covalent linking. After the reaction, the carboxylic groups point in opposite directions, making concerted binding of the carboxylate groups to the calcite impossible. As a consequence, the dimers are expected to lie flat on the surface, which is, indeed, observed. Finally, a direct comparison with BPDCA molecules further reveals the structural similarity of the reacted IBA and as-deposited BPDCA molecules (see Fig. 9.7), serving as a further confirmation of the above drawn conclusion.

Summary and Conclusions

To conclude, I have demonstrated the covalent linking of halide substitute benzoic acid molecules by thermal activation on a bulk insulator, namely the (10.4) cleavage plane of calcite. The resulting products constitute conjugated molecular structures on a truly insulating support, providing electronic decoupling from the substrate, which is mandatory for future applications. By comparison of different substitution position as well as changing the number of halide substituted atoms, I demonstrate the specificity of this approach. These results pave the way for application of on-surface synthesis on bulk insulators.

10 Two-Step On-Surface Polymerization

Contents

By carefully selecting a suitable precursor molecule, I report on a two-step linking reaction on a bulk insulating surface. Besides a firm anchoring towards the substrate surface, the reaction sites and sequential order are encoded in the molecular structure, providing so far unmatched reaction control in on-surface synthesis on an insulating surface.

Introduction

The selective interaction of rationally designed molecular building blocks has been tailored with great success to steer the resulting molecular structure in a well-controlled manner [143; 158]. Covalent linking of molecular precursors on the surface, referred to as on-surface synthesis, has recently emerged as a promising approach for the bottom-up fabrication of functional molecular structures with superior stability and increased electrical conductivity (Chap. 5). A very exciting aspect of on-surface synthesis is the ability to follow new reaction pathways that might not be possible by classical solution synthesis [150].

Up to now, the complexity of these structures has been very limited as most of the reactions have been performed in a single-step manner. Increasing the structural variety of on-surface synthesis requires utmost control with the ability to selectively induce sequential linking reactions in a hierarchical manner. This has recently been demonstrated using halide-substitute porphyrin derivatives on a Au(111) surface [108].

The latter work constitutes an elegant example exploiting the specific dissociation energies of the bromine- phenyl and iodine-phenyl bond. These dissociation energies are associated with different activation temperatures, allowing for inducing the linking reaction in a site-specific and sequential manner. Thus, the reaction sites and sequence are encoded in the molecular structure of the precursors. So far, no example exists, demonstrating hierarchical control in on-surface synthesis on a bulk insulator substrate.

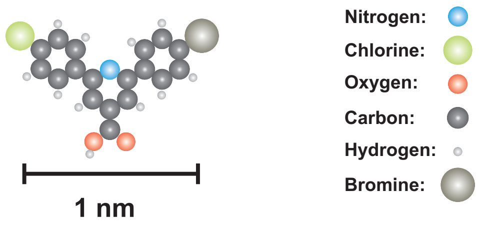

Figure 10.1: Model of a 2-(4-Bromophenyl)-6-(4-chlorophenyl)pyridine-4-carboxylic acid (BPCPPCA) molecule.

Herein, I present the first successful example of improved structural control that is achieved from a site-specific and selective two-step linking process on a bulk insulator surface in UHV. The 2-(4-bromophenyl)-6-(4-chlorophenyl)pyridine-4-carboxylic acid (BPCPPCA, Fig. 10.1) molecule used in this study was selected based on three functional groups.

Bromophenyl and chlorophenyl groups were chosen for inducing site-specific and sequential covalent linking based on homolytic cleavage of the halide-phenyl bonds, having dissociation energies of 336 kJ/mol (Br-C_6H_5) and 399 kJ/mol (Cl-C_6H_5) [157]. The third group is needed to provide sufficient anchoring towards the bulk insulator substrate, the natural cleavage plane of calcite (Chap. 4). A carboxylic acid moiety is known to bind sufficiently to this surface [66], which constitutes an inevitable prerequisite allowing for thermal activation of the desired reactions before the desorption temperature is reached.

When deposited onto the surface at room temperature, ordered islands are obtained as revealed by high-resolution NC-AFM. A first distinct change in molecular structure is induced upon annealing to 570 K, which can be assigned to the homolytic cleavage of the bromine-phenyl bond and subsequent covalent linking of the resulting radicals, resulting in molecular dimers. Further annealing to 610 K induces the subsequent cleavage of the remaining chlorine-phenyl bond. The covalent coupling of the radicals now results in polymerization of the dimers into zig-zag and closed ring structures, which are encoded by the specific design of the molecular building blocks.

This study demonstrates the successful application of a hierarchical two-step linking process on a bulk insulator surface, resulting in enhanced structural control that is programmed by the rational design of the molecular structure.

Depositing BPCPPCA on the $CaCO_3$ Surface

Upon submonolayer deposition of BPCPPCA molecules onto the calcite surface held at room temperature, two types of ordered islands are observed as shown in the NC-AFM images in Fig. 10.2. Overview images of island type A and B are given in Fig.

10.2(a) and (b), respectively. In Fig. 10.2(a), an A-type island is shown in the lower part of the image, while the upper darker area corresponds to the bare calcite surface. The island is composed by two different areas, displayed in darker and brighter color corresponding to an apparent height of 0.5 and 0.8 nm. I ascribe the brighter area to a second layer occupation. Here, I focus on the darker area, which is ascribed to a monolayer of BPCPPCA molecules. Faint lines are visible that are oriented at an angle of +50 ± 3° with respect to the $[\overline{42}.1]$ direction.

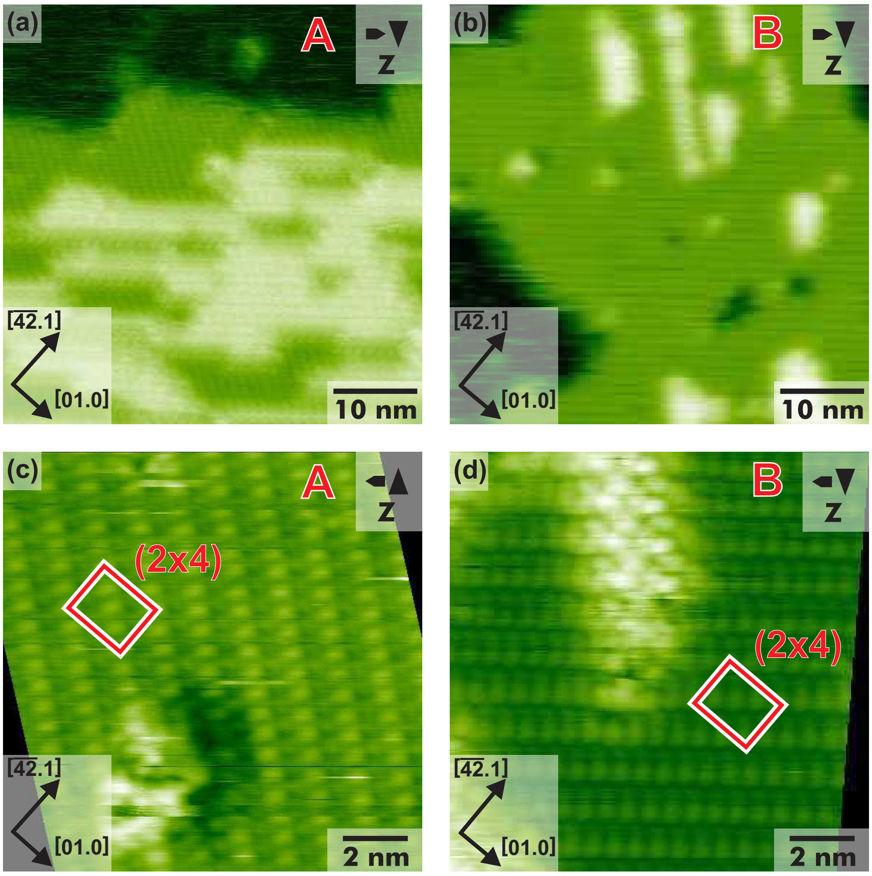

Figure 10.2: Molecular islands after deposition of BPCPPCA onto calcite(10.4). (a) Island type A exhibiting faint lines that are oriented at an angle of +50 ± 3° with respect to the $[\overline{42}.1]$ direction. A second-layer occupation is seen. (b) Island type B with faint lines that are oriented at an angle of −52 ± 3° with respect to the $[\overline{42}.1]$ direction. As in the case of island type A, a second layer occupation is revealed. (c) and (d) drift-corrected high-resolution image of type A and B, revealing a (2 × 4) superstructure that is mirrored along an axis parallel to the $[\overline{42}.1]$ direction.

A similar situation is found for the islands of type B as shown in Fig. 10.2(b). An island with an apparent height of 0.5 nm is seen. As for island type A, areas with an apparent height of 0.8 nm are present that are tentatively assigned to a second molecular layer. Additionally, a few defects are observed in the monolayer film (lower right part of the image). The monolayer island of type B exhibit faint lines that are oriented at an angle of −52 ± 3° with respect to the $[\overline{42}.1]$ direction.

The orientation of these lines indicates that the two island types represent the same molecular adsorption structure that is mirror imaged along an axis parallel to the $[\overline{42}.1]$ direction. This assumption is further corroborated by the high-resolution images given in Fig. 10.2(c) and (d).

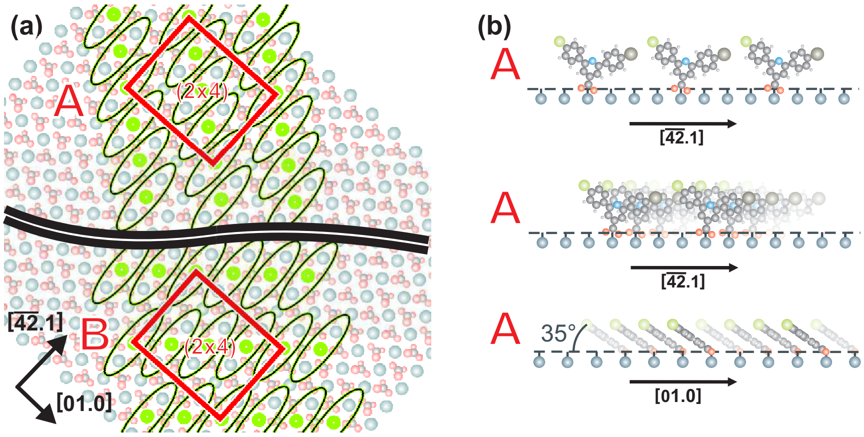

Figure 10.3: Tentative model for (a) the molecular arrangement of the molecules in type A and B islands. The structures are mirror-imaged along an axis oriented along the $[\overline{42}.1]$ direction. (b) Side view of the proposed arrangement of the molecules within island A. The structure for the molecules within island type B is the same, but mirrored.

A high-resolution image of a type A island is shown in Fig. 10.2(c). The faint lines can be resolved as individual features that arrange in rows. The periodic pattern is in agreement with a (2 × 4) superstructure as shown by the superimposed unit cell. A similar but mirrored situation is seen for the islands of type B as given in Fig. 10.2(d). Individual features are resolved that align in rows, resulting in a (2 × 4) superstructure. (An area with second-layer occupation is also seen in Fig. 10.2(d), which no further discussed here.)

Based on these NC-AFM images, I can propose a tentative model of the molecular structure in the monolayer islands as discussed in Fig. 10.3. The (2 × 4) superstructure of island type A (b) is shown in the upper (lower) part of Fig. 10.3(a). I ascribe each individually resolved feature to a single molecule. Based on the size of the molecules and the measured island height, I expect the molecules to be standing upright on the surface in a tilted fashion.

Assuming that the molecules anchor towards the surface with the carboxylic acid anchor, the bright feature might be associated with a protruding halide atom. It is to note that I only image one of the two halide atoms, which can be readily understood by a tilted arrangement and/or different interaction strength with the AFM tip, resulting in different apparent heights. As shown by the ellipses indicating the approximate size of the molecule, my model fits excellently to the assumption of a (2 × 4) superstructure containing three molecules. The side views along the [01.0] and $[\overline{42}.1]$ directions are given in Fig. 10.3(b).

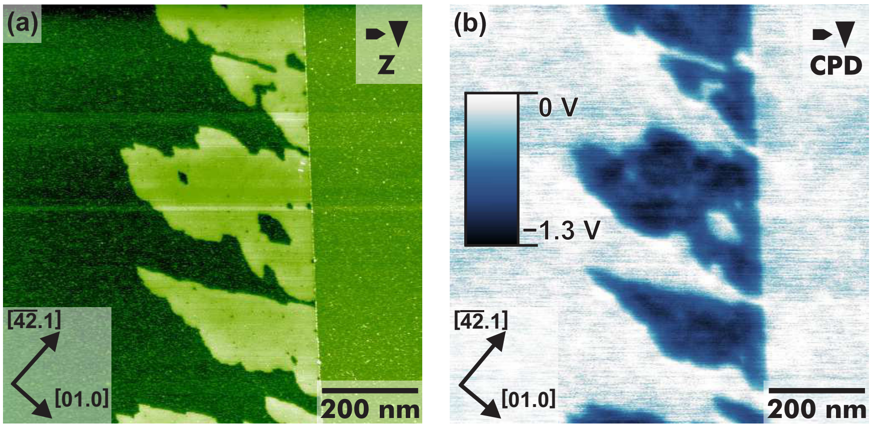

Figure 10.4: Kelvin probe force microscopy information: (a) Topography image showing BPCPPCA molecule islands on the calcite(10.4) surface. (b) Corresponding KPFM image with the bare calcite surface set to about 0 V.

I propose a anchoring of the carboxylic acid moiety towards the surface. Given the large negative shift of the contact potential of the islands with respect to the calcite surface (see Fig. 10.4), I assume that the carboxylic acid group is deprotonated. This assumption is in excellent agreement with previous studies revealing the deprotonation of a benzoic acid derivative presented in Chap. 7, 8 and 9. The negatively charged carboxylate group is expected to anchor towards the positively charged surface calcium cations. However, it is important to mention that the discussion made here does not depend on the protonation state of the carboxylic acid moiety.

Along the [01.0] direction, the molecules are stacked in a shifted arrangement, which can be easily motivated by optimization of π-π interaction of the phenyl rings. Finally, to allow for π-π interaction and probably halogen-π interaction [159], the molecules are assumed to tilt with an angle of approximately 35°, which results in an optimum molecule-molecule distance of 0.3 nm for π-π interaction. Although height measurements in NC-AFM must not be taken literally, I note that the apparent height of 0.5 nm is in good agreement with this tilted arrangement.

A First Heating Step

The situation as revealed after deposition onto the surface held at room temperature changes drastically upon annealing the substrate to 570 K, indicating a significant change in the molecular structure. A representative NC-AFM is given in Fig. 10.2(a). Instead of ordered islands, chain-like structures are formed on the surface. Although the overall ordering is poor compared to the islands, two main orientations of the chain-like structures (marked with I and II) can be identified. The two orientations span an angle of approximately 49 ± 3°.

A zoom into the chain structure of type II as shown in Fig. 10.2(b) reveals a periodic structure within the chain. The same holds true for the chains of type I as shown in Fig. 10.5(c). The spanning angle of 49° can be obtained by considering an angle of +67 ± 3° and −64 ± 3° with respect to the $[\overline{42}.1]$ direction for the I and II chains. Thus, this angle and the similarity of the two chain structures indicate that these two structures are, in fact, identical but mirror-imaged structures.

To elucidate the details of these structures, I note that the individual features imaged within these chains appear significantly larger than the individual features within the ordered islands observed before. This indicates that the envisioned linking reaction has taken place upon homolytic cleavage of the bromide atoms. A dimer structure that is covalently linked at the formed bromine position (6,6'-([1,1'-biphenyl]-4,4'-diyl)bis(2-(4-chlorophenyl)isonicotinic acid)) exhibits either a U or an S-like shape.

Assuming that the dimer molecules anchor with the two carboxylate groups towards the surface calcium cations results in well-defined adsorption positions. The S form is expected to be thermodynamically more favorable. Moreover, when assuming the surface calcium atom as suitable adsorption position for the chlorine atoms, the S form is clearly favored over the U form. Optimizing the intermolecular distance to allow for halogen-π

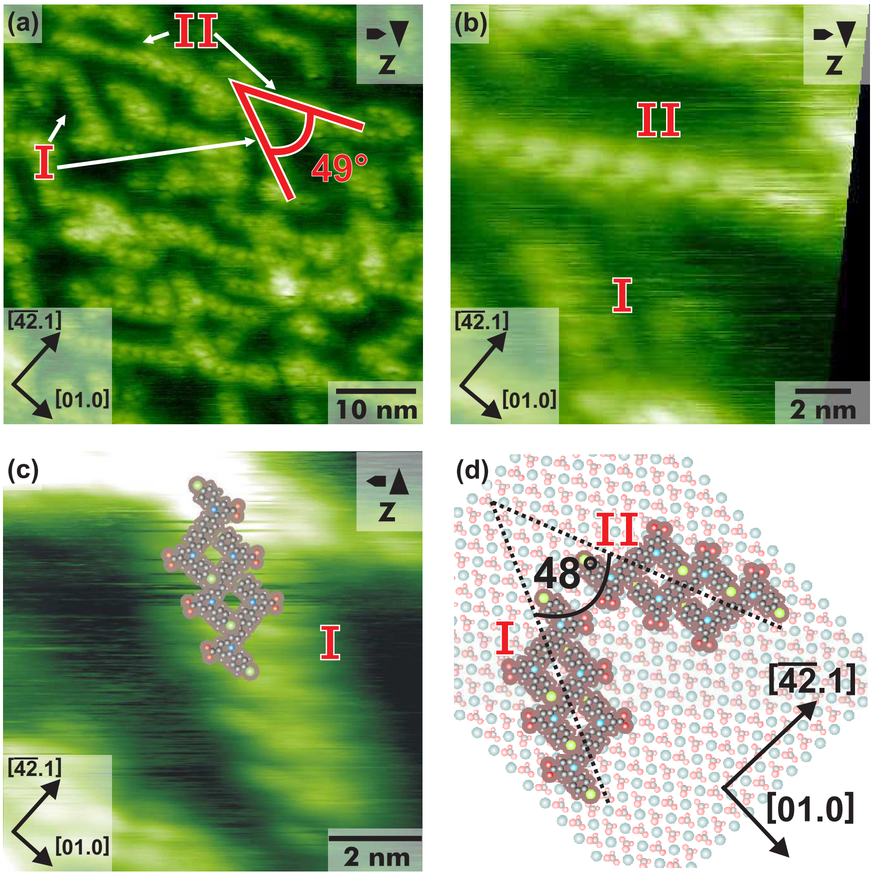

Figure 10.5: Distinctly different structure obtained after annealing the substrate to about 570 K for 1 h. (a) Overview image, revealing chain-like structures forming two types (I and II spanning an angle of approximately 49 ± 3°). (b) Drift-corrected detail image for chain type II. (c) Drift-corrected detail image for chain type I with superimposed model. (d) Proposed model for the two different chain types on calcite(10.4).

interaction can be understood as the driving force behind the lateral shift of the molecules perpendicular to the row direction. This readily results in a molecular chain that forms an angle of either +66 or −66° with respect to the $[\bar{4}2.1]$ direction as observed in the experiment.

I thus conclude this part by summarizing that significantly different structures are obtained upon moderate annealing, namely molecular chain structures. The individual features within the chains fit in size with dimer molecules. Moreover, the observed chain structure can be readily explained by a rational assembly of the dimers. All three findings agree well with the assignment of a first covalent reaction step involving the cleavage of the bromine-phenyl bond.

Second Linking Step

Next, I anneal the surface with the chain-like structures in a second step to 610 K. The resulting structures are shown in Fig. 10.2. Most strikingly, the molecular structures that are present on the surface after the second annealing steps are, again, distinctly different from both, the as-deposited ordered islands and the chain-like structures observed after the first, moderate annealing step.

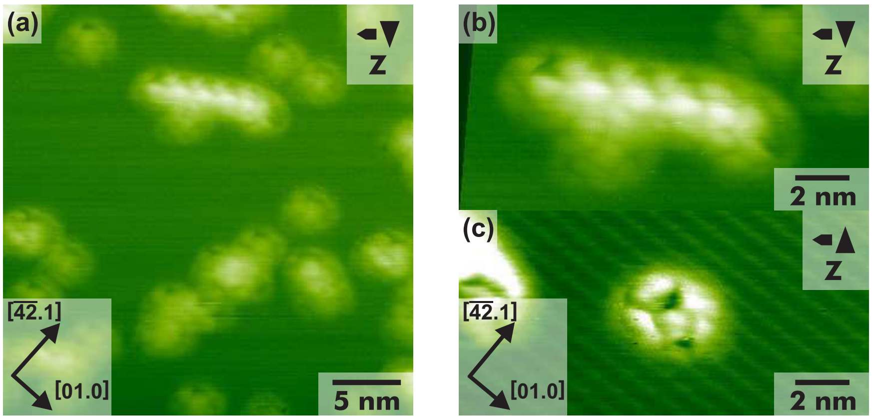

Figure 10.6: Structures observed after the second annealing step to 610 K for 1 h. (a) Rows oriented along an angle of +60 ± 3° with respect to the [$\overline{42}.1$] direction and ring-like features are observed to coexist on the surface. (b) High-resolution image of an extended row structure. (c) High-resolution image of a closed ring structure. Note that the rows running from the upper left to lower right originate from the calcite(10.4) substrate.

Now, rows oriented along an angle of +60 ± 3° with respect to the [$\overline{42}.1$] direction and ring-like features are observed to coexist on the surface (Fig. 10.6(a)). The rows (Fig. 10.6(b)) differ in appearance and, most notably, in orientation with respect to the underlying substrate lattice, clearly indicating that the rows are composed of other building blocks than the chain-like structures revealed after moderate annealing.

Moreover, ring-like features (Fig. 10.6(c)) are seen on the surface, exhibiting a distinct internal structure. To elucidate the structural details, I first consider the row structure as shown in Fig. 10.7(a). A periodic structure is clearly resolved that fits excellently in size with a structure that is composed by further linking of the dimer molecules via cleaving the chlorine-phenyl bond.

Arranging the model such that the carboxylate groups can bind towards the calcium cations results in an angle of +61° with respect to the [$\overline{42}.1$] direction, that is exactly what is observed experimentally. Thus, the size match, the agreement of the periodic repeat distance and the observed orientation on the surface corroborate the model of a further linking of the dimer units in a zig-zag polymer.

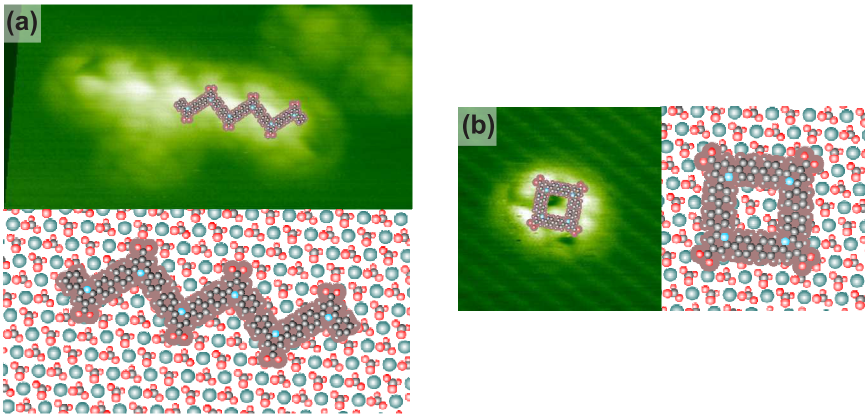

Figure 10.7: High-resolution images after the second annealing step. (a) Drift-corrected image of the row structure and proposed model. (b) Drift-corrected image of the ring structure with proposed model.

Considering the dimer units reveals that a second structure is feasible when linking the dimer building blocks, namely a closed ring. This structure is observed experimentally. The detailed analysis in Fig. 10.7(b) confirms the excellent size match. Moreover, the internal structure seen as dark stripes in the ring-like feature suggests that the four initial precursor molecules are resolved. I assign the bright part to the carboxylate group that is again positioned atop a surface calcium atom.

In the proposed model three out of the four carboxylate groups can attain perfect on-top positions while the forth group does not fit to the surface lattice. This size mismatch of the ring structure with the underlying calcite lattice might be the explanation for the fact that I frequently observe one of the four bright features different from the three other bright features within a ring.

To summarize the results of the second annealing step I note that yet different structures are obtained after the second activation step. Two coexisting structures are revealed, as expected from the structure of the molecular precursors. Extended rows can be identified that fit is size, periodicity and orientation to the model of a further linked zig-zag polymer. Linking two dimers in a closed fashion results in ring-like features that are observed to coexist on the surface. The sum of these experimental findings strongly indicates the successful activation of the second reaction step involving the chlorine-phenyl bond.

Summary and Conclusions

In conclusion, I present the first successful example of a two-step polymerization reaction on a bulk insulating surface. Carefully selecting a precursor molecule that provides both the encoding of the selective and sequential reaction sites as well as suitable anchor groups for preventing desorption is demonstrated to result in hierarchical polymerization. Extended zig-zag and closed ring structures are created upon sequential activation of homolytic cleavage of first bromine-phenyl and second chlorine-phenyl bonds. This work demonstrates that enhanced structural control in on-surface synthesis can be achieved even on the weakly interacting surface of a bulk insulator.

11 Summary

In conclusion, this thesis describs for the first time the covalent coupling of organic molecules on a bulk insulator, namely calcite. By using state-of-the-art non-contact atomic force and Kelvin probe force microscopy at room temperature, fundamental molecular processes were analyzed in terms of molecule-surface interactions as well as chemical transformations and reactivity.

In Chap. 6, the molecule-surface interaction is enhanced by an excellent geometrical match of the molecular structure of BPDCA to the substrate dimensions. A very pronounced row structure is obtained based on a favorable adsorption position with both carboxyl groups anchoring toward the calcite surface, causing a strong surface templating effect. A second structure is formed by molecules that can form hydrogen bonds as present in the bulk structure. The subtle balance between molecule-surface and intermolecular interactions is expressed by the coexistence between these two different molecular structures, allowing for gaining insights into the driving forces behind the molecular self-assembly.

The direct visualization of molecule deprotonation on calcite is presented in Chap. 7. Two phases are observed to coexist after deposition of DHBA molecules. High-resolution images are shown to change in time form a transient bulk-like phase into a stable dense phase. The transition is understood by considering the protonation state of the molecules. While the bulk-like, hydrogen-bonded structure requires the molecules to be protonated, the resulting dense phase is driven by electrostatic interaction of the deprotonated carboxylate moieties with the surface calcium cations. The high-resolution capability of Kelvin probe force microscopy allows to reveal the intramolecular charge distribution within a single DHBA molecule depending on the protonation state.

By controlled deprotonation the activation of substrate templating is demonstrated as shown, in Chap. 8. Upon deposition of IBA molecules on the natural cleavage plane of calcite, islands only nucleate at step edges, indicating the weak molecule-surface interaction. Annealing the substrate, the molecules undergo a transition from the protonated to the deprotonated state. In the deprotonated state, the molecules adopt a well-defined adsorption position, resulting in a distinctly different, substrate-templated molecular structure.

The first successful covalent linking of halide-substituted benzoic acid molecules on the same surface is demonstrated in Chap. 9. The deprotonated carboxylate acid group is exploited to avoid desorption of the precursor molecules upon thermal activation required for the linkling reaction. Moreover, the presence of the carboxylate group being a strong electron donor is expected to weaken the phenyl-halide bond and, therefore, favour homolytic cleavage of this bond to give reactive phenyl radicals at moderate temperatures without the need of a coupling catalyst. The specificity of this approach is confirmed by creating conjugated molecular wires, zig-zag structures as well as dimers by exploiting different substitution position as well as changing the number of halide substituted atoms.

Building upon this achievement, a two-step linking reaction on the insulating calcite surface is presented in Chap. 10. For inducing site-specific and sequential covalent linking, a precursor molecule is chosen that provides bromophenyl and chlorophenyl groups, having different dissociation energies for homolytic cleavage of the halide-phenyl bonds. Following a first heating step, a chain structure of the self-assembled precursor dimers is explained by dissociation of the bromine-carbon bond. Upon the second, higher thermal activation step involving the chlorine-phenyl bond, extended zig-zag and closed ring structures are created. Therefore, the reaction sites and sequential order are encoded in the molecular structure, providing so far unmatched reaction control in on-surface synthesis on an insulating surface.

The results of this thesis, therefore, constitute a significant step towards exploiting on-surface synthesis for molecular electronics and related applications. The described approaches and methods will assist producing future molecular electronics. This will allow for benefiting from conjugated carbon nanostructures as functional materials in integrated circuits instead of the present silicon-based electronics.

Bibliography

[1] G. E. Moore: Cramming More Components onto Integrated Circuits.
Electronics **38**, 114 (1965)

[2] M. Kaku: Physics of the Future. Knopf Doubleday Publishing Group, 2011

[3] A. Aviram, M. A. Ratner: Molecular Rectifiers.
Chemical Physics Letters **29**, 277 (1974)

[4] Z. J. Donhauser, B. A. Mantooth, K. F. Kelly, L. A. Bumm, J. D. Monnell, J. J. Stapleton, D. W. Price, A. M. Rawlett, D. L. Allara, J. M. Tour, P. S. Weiss: Conductance switching in single molecules through conformational changes.
Science **292**, 2303 (2001)

[5] M. Fuechsle, J. A. Miwa, S. Mahapatra, H. Ryu, S. Lee, O. Warschkow, L. C. L. Hollenberg, G. Klimeck, M. Y. Simmons: A single-atom transistor.
Nature Nanotechnology **7**, 242 (2012)

[6] M.-K. Ng, D.-C. Lee, L. Yu: Molecular Diodes Based on Conjugated Diblock Co-oligomers.
Journal of the American Chemical Society **124**, 11862 (2002)

[7] G. M. Whitesides, J. P. Mathias, C. T. Seto: Molecular self-assembly and nanochemistry: a chemical strategy for the synthesis of nanostructures.
Science **254**, 1312 (1991)

[8] A. GOURDON: On-surface covalent coupling in ultrahigh vacuum.
Angewandte Chemie – International Edition **47**, 6950 (2008)

[9] G. BINNIG, H. ROHRER, C. GERBER, E. WEIBEL: Surface studies by scanning tunneling microscopy.
Physical Review Letters **49**, 57 (1982)

[10] NOBEL MEDIA AB: Press Release: The 1986 Nobel Prize in Physics. Nobelprize.org, 1986

[11] G. BINNIG, H. ROHRER, C. GERBER, E. WEIBEL: 7 x 7 Reconstruction on silicon(111) resolved in real space.
Physical Review Letters **50**, 120 (1983)

[12] G. BINNIG, C. QUATE, C. GERBER: Atomic Force Microscope.
Physical Review Letters **56**, 930 (1986)

[13] S. SADEWASSER, T. GLATZEL: Kelvin Probe Force Microscopy: Measuring and Compensating Electrostatic Forces. Springer-Verlag, 2012

[14] G. MEYER, N. M. AMER: Novel optical approach to atomic force microscopy.
Applied Physics Letters **53**, 2400 (1988)

[15] Z. F. SHAO, J. YANG, A. P. SOMLYO: Biological atomic force microscopy: From microns to nanometers and beyond.
Annual Review of Cell and Developmental Biology **11**, 241 (1995)

[16] J. HU, M. WANG, H. U. G. WEIER, P. FRANTZ, W. KOLBE, D. F. OGLETREE, M. SALMERON: Imaging of single extended DNA molecules on flat (aminopropyl)triethoxysilane-mica by atomic force microscopy.
Langmuir **12**, 1697 (1996)

[17] F. J. GIESSIBL: Atomic resolution of the silicon (111)-(7x7) surface by atomic force microscopy.
Science **267**, 68 (1995)

[18] S. KITAMURA, M. IWATSUKI: Observation of silicon surfaces using ultrahigh-vacuum noncontact atomic force microscopy.
Japanese Journal of Applied Physics, Part 2: Letters **35**, L668 (1996)

[19] C. BARTH, A. S. FOSTER, C. R. HENRY, A. L. SHLUGER: Recent Trends in Surface Characterization and Chemistry with High-Resolution Scanning Force Methods.
Advanced Materials **23**, 477 (2011)

[20] S. MAGONOV, M. WHANGBO, S. MAGONOV: Surface Analysis with STM and AFM: Experimental and Theoretical Aspects of Image Analysis. Wiley-VCH, 1996

[21] S. MORITA, R. WIESENDANGER, E. MEYER: Noncontact Atomic Force Microscopy. Springer-Verlag, 2002

[22] G. BAYM: Lectures on Quantum Mechanics: Lecture Notes and Supplements in Physics. Perseus Books Group, 1990

[23] J. N. ISRAELACHVILI: Intermolecular and Surface Forces. Academic Press, 2011

[24] H. C. HAMAKER: The London-van der Waals attraction between spherical particles.
Physica (The Hague) **4**, 1058 (1937)

[25] C. BARTH, C. R. HENRY: Atomic resolution imaging of the (001) surface of UHV cleaved MgO by dynamic scanning force microscopy.
Physical Review Letters **91**, 196102 (2003)

[26] W. MELITZ, J. SHEN, A. C. KUMMEL, S. LEE: Kelvin probe force microscopy and its application.
Surface Science Reports **66**, 1 (2011)

[27] F. J. GIESSIBL: Advances in atomic force microscopy. Reviews of Modern Physics **75**, 949 (2003)

[28] Y. MARTIN, C. C. WILLIAMS, H. K. WICKRAMASINGHE: Atomic force microscope-force mapping and profiling on a sub 100-Å scale.
Journal of Applied Physics **61**, 4723 (1987)

[29] T. R. ALBRECHT, P. GRÜTTER, D. HORNE, D. RUGAR: Frequency-Modulation Detection Using High-Q Cantilevers for Enhanced Force Microscope Sensitivity.
Journal of Applied Physics **69**, 668 (1991)

[30] J. LÜBBE, H. SCHNIEDER, M. REICHLING: Pressure dependence of the Q-factor of cantilevers used for NC-AFM.
e-Journal of Surface Science and Nanotechnology **9**, 30 (2011)

[31] P. RAHE: The Calcite($10\bar{1}4$) Surface: A Versatile Substrate for Molecular Self-Assembly, PhD thesis, 2011

[32] J. LÜBBE, M. TEMMEN, S. RODE, P. RAHE, A. KÜHNLE, M. REICHLING: Thermal noise limits for ultra-high vacum non-contact atomic force microscopy.
Beilstein Journal of Nanotechnology **4**, 32 (2013)

[33] W. KELVIN: Contact Electricity of Metals. W. Clowes and sons, 1897

[34] W. A. ZISMAN: A new method of measuring contact potential differences in metals.
Review of Scientific Instruments **3**, 367 (1932)

[35] M. NONNENMACHER, M. P. O'BOYLE, H. K. WICKRAMASINGHE: Kelvin probe force microscopy.
Applied Physics Letters **58**, 2921 (1991)

[36] H. HOPPE, T. GLATZEL, M. NIGGEMANN, A. HINSCH, M. C. LUX-STEINER, N. S. SARICIFTCI: Kelvin Probe Force Microscopy Study on Conjugated Polymer/Fullerene

Bulk Heterojunction Organic Solar Cells.
Nano Letters **5**, 269 (2005)

[37] L. LIU, G. LI: Electrical characterization of single-walled carbon nanotubes in organic solar cells by Kelvin probe force microscopy.
Applied Physics Letters **96**, 083302 (2010)

[38] A. K. SINENSKY, A. M. BELCHER: Label-free and high-resolution protein: DNA nanoarray analysis using Kelvin probe force microscopy.
Nature Nanotechnology **2**, 653 (2007)

[39] L. GROSS, F. MOHN, P. LILJEROTH, J. REPP, F. J. GIESSIBL, G. MEYER: Measuring the Charge State of an Adatom with Noncontact Atomic Force Microscopy.
Science **324**, 1428 (2009)

[40] F. MOHN, L. GROSS, N. MOLL, G. MEYER: Imaging the charge distribution within a single molecule.
Nature Nanotechnology **7**, 227 (2012)

[41] A. HINAUT, A. PUJOL, F. CHAUMETON, D. MARTROU, A. GOURDON, S. GAUTHIER: An NC-AFM and KPFM study of the adsorption of a triphenylene derivative on KBr(001).
Beilstein Journal of Nanotechnology **3**, 221 (2012)

[42] J. HOLLAS: Moderne Methoden in der Spektroskopie. Vieweg & Teubner, 1995

[43] R. WIESENDANGER: Scanning Probe Microscopy an Spectroscopy: Methods and Applications. Cambridge University Press, 1994

[44] R. MÖLLER, C. BAUR, A. ESSLINGER, P. KURZ: Scanning noise potentiometry.
Journal of Vacuum Science and Technology B **9**, 609 (1991)

[45] J. M. R. WEAVER, D. W. ABRAHAM: High resolution atomic force microscopy potentiometry.

Journal of Vacuum Science and Technology, B: Microelectronics and Nanometer Structures **9**, 1559 (1991)

[46] M. YASUTAKE, D. AOKI, M. FUJIHIRA: Surface potential measurements using the Kelvin probe force microscope. Thin Solid Films **273**, 279 (1996)

[47] A. GIL, J. COLCHERO, J. GÓMEZ-HERRERO, A. M. BARÓ: Electrostatic force gradient signal: resolution enhancement in electrostatic force microscopy and improved Kelvin probe microscopy.
Nanotechnology **14**, 332 (2003)

[48] U. ZERWECK, C. LOPPACHER, T. OTTO, S. GRAFSTRÖM, L. M. ENG: Accuracy and resolution limits of Kelvin probe force microscopy.
Physical Review B **71**, 125424 (2005)

[49] J. SCHÜTTE: Abbildung organischer Moleküle auf dielektrischen Oberflächen, PhD thesis, 2009

[50] M. NIMMRICH: Atomic-scale characterization of diamond surfaces and fullerene self-assembly, PhD thesis, 2012

[51] R. BECHSTEIN: Pristine and Doped Titaniuim Dioxide Studies by NC-AFM, PhD thesis, 2009

[52] R. BECHSTEIN, C. GONZÁLEZ, J. SCHÜTTE, P. JELÍNEK, R. PÉREZ, A. KÜHNLE: 'All-inclusive' imaging of the rutile TiO_2(110) surface using NC-AFM.
Nanotechnology **20**, 505703 (2009)

[53] J. SCHÜTTE, P. RAHE, L. TRÖGER, S. RODE, R. BECHSTEIN, M. REICHLING, A. KÜHNLE: Clear signature of the (2x1) reconstruction of calcite $(10\bar{1}4)$.
Langmuir **26**, 8295 (2010)

[54] M. NIMMRICH, M. KITTELMANN, P. RAHE, A. MAYNE, G. DUJARDIN, A. SCHMIDSFELD, M. REICHLING, W. HARNEIT, A. KÜHNLE: Atomic-resolution imaging of clean and hydrogen-terminated C(100)-(2 x 1) diamond

surfaces using noncontact AFM.
Physical Review B **81**, 201403R (2010)

[55] M. SCHUNACK: Scanning Tunneling Microscopy Studies of Organic Molecules on Metal Surfaces, PhD thesis, 2002

[56] M. KNUDSEN: Experimentelle Bestimmung des Druckes gesättigter Quecksilberdämpfe bei 0° und höheren Temperaturen.
Annalen der Physik (1909)

[57] F. LOSKE, R. BECHSTEIN, J. SCHÜTTE, F. OSTENDORF, M. REICHLING, A. KÜHNLE: Growth of ordered C_{60} islands on $TiO_2(110)$.
Nanotechnology **20**, 065606 (2009)

[58] F. LOSKE, A. KÜHNLE: Manipulation of C_{60} islands on the rutile $TiO_2(110)$ surface using non-contact atomic force microscopy.
Applied Physics Letters **95**, 043110 (2009)

[59] F. LOSKE, P. RAHE, A. KÜHNLE: Contrast inversion in non-contact atomic force microscopy imaging of C_{60} molecules.
Nanotechnology **20**, 264010 (2009)

[60] P. RAHE, M. NIMMRICH, A. NEFEDOV, M. NABOKA, C. WÖLL, A. KÜHNLE: Transition of Molecule Orientation during Adsorption of Terephthalic Acid on Rutile $TiO_2(110)$.
Journal of Physical Chemistry C **113**, 17471 (2009)

[61] J. SCHÜTTE, R. BECHSTEIN, P. RAHE, M. ROHLFING, H. LANGHALS, A. KÜHNLE: Imaging perylene derivatives on rutile $TiOC_2(110)$ by noncontact atomic force microscopy.
Physical Review B **79**, 045428 (2009)

[62] J. SCHÜTTE, R. BECHSTEIN, M. ROHLFING, M. REICHLING, A. KÜHNLE: Cooperative mechanism for anchoring

highly polar molecules at an ionic surface.
Physical Review B **80**, 205421 (2009)

[63] F. Loske, J. Lübbe, J. Schütte, M. Reichling, A. Kühnle: Quantitative description of C_{60} diffusion on an insulating surface.
Physical Review B **82**, 155428 (2010)

[64] P. Rahe, M. Nimmrich, A. Greuling, J. Schütte, I. Starà, J. Rybàček, G. Huerta-Angeles, I. Starỳ, M. Rohlfing, A. Kühnle: Toward Molecular Nanowires Self-Assembled on an Insulating Substrate: Heptahelicene-2-carboxylic acid on Calcite $(10\bar{1}4)$.
Journal of Physical Chemistry C **114**, 1547 (2010)

[65] F. Loske, M. Reichling, A. Kühnle: Deposition Sequence Determines Morphology of C_{60} and 3,4,9,10-Perylenetetracarboxylic Diimide Islands on $CaFC_2(111)$.
Japanese Journal of Applied Physics **50**, 08LB07 (2011)

[66] M. Kittelmann, P. Rahe, M. Nimmrich, C. M. Hauke, A. Gourdon, A. Kühnle: On-Surface Covalent Linking of Organic Building Blocks on a Bulk Insulator.
ACS nano **5**, 8420 (2011)

[67] F. Loske, M. Reichling, A. Kühnle: Steering molecular island morphology on an insulator surface by exploiting sequential deposition.
Chemical Communications **47**, 10386 (2011)

[68] C. M. Hauke, P. Rahe, M. Nimmrich, J. Schütte, M. Kittelmann, I. Starà, I. Starỳ, J. Rybàček, A. Kühnle: Molecular Self-Assembly of Enantiopure Heptahelicene-2-Carboxylic Acid on Calcite $(10\bar{1}4)$.
Journal of Physical Chemistry C **116**, 4637 (2012)

[69] M. Nimmrich, M. Kittelmann, P. Rahe, W. Harneit, A. J. Mayne, G. Dujardin, A. Kühnle: Influence of charge transfer doping on the morphologies of C_{60} islands on hydrogenated diamond C(100)-(2 x 1).
Physical Review B **85**, 035420 (2012)

[70] M. Kittelmann, P. Rahe, M. Nimmrich, C. M. Hauke, A. Gourdon, A. Kühnle: Direct Visualization of Molecule Deprotonation on an Insulating Surface.
ACS nano **6**, 7406 (2012)

[71] P. Rahe, R. Lindner, M. Kittelmann, M. Nimmrich, A. Kühnle: From dewetting to wetting molecular layers: C_{60} on $CaCO_3(10\bar{1}4)$ as a case study.
Physical Chemistry Chemical Physics **14**, 6544 (2012)

[72] P. Rahe, M. Nimmrich, A. Kühnle: Substrate Templating upon Self-Assembly of Hydrogen-Bonded Molecular Networks on an Insulating Surface.
Small **8**, 2968 (2012)

[73] M. Kittelmann, P. Rahe, A. Kühnle: Molecular self-assembly on an insulating surface: interplay between substrate templating and intermolecular interactions.
Journal of Physics-Condensed Matter **24**, 354007 (2012)

[74] L. Tröger, J. Schütte, F. Ostendorf, A. Kühnle, M. Reichling: Concept for support and cleavage of brittle crystals.
Review of Scientific Instruments **80**, 063703 (2009)

[75] P. Rahe, R. Bechstein, A. Kühnle: Vertical and lateral drift corrections of scanning probe microscopy images.
J. Vac. Sci. Technol. B **28**, C4E31 (2010)

[76] H. Binder: Lexikon der chemischen Elemente. Hirzel, 1999

[77] K. W. Bladh, R. A. Bideaux, E. Anthony-Morton, B. G. Nichols: Calcite. In: *Handbook of Mineralogy* Bd. V. Chantilly, VA : Mineralogical Society of America, 2003

[78] J. W. Gifford: The refractive indices of Fluorite, Quartz, and Calcite.
Proceedings of the Royal Society of London **70**, 329 (1902)

[79] D. W. THOMPSON, M. J. DEVRIES, T. E. TIWALD, J. A. WOOLLAM: Determination of optical anisotropy in calcite from ultraviolet to mid-infrared by generalized ellipsometry.
Thin Solid Films **313-314**, 341 (1998)

[80] R. REEDER, M. S. O. AMERICA: Carbonates: mineralogy and chemistry. Mineralogical Society of America, 1983

[81] L. ADDADI, S. WEINER: Control and design principles in biological mineralization.
Angewandte Chemie – International Edition **31**, 153 (1992)

[82] J. RIEGER, J. THIEME, C. SCHMIDT: Study of precipitation reactions by X-ray microscopy: $CaCO_3$ precipitation and the effect of polycarboxylates.
Langmuir **16**, 8300 (2000)

[83] P. RAHE, J. SCHÜTTE, A. KÜHNLE: NC-AFM contrast formation on the calcite $(10\bar{1}4)$ surface.
Journal of Physics-Condensed Matter **24**, 084006 (2012)

[84] A. L. RACHLIN, G. S. HENDERSON, M. C. GOH: An atomic force microscope (AFM) study of the calcite cleavage plane: image averaging in Fourier space.
American Mineralogist **77**, 904 (1992)

[85] S. L. S. STIPP, C. M. EGGLESTON, B. S. NIELSEN: Calcite Surface-Structure Observed at Microtopographic and Molecular Scales with Atomic-Force Microscopy (AFM).
Geochimica Et Cosmochimica Acta **58**, 3023 (1994)

[86] N. NILIUS, T. RISSE, S. SCHAUERMANN, S. SHAIKHUTDINOV, M. STERRER, H. J. FREUND: Model studies in catalysis.
Topics in Catalysis **54**, 4 (2011)

[87] C. JOACHIM, J. K. GIMZEWSKI, A. AVIRAM: Electronics using hybrid-molecular and mono-molecular devices.
Nature **408**, 541 (2000)

[88] J. V. Barth, G. Costantini, K. Kern: Engineering atomic and molecular nanostructures at surfaces.
Nature **437**, 671 (2005)

[89] D. F. Perepichka, F. Rosei: Extending Polymer Conjugation into the Second Dimension.
Science **323**, 216 (2009)

[90] J. Mendez, M. F. Lopez, J. A. Martin-Gago: On-surface synthesis of cyclic organic molecules.
Chemical Society Reviews **40**, 4578 (2011)

[91] S.-W. Hla, L. Bartels, G. Meyer, K.-H. Rieder: Inducing All Steps of a Chemical Reaction with the Scanning Tunneling Microscope Tip: Towards Single Molecule Engineering.
Physical Review Letters **85**, 2777 (2000)

[92] F. Ullmann, J. Bielecki: Ueber Synthesen in der Biphenylreihe.
Berichte der deutschen chemischen Gesellschaft **34**, 2174 (1901)

[93] L. Grill, M. Dyer, L. Lafferentz, M. Persson, M. V. Peters, S. Hecht: Nano-architectures by covalent assembly of molecular building blocks.
Nature Nanotechnology **2**, 687 (2007)

[94] J. A. Lipton-Duffin, O. Ivasenko, D. F. Perepichka, F. Rosei: Synthesis of Polyphenylene Molecular Wires by Surface-Confined Polymerization.
Small **5**, 592 (2009)

[95] J. A. Lipton-Duffin, J. A. Miwa, M. Kondratenko, F. Cicoira, B. G. Sumpter, V. Meunier, D. F. Perepichka, F. Rosei: Step-by-step growth of epitaxially aligned polythiophene by surface-confined reaction.
Proceedings of the National Academy of Sciences **107**, 11200 (2010)

[96] L. Lafferentz, F. Ample, H. Yu, S. Hecht,

C. JOACHIM, L. GRILL: Conductance of a Single Conjugated Polymer as a Continuous Function of Its Length.
Science **323**, 1193 (2009)

[97] C. H. SCHMITZ, J. IKONOMOV, M. SOKOLOWSKI: Two-Dimensional Ordering of Poly(p-phenyleneterephthalamide) on the Ag(111) Surface Investigated by Scanning Tunneling Microscopy.
Journal of Physical Chemistry C **113**, 11984 (2009)

[98] M. BIERI, S. BLANKENBURG, M. KIVALA, C. A. PIGNEDOLI, P. RUFFIEUX, K. MÜLLEN, R. FASEL: Surface-supported 2D heterotriangulene polymers.
Chemical Communications **47**, 10239 (2011)

[99] M. BIERI, M. TREIER, J. M. CAI, K. AÏT-MANSOUR, P. RUFFIEUX, O. GRÖNING, P. GRÖNING, M. KASTLER, R. RIEGER, X. L. FENG, K. MÜLLEN, R. FASEL: Porous graphenes: two-dimensional polymer synthesis with atomic precision.
Chemical Communications **45**, 6919 (2009)

[100] R. GUTZLER, H. WALCH, G. EDER, S. KLOFT, W. M. HECKL, M. LACKINGER: Surface mediated synthesis of 2D covalent organic frameworks: 1,3,5-tris(4-bromophenyl)benzene on graphite(001), Cu(111), and Ag(110).
Chemical Communications **29**, 4456 (2009)

[101] R. SCHOLL, C. SEER: Abspaltung aromatisch gebundenen Wasserstoffs und Verknüpfung aromatischer Kerne durch Aluminiumchlorid.
Justus Liebigs Annalen der Chemie **394**, 111 (1912)

[102] J. M. CAI, P. RUFFIEUX, R. JAAFAR, M. BIERI, T. BRAUN, S. BLANKENBURG, M. MUOTH, A. P. SEITSONEN, M. SALEH, X. L. FENG, K. MÜLLEN, R. FASEL: Atomically precise bottom-up fabrication of graphene nanoribbons.
Nature **466**, 470 (2010)

[103] M. Matena, T. Riehm, M. Stöhr, T. A. Jung, L. H. Gade: Transforming surface coordination polymers into covalent surface polymers: Linked polycondensed aromatics through oligomerization of N-heterocyclic carbene intermediates.
Angewandte Chemie – International Edition **47**, 2414 (2008)

[104] S. Weigelt, C. Busse, C. Bombis, M. M. Knudsen, K. V. Gothelf, T. Strunskus, C. Woll, M. Dahlbom, B. Hammer, E. Laegsgaard, F. Besenbacher, T. R. Linderoth: Covalent interlinking of an aldehyde and an amine on a Au(111) surface in ultrahigh vacuum.
Angewandte Chemie – International Edition **46**, 9227 (2007)

[105] M. I. Veld, P. Iavicoli, S. Haq, D. B. Amabilino, R. Raval: Unique intermolecular reaction of simple porphyrins at a metal surface gives covalent nanostructures.
Chemical Communications **13**, 1536 (2008)

[106] S. Weigelt, C. Busse, C. Bombis, M. M. Knudsen, K. V. Gothelf, E. Laegsgaard, F. Besenbacher, T. R. Linderoth: Surface synthesis of 2D branched polymer nanostructures.
Angewandte Chemie – International Edition **47**, 4406 (2008)

[107] N. A. A. Zwaneveld, R. Pawlak, M. Abel, D. Catalin, D. Gigmes, D. Bertin, L. Porte: Organized formation of 2D extended covalent organic frameworks at surfaces.
Journal of the American Chemical Society **130**, 6678 (2008)

[108] L. Lafferentz, V. Eberhardt, C. Dri, C. Africh, G. Comelli, F. Esch, S. Hecht, L. Grill: Controlling on-surface polymerization by hierarchical and substrate-directed growth.
Nature Chemistry **4**, 215 (2012)

[109] A. Saywell, J. Schwarz, S. Hecht, L. Grill: Polymerization on Stepped Surfaces: Alignment of Polymers and Identification of Catalytic Sites.
Angewandte Chemie – International Edition **51**, 5096 (2012)

[110] M. Abel, S. Clair, O. Ourdjini, M. Mossoyan, L. Porte: Single Layer of Polymeric Fe-Phthalocyanine: An Organometallic Sheet on Metal and Thin Insulating Film.
Journal of the American Chemical Society **133**, 1203 (2011)

[111] C. Bombis, F. Ample, L. Lafferentz, H. Yu, S. Hecht, C. Joachim, L. Grill: Single Molecular Wires Connecting Metallic and Insulating Surface Areas.
Angewandte Chemie – International Edition **48**, 9966 (2009)

[112] J. M. Lehn: Supramolecular chemistry - molecules, supermolecules, and molecular functional units (Nobel lecture).
Angewandte Chemie **100**, 91 (1988)

[113] A. Hauschild, K. Karki, B. C. C. Cowie, M. Rohlfing, F. S. Tautz, M. Sokolowski: Molecular Distortions and Chemical Bonding of a Large p-Conjugated Molecule on a Metal Surface.
Physical Review Letters **94**, 036106 (2005)

[114] J. Ziroff, F. Forster, A. Schoell, P. Puschnig, F. Reinert: Hybridization of Organic Molecular Orbitals with Substrate States at Interfaces: PTCDA on Silver.
Physical Review Letters **104**, 233004 (2010)

[115] E. Bauer: Phänomenologische Theorie der Kristallabscheidung an Oberflächen I.
Zeitschrift fuer Kristallographie **110**, 372 (1958)

[116] A. Kühnle: Self-assembly of organic molecules at metal surfaces.

Current Opinion in Colloid and Interface Science **14**, 157 (2009)

[117] T. Dienel, C. Loppacher, S. C. B. Mannsfeld, R. Forker, T. Fritz: Growth-mode-induced narrowing of optical spectra of an organic adlayer.
Advanced Materials **20**, 959 (2008)

[118] S. A. Burke, W. Ji, J. M. Mativetsky, J. M. Topple, S. Fostner, H. J. Gao, H. Guo, P. Grütter: Strain induced dewetting of a molecular system: Bimodal growth of PTCDA on NaCl.
Physical Review Letters **100**, 186104 (2008)

[119] T. Kunstmann, A. Schlarb, M. Fendrich, T. Wagner, R. Möller, R. Hoffmann: Dynamic force microscopy study of 3,4,9,10-perylenetetracarboxylic dianhydride on KBr(001).
Physical Review B **71**, 121403 (2005)

[120] J. M. Topple, S. A. Burke, S. Fostner, P. Grütter: Thin film evolution: Dewetting dynamics of a bimodal molecular system.
Physical Review B **79**, 205414 (2009)

[121] J. M. Topple, S. A. Burke, W. Ji, S. Fostner, A. Tekiel, P. Grütter: Tailoring the Morphology and Dewetting of an Organic Thin Film.
Journal of Physical Chemistry C **115**, 217 (2011)

[122] S. A. Burke, J. M. Mativetsky, R. Hoffmann, P. Grütter: Nucleation and submonolayer growth of C_{60} on KBr.
Physical Review Letters **94**, 096102 (2005)

[123] S. A. Burke, J. M. Mativetsky, S. Fostner, P. Grütter: C_{60} on alkali halides: Epitaxy and morphology studied by noncontact AFM.
Physical Review B **76**, 035419 (2007)

[124] M. Körner, F. Loske, M. Einax, A. Kühnle, M. Re-

ICHLING, P. MAASS: Second-Layer Induced Island Morphologies in Thin-Film Growth of Fullerenes.
Physical Review Letters **107**, 016101 (2011)

[125] S. FREMY, A. SCHWARZ, K. LÄMMLE, M. PROSENC, R. WIESENDANGER: The monomer-to-dimer transition and bimodal growth of Co-salen on NaCl(001): a high resolution atomic force microscopy study.
Nanotechnology **20**, 405608 (2009)

[126] C. LOPPACHER, U. ZERWECK, D. KOEHLER, M. RODENSTEIN, E. JAEHNE, R. LUTHER, H.-J. ADLER, L. M. ENG: Physical vapour deposition of alkyl phosphonic acid on mica and HOPG investigated by NC-AFM.
Nanotechnology **18**, 084003 (2007)

[127] S. MAIER, L.-A. FENDT, L. ZIMMERLI, T. GLATZEL, O. PFEIFFER, F. DIEDERICH, E. MEYER: Nanoscale engineering of molecular porphyrin wires on insulating surfaces.
Small **4**, 1115 (2008)

[128] J. M. MATIVETSKY, S. A. BURKE, S. FOSTNER, P. GRUTTER: Nanoscale Pits as Templates for Building a Molecular Device.
Small **3**, 818 (2007)

[129] S. A. BURKE, J. M. LEDUE, J. M. TOPPLE, S. FOSTNER, P. GRÜTTER: Relating the Functional Properties of an Organic Semiconductor to Molecular Structure by nc-AFM.
Advanced Materials **21**, 2029 (2009)

[130] O. H. PAKARINEN, J. M. MATIVETSKY, A. GULANS, M. J. PUSKA, A. S. FOSTER, P. GRUTTER: Role of van der Waals forces in the adsorption and diffusion of organic molecules on an insulating surface.
Physical Review B **80**, 085401 (2009)

[131] L. NONY, E. GNECCO, A. BARATOFF, A. ALKAUSKAS, R. BENNEWITZ, O. PFEIFFER, S. MAIER, A. WETZEL, E. MEYER, C. GERBER: Observation of individual mol-

ecules trapped on a nanostructured insulator.
Nano Letters **4**, 2185 (2004)

[132] L. Zimmerli, S. Maier, G. Th, E. Gnecco, O. Pfeiffer, F. Diederich, L. Fendt, E. Meyer: Formation of molecular wires on nanostructured KBr.
Journal of Physics: Conference Series **61**, 1357 (2007)

[133] J. M. Mativetsky, S. A. Burke, S. Fostner, P. Grütter: Templated growth of 3,4,9,10-perylenetetracarboxylic dianhydride molecules on a nanostructured insulator.
Nanotechnology **18**, 105303 (2007)

[134] R. Bennewitz, S. Schär, V. Barwich, O. Pfeiffer, E. Meyer, F. Krok, B. Such, J. Kolodzej, M. Szymonski: Atomic-resolution images of radiation damage in KBr.
Surface Science **474**, L197 (2001)

[135] K. Lämmle, T. Trevethan, A. Schwarz, M. Watkins, A. Shluger, R. Wiesendanger: Unambiguous Determination of the Adsorption Geometry of a Metal-Organic Complex on a Bulk Insulator.
Nano Letters **10**, 2965 (2010)

[136] A. Hinaut, K. Lekhal, G. Aivazian, S. Bataille, A. Gourdon, D. Martrou, S. Gauthier: NC-AFM Study of the Adsorption of Hexamethoxytriphenylene on KBr(001).
Journal of Physical Chemistry C **115**, 13338 (2011)

[137] L. Nony, F. Bocquet, F. Para, F. Chérioux, E. Duverger, F. Palmino, V. Luzet, C. Loppacher: Dipole-driven self-organization of zwitterionic molecules on alkali halide surfaces.
Beilstein Journal of Nanotechnology **3**, 285 (2012)

[138] B. Such, T. Trevethan, T. Glatzel, S. Kawai, L. Zimmerli, E. Meyer, A. L. Shluger, C. H. M. Amijs, P. de Mendoza, A. M. Echavarren: Functionalized

Truxenes: Adsorption and Diffusion of Single Molecules on the KBr(001) Surface.
ACS Nano **4**, 3429 (2010)

[139] M. FENDRICH, T. KUNSTMANN: Organic molecular nanowires: N,N'-dimethylperylene-3,4,9,10-bis(dicarboximide) on KBr(001).
Applied Physics Letters **91**, 023101 (2007)

[140] M. FENDRICH, M. LANGE, C. WEISS, T. KUNSTMANN, R. MOLLER: N,N '-dimethylperylene-3,4,9,10-bis(dicarboximide) on alkali halide (001) surfaces.
Journal of Applied Physics **105**, 094311 (2009)

[141] R. PAWLAK, L. NONY, F. BOCQUET, V. OLSON, M. SASSI, J. M. DEBIERRE, C. LOPPACHER, L. PORTE: Supramolecular Assemblies of 1,4-Benzene Diboronic Acid on KCl(001).
Journal of Physical Chemistry C **114**, 9290 (2010)

[142] T. GLATZEL, L. ZIMMERLI, S. KAWAI, E. MEYER, L.-A. FENDT, F. DIEDERICH: Oriented growth of porphyrin-based molecular wires on ionic crystals analysed by nc-AFM.
Beilstein Journal of Nanotechnology **2**, 34 (2011)

[143] J. V. BARTH: Molecular architectonic on metal surfaces.
Annual review of physical chemistry **58**, 375 (2007)

[144] D. M. DUFFY, J. H. HARDING: Modelling the interfaces between calcite crystals and Langmuir monolayers.
Journal of Materials Chemistry **12**, 3419 (2002)

[145] N. ZHU, T. OSADA, T. KOMEDA: Supramolecular assembly of biphenyl dicarboxylic acid on Au(111).
Surface Science **601**, 1789 (2007)

[146] M. ŚLEDŹ, J. JANCZAK, R. KUBIAK: New crystalline modification of terephthalic acid.
Journal of Molecular Structure **595**, 77 (2001)

[147] A. C. Papageorgiou, S. Fischer, J. Reichert, K. Diller, F. Blobner, F. Klappenberger, F. Allegretti, A. P. Seitsonen, J. V. Barth: Chemical Transformations Drive Complex Self-Assembly of Uracil on Close-Packed Coinage Metal Surfaces.
ACS Nano **6**, 2477 (2012)

[148] L. Kanninen, N. Jokinen, H. Ali-Löytty, P. Jussila, K. Lahtonen, M. Hirsimäki, M. Valden, M. Kuzmin, R. Pärna, E. Nõmmiste: Adsorption structure and bonding of trimesic acid on Cu(100).
Surface Science **605**, 1968 (2011)

[149] P. X. Dai, T. Chen, D. Wang, L. J. Wan: Potential Dependent Adsorption Geometry of 2,5-Dihydroxybenzoic Acid on a Au(111) Surface: An in Situ Electrochemical Scanning Tunneling Microscopy Study.
Journal of Physical Chemistry C **116**, 6208 (2012)

[150] G. Franc, A. Gourdon: Covalent networks through on-surface chemistry in ultra-high vacuum: state-of-the-art and recent developments.
Physical Chemistry Chemical Physics **13**, 14283 (2011)

[151] F. Leydier, C. Chizallet, A. Chaumonnot, M. Digne, E. Soyer, A. A. Quoineaud, D. Costa, P. Raybaud: Brønsted acidity of amorphous silica-alumina: The molecular rules of proton transfer.
Journal of Catalysis **284**, 215 (2011)

[152] M. Haisa, S. Kashino, S. I. Hanada, K. Tanaka, S. Okazaki, M. Shibagaki: The Structures of 2-Hydroxy-5-Methylbenzoic acid and Dimorphs of 2,5-Dihydroxibenzoic acid.
Acta Crystallographica B **38**, 1480 (1982)

[153] M. O. Sinnokrot, E. F. Valeev, C. D. Sherrill: Estimates of the ab initio limit for pi-pi interactions: The benzene dimer.
Journal of the American Chemical Society **124**, 10887 (2002)

[154] S. SADEWASSER, M. C. LUX-STEINER: Correct Height Measurement in Noncontact Atomic Force Microscopy.
Physical Review Letters **91**, 266101 (2003)

[155] L. VITALI, G. LEVITA, R. OHMANN, A. COMISSO, A. DE VITA, K. KERN: Portrait of the potential barrier at metal-organic nanocontacts.
Nature Materials **9**, 320 (2010)

[156] F. HUQ: Molecular modelling analysis of the metabolism of aspirin.
Asian Journal of Chemistry **19**, 102 (2007)

[157] Y. LUO: Comprehensive Handbook of Chemical Bond Energies. CRC Press, 2007

[158] A. G. SLATER, P. H. BETON, N. R. CHAMPNESS: Two-dimensional supramolecular chemistry on surfaces.
Chemical Science **2**, 1440 (2011)

[159] M. D. PRASANNA, T. N. GURU ROW: C - halogen $\cdots \pi$ interactions and their influence on molecular conformation and crystal packing: a database study.
Crystal Engineering **3**, 135 (2000)

Acknowledgements

Zum Schluss möchte ich bei allen Personen ganz herzlich bedanken, die zum Gelingen dieser Arbeit beigetragen haben.

[Personal data removed]

List of Abbreviations

A	oscillation amplitude
AFM	atomic force microscopy
AM	amplitude-modulated
Γ	dissipation
$\Delta\Phi$	difference in work functions
f_0	resonance frequency of freely oscillating cantilever
Δf	frequency shift
$F_{\mathbf{el}}$	electrostatic force
f_{mod}	modulation frequency
FM	frequency modulated
$F_{\mathbf{ts}}$	tip-sample interaction force
k	cantilever spring constant
KPFM	kelvin probe force microscopy
k_{ts}	tip-sample force gradient
NC	non-contact
PLL	phase-locked loop
SPM	scanning probe microscopy
STM	scanning tunneling microscopy
Q	quality factor
U_{cpd}	contact potential difference
U_{dc}	applied DC voltage
U_{mod}	modulation voltage
UHV	ultra-high vacuum

Publications

Publications

This thesis is based on the following publications that I have (co-)authored:

Chap. 5:

Tuning molecular self-assembly on bulk insulator surfaces by anchoring of the organic building blocks
Rahe, P.; Kittelmann, M.; Neff, J.; Nimmrich, M.; Maaß, P.; Kühnle, A.
in preparation

Chap. 6:

Molecular self-assembly on an insulating surface: interplay between substrate templating and intermolecular interactions
Kittelmann, M.; Rahe, P.; Kühnle, A.
Journal of Physics: Condensed Matter **24**, 35, 354007 (2012)

Chap. 7:

Direct Visualization of Molecule Deprotonation on an Insulating Surface
Kittelmann, M.; Rahe, P.; Gourdon, A.; Kühnle, A.
ACS Nano **6**, 8, 7406 (2012)

Chap. 8:

Controlled activation of substrate templating in molecular self-assembly by deprotonation
Kittelmann, M.; Neff, J.; Nimmrich, M.; Rahe, P.; Gourdon, A.; Kühnle, A.
in preparation

Chap. 9:

On-Surface Covalent Linking of Organic Building Blocks on a Bulk Insulator
Kittelmann, M.; Rahe, P.; Nimmrich, M.; Hauke, C.M.; Gourdon, A.; Kühnle, A.
ACS Nano **5**, 11, 8420 (2011)

Chap. 10:

Two-Step On-Surface Polymerization by Selectively Activation on an Insulating Surface
Kittelmann, M.; Nimmrich, M.; Lindner, R.; Gourdon, A.; Kühnle, A.
in preparation

Besides the above mentioned work, I have been involved in the following publications, which are not subject of this thesis:

- **Atomic-resolution imaging of clean and hydrogen-terminated C(100)-(2 × 1) diamond surfaces using noncontact AFM**
  Nimmrich, M.; Kittelmann, M.; Rahe, P.; Mayne, A.J.; Dujardin, G.; von Schmidsfeld, A.; Reichling, M.; Harneit, W.; Kühnle, A.
  Physical Review B **81**, 20, 201403(R) (2010)

- **Molecular Self-Assembly of Enantiopure Heptahelicene-2-Carboxylic Acid on Calcite** $(10\overline{1}4)$
  Hauke, C.M.; Rahe, P.; Nimmrich,M.; Schutte, J.; Kittelmann, M.; Starà, I.G.; Starỳ, I.; Rybàček, J.; Kuhnle, A.
  Journal of Physical Chemistry C **116**, 7, 4637 (2011)

- **From dewetting to wetting molecular layers: C_{60} on $CaCO_3$$(10\overline{1}4)$ as a case study**
  Rahe, P.; Lindner,R.; Kittelmann,M.; Nimmrich, M.; Kühnle, A.
  Physical Chemistry Chemical Physics **14**, 18, 6544 (2012)

- **Influence of charge transfer doping on themorphologies of C_{60} islands on hydrogenated diamond C(100)-(2 × 1)**
  Nimmrich, M.; Kittelmann, M.; Rahe, P.; Harneit, W.; Mayne, A.J.; Dujardin, G.; Kühnle, A.
  Physical Review B **85**, 3, 035420 (2012)

- **Organisch geordnet - Strategien zur Herstellung funktionaler Strukturen organischer Moleküle auf dielektrischen Oberflächen**
  Nimmrich, M.; Rahe, P.; Kittelmann, M.; Kühnle, A.
  Physik Journal **12**, 29 (2012)

- **Influence of Molecule Deprotonation on Molecular Self-Assembly on an Insulating Surface: A Comparison of Ultra-High Vacuum and Liquid Environment**
  Schreiber, M.; Kittelmann, M.; Klassen, S.; Kling, F.; Adam, A.; Eckardt, M.; Greifenstein ,L.; Bechstein, R.; Kühnle, A.
  submitted to Soft Matter

- **Photo-Initiated Covalent Bond Formation on an Insulating Substrate**
  Lindner, R.; Rahe, P.; Kittelmann, M.; Gourdon, A.; Kühnle, A.
  in preparation

Talks

(presenting author underlined)

- **NC-AFM on hydrogenated and on clean diamond(100)**
  Nimmrich, M.; Kittelmann, M.; Rahe, P.; Mayne, A.J.; Dujardin, G.; von Schmidsfeld, A.; Reichling, M.; Harneit, W.; Kühnle, A.
  (NCAFM 2010, Kanazawa, Japan)

- **NC-AFM Aufnahmen von reinem und wasserstoffterminierten Diamant C(100)**
  Kittelmann, M.; Nimmrich, M.; Rahe, P.; Mayne, A.J.; Dujardin, G.; von Schmidsfeld, A.; Reichling, M.; Harneit, W.; Kühnle, A.
  (DPG 2011, Dresden, Germany)

- **On-surface covalent linking on an insulating substrat**
  Kittelmann, M.; Rahe, P.; Nimmrich, M.; Hauke, C.M.; Gourdon, A.; Kühnle, A.
  (ECOSS 28 2011, Wroclaw, Poland)

- **Self-assembly and chiral recognition of heptahelicene acid on an insulating surface**
  Hauke, C.M.; Rahe, P.; Nimmrich, M.; Schütte, J.; Kittelmann, M.; Starà, I.G.; Starỳ, I.; Rybàček, J.; Kühnle, A.
  (ECOSS 28 2011, Wroclaw, Poland)

- **Phase transition of a molecular film and on-surface covalent linking**
  Kittelmann, M.; Rahe, P.; Hauke, C.M.; Nimmrich, M.; Kühnle, A.
  (NCAFM 2011, Lindau, Germany)

- **Adsorption and structure formation of organic molecules on CaCO3**(10$\bar{1}$4) **- Impact for molecular self-assembly on insulating substrates**
  Rahe, P.; Nimmrich, M.; Schütte, J.; Kittelmann, M.; Kühnle, A.
  (NCAFM 2011, Lindau, Germany)

- **Effect of Transfer Doping on the Structure Formation of C_{60} Self-Assembly on Hydrogenated Diamond C(100)-(2 × 1)**
  Nimmrich, M.; Kittelmann, M.; Rahe, P.; Harneit, W.; Mayne, A.J.; Dujardin, G.; Kühnle, A.
  (MRS Fall Meeting 2011, Boston, USA)

- **Lichtinduzierte Knüpfung von kovalenten Bindungen auf Isolatoren**
  Lindner, R.; Kittelmann, M.; Rahe, P.; Hauke, C.M.; Nimmrich, M.; Kühnle, A.
  (DPG 2012, Berlin, Germany)

- **On-surface covalent linking of organic building blocks on a bulk insulator**
  Kittelmann, M.; Rahe, P.; Nimmrich, M.; Lindner, R.; Gourdon, A.; Kühnle, A.
  (DPG 2012, Berlin, Germany)

- **Light-induced formation of covalent bonds on an insulator**
  Lindner, R.; Kittelmann, M.; Rahe, P.; Harneit, W.; Mayne, A.J.; Dujardin, G.; Kühnle, A.
  (ECOSS 29 2012, Edinburgh, United Kingdom)

- **Chiral wetting layers of oligoaramides on an insulating surface**
  Hauke, C.M.; Kittelmann, M.; Rahe, P.; Harneit, W.; Mayne, A.J.; Dujardin, G.; Kühnle, A.
  (ECOSS 29 2012, Edinburgh, United Kingdom)

- **Molecular interplay between substrate templating and intermolecular interactions on an insulating surface**
  Kittelmann, M.; Rahe, P.; Kühnle, A.
  (ECOSS 29 2012, Edinburgh, United Kingdom)

Poster Presentations

(presenting author underlined)

- **High-resolution imaging of bare and hydrogen-saturated diamond C(100) using NC-AFM**
  Nimmrich, M.; Kittelmann, M.; Rahe, P.; Mayne, A.J.; Dujardin, G.; Reichling, M.; Harneit, W.; Kühnle, A.
  (AAFMT 2011, Karlsruhe, Germany)

- **Chiral recognition and homochiral island formation on an insulating substrate**
  Hauke, C.M.; Rahe, P.; Nimmrich, M.; Schütte, J.; Kittelmann, M.; Starà, I.G.; Starỳ, I.; Rybàček, J.; Kühnle, A.
  (AAFMT 2011, Karlsruhe, Germany)

- **Insulating substrates as a surface for chiral recognition and homochiral islands formation**
  Hauke, C.M.; Rahe, P.; Nimmrich, M.; Schütte, J.; Kittelmann, M.; Starà, I.G.; Starỳ, I.; Rybàček, J.; Kühnle, A.
  (ISPM 2011, München, Germany)

- **Adsorption and self-assembly of C_{60} on hydrogenated and pure diamond C(100)**
  Nimmrich, M.; Kittelmann, M.; Rahe, P.; Kühnle, A.
  (ECOSS 28 2011, Wroclaw, Poland)

- **Chiral recognition and homochiral island formation on an insulating substrate**
  Hauke, C.M.; Rahe, P.; Nimmrich, M.; Schütte, J.; Kittelmann, M.; Starà, I.G.; Starỳ, I.; Rybàček, J.; Kühnle, A.
  (NCAFM 2011, Lindau, Germany)

- **3D force maps on $CaCO_3$(10.4) at room temperature**
  Kuhn, S.; Rahe, P.; Masayuki, A.; Yoshiaki, S.; Kittelmann, M.; Kühnle, A.
  (NCAFM 2012, Český Krumlov, Czech Republic)

- **Interplay between substrate templating and intermolecular interactions in molecular self-assembly on an insulating surface**
  Kittelmann, M.; Rahe, P.; Kühnle, A.
  (Symposium: From Reciprocal to Real Space 2012, Berlin, Germany)

- **Atomic Resolution Three Dimensional Force-field Map at Room Temperature on an Insulating Bulk Surface**
  Kuhn, S.; Rahe, P.; Masayuki, A.; Yoshiaki, S.; Kittelmann, M.; Kühnle, A.
  (MRS Fall Meeting 2012, Boston, USA)